STRESS-FUNCTION VARIATIONAL METHOD AND ITS

APPLICATIONS IN THE STRENGTH ANALYSIS OF BONDED

JOINTS AND HARD COATINGS

A Thesis
Submitted to the Graduate Faculty
of the
North Dakota State University
of Agriculture and Applied Science

By

Robert Allen Jenson

In Partial Fulfillment of the Requirements
for the Degree of
MASTER OF SCIENCE

Major Department:
Mechanical Engineering

May 2011

Fargo, North Dakota

North Dakota State University
Graduate School

Title

Stress-Function Variational Method and Its Applications in the Strength

Analysis of Bonded Joints and Hard Coatings

By

Robert Allen Jenson

The Supervisory Committee certifies that this *disquisition* complies with North Dakota State University's regulations and meets the accepted standards for the degree of

MASTER OF SCIENCE

ABSTRACT

Jenson, Robert Allen, M.S., Department of Mechanical Engineering, College of Engineering and Architecture, North Dakota State University, May 2011. Stress-Function Variational Method and Its Applications in the Strength Analysis of Bonded Joints and Hard Coatings. Major Professor: Dr. Xiangfa Wu.

High concentrations of interfacial stress near the adherend ends are primarily responsible for the debonding failure of bonded joints, such as those structured extensively in civil and structural engineering; aeronautical, ground, and marine vehicles; and flexible electronics and microelectronic packaging. Accurate determination of these interfacial stresses is crucial to improved structural design and optimization as well as health monitoring of the structures in which such joints are found. A variety of joint models have been available in the literature for joint strength analysis and structural design. Yet, a few deficiencies still exist in most of these models in accurate prediction of joint stresses, including the violation of the generalized Hooke's law of the adhesive layers and failure to satisfy the physical traction conditions at the free edges of joint adherends.

In this thesis, a generalized stress-function variational method is developed for the determination of the interfacial shear and normal stresses in general bonded bimaterial joints subjected to mechanical and thermomechanical loads. Specifically, three types of joints are considered in this study, including single-sided bonded joints, single-sided strap joints, and single-lap joints. During the formulation, two unknown interfacial stress functions are directly introduced to satisfy the traction boundary conditions of the joints; the *Euler-Bernoulli* elementary beam theory and 2D elasticity are used to determine the stress components of the adherends in terms of the interfacial stress functions. By utilizing

the theorem of minimum complementary strain energy, the governing equations of the bimaterial joint are obtained as a system of two coupled 4th-order ordinary differential equations (ODEs) of the introduced stress functions. These ODEs are formatted into a generalized eigenvalue problem, and are further solved numerically by designing robust and efficient computational codes using MATLAB™. The results of the analysis are validated by comparison with elementary mechanics of materials as well as detailed finite element analysis (FEA) using ANSYS™; the current models can accurately satisfy the shear stress-free boundary conditions at the adherend edges.

In addition, the proposed method is further applied to the analysis of progressive cracking in hard coatings. In this analysis, a cracked hard coating layer bonded onto a substrate is modeled as a single-sided bonded joint, and the expressions of strain energy derived in this study are incorporated into energy-based cracking criteria of the system. Using the above variational method, the critical loads (i.e., applied axial stress, shear force, bending moment, or temperature change) for initial cracking can be determined. Thus, the present method is also capable of modeling progressive cracking in hard coating systems.

ACKNOWLEDGMENTS

DEDICATION

For my family, whose love and encouragement has brought me this far, and my

beautiful wife, without whose support this could not have been accomplished.

TABLE OF CONTENTS

LIST OF TABLES

LIST OF FIGURES

xiii

1. INTRODUCTION

Bonded joints, constructed from two adherends of the same or dissimilar materials fastened by means of bolts, solders, or adhesives, have found broad applications in numerous engineering practices. Bonded joints are used structurally as load transfer elements, surface reinforcing patches, and connectors to link separated parts. Applications of bonded joints can be observed in all manners of vehicle, from ground to marine to aerospace, as well as in mechanical and civil structures. Furthermore, recent developments in the electronics field (e.g. microelectronics packaging, as well as the more-recent advance of flexible electronics) have presented the deposition of stiff silicon structures on compliant substrates—systems easily thought of as small-scale application of bonded joints. Due to the prevalence of bonded joints, it is critical to understand that the integrity and safety of the resulting structures depends greatly on the strength and durability of the joints that comprise them. However, due to dissimilarities in material properties between adherends of the joint (such as a mismatch of Poisson's ratios, Young's moduli, or the thermal expansion coefficients), complicated stress fields arise in the system that include high stress concentrations near the free edges of the adherends under mechanical or thermomechanical loads. These high interfacial stresses are the primary cause of debonding failure commonly observed in engineered joints. Therefore, an accurate stress analysis of bonded joints is required for improved joint design and structural optimization; in addition, improved stress analyses will also advance both health monitoring of structures and our understanding of the failure mechanisms and damage evolution in bonded joints.

1

Stress analysis of bonded joints dates can be tracked to the pioneering works by Volkersen (1938) and Goland and Reissner (1944), with numerous improvements and variations in the decades since then. However, some important notes bear mentioning: most of the existing analytic models found in the literature share a few obvious technical deficiencies in the view of physics. Firstly, many such models failed to satisfy the shear stress-free condition at the free edges of the adherends. That is, at the ends of the overlap region of a bonded joint, where no shear stress should exist, a majority of analytic models available in the literature instead predicts the maximum value of interfacial shear stress. Furthermore, a number of studies of the bonded joint problems treated the adhesive layer using a shear-lag model, which violated the generalized Hooke's law for the adhesive layer; the shear-lag model allows for only shear deformation of the adhesive, which skews the stress-strain relationship detailed by Hooke's law for isotropic, linearly thermoelastic solids.

Therefore, it is the main goal of this thesis work to eliminate these obvious technical deficiencies and provide improved and more physically compatible models for stress analysis of bonded joints. Specifically, a systematic methodology based on the stress-functional variation of complimentary strain energy of bonded joints is formulated for accurate determination of the entire stress field of bonded joints of all kinds of configurations. In the simplest case of bonded joints made of two slender adherends, two interfacial shear and normal stress functions can be directly introduced. Stress equilibrium equations for representative segmental elements of the adherends can then be constructed using these stress functions. Based on classic *Euler-Bernoulli* beam theory and two-dimensional (2D) elasticity, expressions of the planar stress components in the adherends

can be subsequently derived, from which an expression of the complementary strain energy of the joint can be defined. According to the theorem of minimum complementary strain energy, the stationary point of the strain energy corresponds to the state of static equilibrium of the joint. Minimization of the strain energy through variational operations results in a system of two coupled 4th-order ordinary differential equations (ODEs), which can be solved efficiently using eigenfunctions. A compact, efficient, computational package is designed with MATLAB^{TM}. The solution of the joint stress field is determined completely in terms of the joint geometries, material properties, and traction boundary conditions (BCs). Thus, the interfacial stresses in the joint obtained in this study can fully satisfy all the traction BCs properly.

The methods developed in the present work can be effectively applied to a variety of joint configurations subjected to arbitrary combinations of loading. The proposed efficient solution methods are expected to be useful for interfacial damage evaluation of bonded joints, as well as joint design and structural optimization through scaling analysis of joint parameters. The work can also be easily generalized for a number of bonded structures and layered materials—e.g., hard coatings and flexible electronics—where the strength and durability of the system depends highly on interfacial stresses.

2. LITERATURE REVIEW

2.1 Joining Technology and History of Bonded Joints

The history of adhesively bonded joints can be traced back to the mid-Pleistocene era, with the discovery of simple spears constructed from stone flakes bonded to pieces of wood with tar (Mazza et al., 2006). In the past five decades, developments have been made in the application of advanced adhesive joining techniques to aircraft design, where aircraft skins are bonded to support structures, such as stringers and metallic honeycomb assemblies, via adhesives (Higgins, 2000). Furthermore, not only aerospace but also all types of vehicles (e.g. ground and marine transportation, etc.) have evidenced the developments in the application of adhesive joining technology. Besides vehicle design, these adhesive joints have also found use in civil structures and other mechanical systems as well. Some of the reasons for the ever growing use of adhesively bonded joints in engineering applications include the more compact structural design, lower cost in manufacturing, and improved mechanical durability, noise suppression, and weight reduction compared to other types of mechanically bonded constructs (i.e., bolts, rivets, welds, etc.). Adhesively bonded joints normally lead to more efficient load transfer between joined parts and higher durability of the structure (Goncalves et al., 2002; Mortensen and Thomsen, 2002). The adhesive layers in these types of joint can also provide noticeable structural damping, cracking retardant properties, and corrosion resistance (Tsai et al., 1998). Furthermore, adhesive joints are also associated with conservation of materials and weight reduction, which can lower the costs of production relative to other types of mechanical fasteners. It has been reported that 10-15% of the

4

weight of a typical commercial aircraft can be saved by replacing rivets with adhesive bonds (Brockmann et al., 2009). This makes a significant impact on the cost-reduction and energy conservation goals of the industry.

In addition to these applications, the analysis of bonded joints has also become a vital concern with regard to microelectronics packaging and flexible electronics. For microelectronic devices, thermal stresses are the primary cause of debonding failure and functionality defects; more accurate and in-depth analysis of the interfacial thermal stresses in bonded chip components will allow for a better understanding of damage evolution and mechanical failure of these chips and has been the subject of much research in the past three decades (Chen and Nelson, 1979; Ru, 2002; Suhir, 1986, 1989, 1991, 2001; Suhir and Vujosevic, 2010; Suo, 2003; Tsai et al., 2004). Similarly, advances in recent flexible electronics, which involves the deposition of rigid silicon islands on compliant polymeric substrates, rely on a more accurate analysis of the interfacial stresses of the joining components. Such interfacial stresses directly influence the mechanical durability and reliability of such integrated devices (Jiang et al., 2007, 2008; Khang et al., 2006, 2009; Kim and Rogers, 2008; Lu et al., 2007; Song et al., 2008; Sun et al., 2006).

2.2 Types of Bonded Joints

In their simplest form, bonded joints can be defined as two or more adherends of the same or dissimilar materials fastened together by mechanical means (e.g. bolts, rivets, etc.), welds, or adhesives. Due to the widespread use of adhesively bonded joints in a large array of engineering disciplines, it is this particular model that will be studied more extensively in the following work. Typically, adhesively bonded joints come in a variety of

configurations, which are classified primarily according to their geometric arrangements. Figure 2.1 illustrates several of the most commonly used types of bonded joints. To mention a few, the simplest lap joints consist of two or more adherends which overlap each other in the bonding region. In contrast, the strapped joints are similar to a butt joint covered with a reinforcing patch. Also, the simple single-sided bonded joint can be used to represent the microelectronics and flexible electronic devices for analysis.
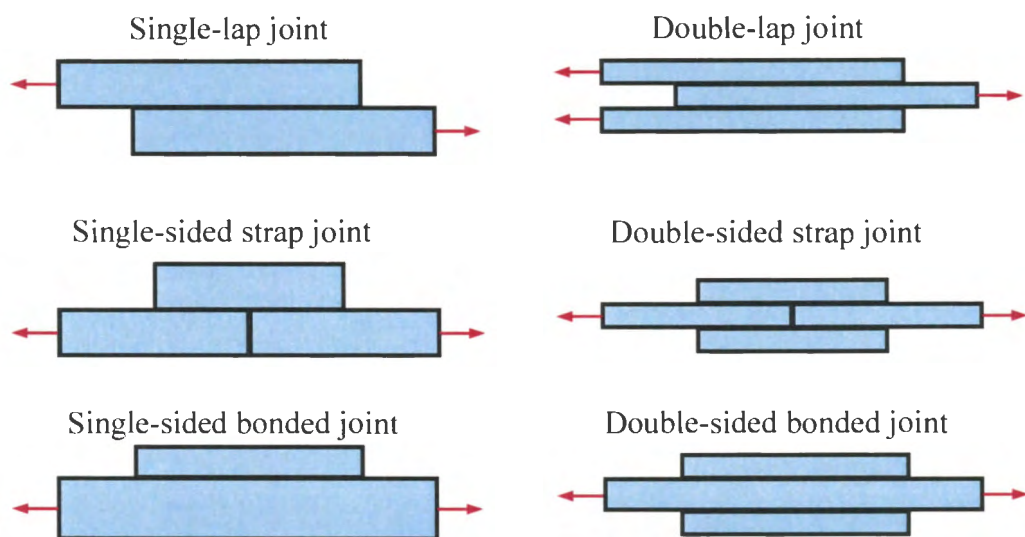
Figure 2.1. Common types of bonded joints.

Due to the existence of multiple interfaces and the mismatch of material properties across the bonding surfaces, complicated stress fields usually occur in bonded joints subjected to external mechanical or thermomechanical loads. These stress fields are characterized by the existence of high stress concentrations near the free edges of the bonded joints, which are responsible for their debonding failure. The failure mode of an adhesively bonded joint depends on the material properties of the adherends, interfacial bonding strength, and loading condition, among others. It can occur in any of several

competing ways; Figure 2.2 shows the typical failure modes of adhesively bonded joints.

These modes can be generally divided into two basic types: failure of the adherend, and

failure of the adhesive layer. While the diagram shows only adhesively bonded single-lap

joints subjected to axial loading, the same failure modes can be also caused by any

combination of axial force, transverse shear force, or bending moments in other types of

joint configuration. Because the high interfacial stresses are directly responsible for the

debonding failure of joints and heavily influence the strength and reliability of the

structures integrated with them, it is essential to joint design, structural optimization and

damage assessment that a more accurate analysis of mechanical and thermal stresses in

bonded joints be completed.
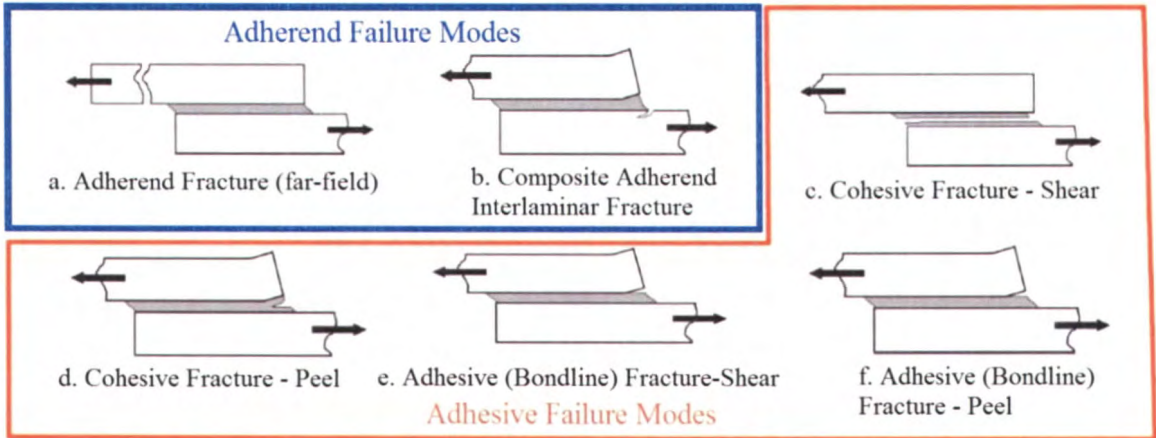
Figure 2.2. Typical failure modes of adhesively bonded joints (Heslehurst and Hart-Smith, 2002).

2.3 Stress Analysis of Bonded Joints: Existing Analytic and Numerical

Methods

Stress analysis of bonded joints can be traced back to Timoshenko's model of a bi-

metal thermostat (Timoshenko, 1925). The analysis, which examined two perfectly bonded

7

dissimilar metal strips subjected to a uniform temperature change, first touched on the concept of free-edge stresses in the joint. Volkersen (1938) and Goland and Reissner (1944) were the first to investigate the stresses in adhesively bonded single-lap joints under mechanical loads. The work performed by Volkersen (1938) introduced the concept of differential shear. In this model, the adhesive layer was only allowed to deform in shear, while the adherends were treated as linearly elastic tension bars. However, this analysis ignored the moment induced by the eccentric load path of the single lap joint. Goland and Reissner (1944) furthered the single lap-joint analysis by considering the joint under the influence of both in-plane tension and bending moment. In order to account for the resulting nonlinearity, two correction factors were introduced for the transverse force and bending moment. Unfortunately, these models violate the shear stress-free conditions by locating the maximum values of interfacial shear stress at the free edges of the adherends.

Further improvements to the bonded joint models continued over decades. Among others, Hart-Smith (1973) developed an elastoplastic joint model that accounted for the large deflection of adhesively bonded joints with the plastic deformation of the adhesive layers, and allowed for individual deformation of the upper and lower adherends. This elastoplastic model also contained the failure criterion of the adhesive layer based on maximum shear strain. The study by Erdogan and Ratwani (1971) utilized classic beam theory and accounted for adherend rotation in order to formulate a set of governing equations to solve for the debonding stresses of several types of joints. However, due to the limitations of classic beam theory, the shear stress-free condition remains broken at the adherend ends, just as it did with many other models reported in the literature. In addition, joint models that consider the adhesive layer as a shear-spring (such as the Volkersen

model, for one) also violate generalized Hooke's law of the adhesive layer. There have been many, varied models available in the literature: Delale, et al. (1981) produced a generalized model considering the adherends as flexural beams; Her (1999) devised a tension-bar model to analyze adhesive lap joints; Lee and Kim (2005) modeled adhesive layers as distributed linearly elastic springs. An exhaustive review of some of the most important analytical models for the stress analysis of bonded joints and relevant comparison in stress analysis has been made recently by da Silva et al. (2009). Furthermore, one improved model of note was developed by Chen and Cheng (1983), which utilized 2D elasticity and the theorem of minimum complementary strain energy to find stresses in the adhesive and substrate layers of an adhesively bonded single-lap joint. Two major assumptions made in the work were firstly that, based on classical beam-plate theory, the longitudinal normal stresses in the adherends vary linearly with respect to the thickness coordinate y. Secondly, it was assumed that the shear stress in the adhesive layer remained constant across the layer thickness, due to it being very thin compared to the adherends. Based on the first assumption, the longitudinal normal stresses in the adherends were defined as linear combinations of arbitrary axial stress functions in the length coordinate x. The moment reduction factor k from the work of Goland and Reissner (1944) was used in the determination of the bending moment and transverse shear force at the free edges of the joint. Minimization of the strain energy of the joint was carried out to determine the governing set of ODEs for the axial stress functions of the joint, which were used to define the remaining stress components according to elasticity. The maximum interfacial stress predicted by Chen and Cheng was found to occur at a distance of approximately 20% the adherend thickness from the free edges; this result is in a close

9

agreement with those based on finite element analyses (FEAs), examples of which can be found in Diaz et al. (2009), Lee & Kim (2005), and Mortensen & Thomsen (2002). By comparison, the current work, detailed in Chapters 3 and 4, makes use of the flexural stress formula for *Euler-Bernoulli* beams to directly write the axial normal stress in terms of two independent unknown interfacial stress functions. In addition, it is not necessary to introduce the artificial Goland and Reissner bending moment factor k in the present formulation and all the stress equilibrium equations are satisfied exactly. The present model can be easily extended for stress and failure analysis of a variety of bonded joints (e.g. adhesively bonded multi-material composite joints) and coating systems.

Parallel to the broad structural applications of bonded joints in engineering, joining technology has also been in use in microelectronics packaging. In particular, with the advent of microelectronics fabrication techniques, thermal stress-induced failure of bonded microelectronic components has gained importance. Better understanding of the failure mechanisms of these microstructures in thermal and electric fields, as well as more accurate prediction of the interfacial thermal stresses will greatly assist in the design and durability analysis of such microelectronic devices. This development has been accompanied by much research (Chen & Nelson, 1979; Ru, 2002; Suhir, 1986, 1989, 1991, 2001; Suhir & Vujosevic, 2010; Suo, 2003; Tsai et al., 2004). Besides, there has been much recent development in the field of flexible electronics consisting of rigid silicon structures deposited on compliant polymeric substrates. The mechanical durability and lifetime of these devices are highly influenced by the interfacial stresses present in the system. Accurate estimation of these stresses is crucial to the commercial development of

flexible electronics (Jiang et al., 2007, 2008; Khang et al., 2006, 2009; Kim & Rogers, 2008; Lu et al., 2007; Song et al., 2008; and Sun et al., 2006).

Obviously, the desired understanding of the interfacial stresses in bonded joints is not just limited to electronics and mechanical engineering. In fact, it has been continuously researched for decades in the vein of structural engineering. The strength and durability of structures utilizing bonded joints on any scale is dependent on the interfacial stresses present in those joints. For instance, Yuan et al. (2004) and Lorenzis and Teng (2007) have performed stress and durability analyses on fiber-reinforced polymer matrix composites (PMCs) and concrete joints. The analysis performed by Yuan et al. (2004) considered a single-lap model of a fiber-reinforced polymer (FRP) sheet adhesively bonded to a concrete prism. A local bond strength parameter and the interfacial fracture energy were used in the derivation of the governing equation of interfacial stresses in the joint, which was solved with the definition of a local slip-bond curve relating the local interfacial shear stress to the local shear slip. Closed-form solutions were found for several loading stages: linear elastic, softening, debonding propagation, and linear unloading. However, the model was predicated on the assumptions that the adherends only deformed in axial tension, and the adhesive layer functions only in shear. Bending effects in the adherends were ignored, and shear stress was assumed constant throughout the adhesive layer. Lorenzis and Teng (2007) reviewed much of the existing work on near-surface mounted FRP reinforcements, and found that further research was needed for better understanding of the debonding failure mechanisms and the interaction between fracture and interfacial bond stress.

Moreover, research has also been performed by Pugno and Surace (2000, 2001), Pugno and Carpinteri (2003), and Carpinteri et al. (2009) on debonding failure of

reinforced concrete and tubular adhesive joints. The analyses of tubular adhesively bonded joints subjected to torsional (Pugno and Surace, 2000, 2001) and axial loadings (Pugno and Carpinteri, 2003) utilized the assumptions that the shear stress in the adhesive layer remained constant, and that only shear stresses in the adhesive and the adherends had an appreciable effect on deformation. The maximum shear stress in the joint was located at the ends of the adhesive layer, with the high stress concentration at the end of the stiffer adherend. A fracture mechanics approach involving the fracture energy and strain energy of the joint has been used to examine the joint failure. Carpinteri et al. (2009) further examined two differing failure criteria for these types of tubular joints: a bond stress-based criterion and an energy method based on fracture mechanics. By assuming a modification of the classical equivalent beam theory involving a shear-lag representation of the adhesive layer, a link was established between the two failure criteria. Discussion of additional models can be found in the above-mentioned review paper dedicated by da Silva et al. (2009). Yet, most of the above models share a common technical deficiency in their assumptions of a shear-lag model for the adhesive layers; this, as already mentioned, violates generalized Hooke's law.

Another area in which the stress analysis of bonded joints is particularly useful is the study of cracking in bonded layers such as failure analysis of composite laminates, surface coatings, microelectronics, etc. In fracture mechanics of layered materials, much work has been done to analyze the cracking behavior in bonded layers subjected to given loads (Suo and Hutchinson, 1990; Hutchinson and Suo, 1992; Li, 2001; Li & Lee, 2009; Sih, 1973; Tada et al., 1973; Yu et al., 2001; Yu & Hutchinson, 2003; Wu & Dzenis, 2002a & 2002b; and Wu et al., 2003a, 2003b, & 2004; etc.). Improved stress analyses of bonded

joints can enhance the accuracy of the effective loads estimated by other classic methods which will be beneficial to better understanding of the failure mechanisms and the fracture analysis of bonded joints.

To date, several improved models for the stress analysis of bonded joints have been developed. For instance, the earlier work by Chang (1990, 1993) was able to arrive at expressions of joint stresses that satisfied all the traction BCs by expressing the interfacial shear and normal stresses as Fourier series and using the minimization of complementary strain energy of the joint to fully determine the coefficients. However, the oversimplified assumption of the adherend deflection leads to interfacial stress predictions of low accuracy at the interface away from the adherend ends when compared to those based on purely numerical methods (e.g. FEA). Furthermore, models developed by Yin (1994a & 1994b) and Wu and Dzenis (2005) directly introduced interfacial stress functions to satisfy all stress equilibrium equations and stress continuity across layer interfaces of laminated composites. In these formulations, deformation compatibility was satisfied in the weak form in the sense of minimization of the complementary strain energy of the laminates, which led to a system of coupled ODEs solved efficiently by using eigenfunctions. These analyses resulted in complete satisfaction of all free-edge traction BCs, as well as a close agreement to results obtained from detailed FEAs at the regions out of a ply-thickness from the free edges.

In this work, a novel bonded joint model is developed for joint stress analysis, in which the joint (either single-sided bonded joint, single-side strap joint, or single-lap joint herein) is considered being made of slender isotropic, linearly thermoelastic adherends. Two unknown interfacial shear and normal (peeling) stress functions are introduced and

13

used in conjunction with the stress equilibrium equations to determine the stress resultants. Stress-equilibrium equations of 2D elasticity and the *Euler-Bernoulli* axial flexural stress formula lead to expressions of all the planar stress components in the joints, which are used to formulate the complementary strain energy of the joint. By invoking the theorem of minimum complementary strain energy, a set of two coupled 4th-order ODEs is derived which can be solved by application of traction BCs (i.e. the equivalent edge forces and moments) to give the interfacial stress distribution in the entire bonded joint.

2.4 Outstanding Problems

Based on the above review, a few outstanding problems remain regarding stress analysis of bonded joints. Firstly, the stress-free BCs at free edges of the bonded joint model must be strictly upheld, and stresses in the adhesive layers of bonded joints need to be properly addressed. Furthermore, a generalized method would be derived which is capable of accurate stress analysis of various joint configurations with arbitrary sets of geometric parameters, material properties, and loading conditions.

The formulation of the bonded joint models in the following work is planned as follows.

Chapter 3 will introduce an analytic model for bonded joints made of a slender substrate reinforced with a cover layer. Two interfacial stress functions are directly introduced, representing the interfacial normal and shear stresses along the bond line of the joint. As the first such approach, to simplify the derivation, an approximate deformation compatibility constraint (i.e. equal curvature of adherends) is enforced to correlate the two stress functions. The entire stress field of the joint is then defined in terms of the unknown

14

interfacial shear stress function. The strain energy of the entire joint is expressed in terms of the interfacial shear stress function, and the theorem of minimum complementary strain energy is invoked. The strain energy of the joint is minimized using the variational operator with respect to the interfacial shear stress function, resulting in the governing 4th-order ODE of constant coefficients.

In Chapter 4, a general stress-function variational method is developed for a single-sided strap joint consisting of two identical slender substrate layers and a slender cover layer. Two interfacial stress functions are directly introduced; however, the approximate deformation compatibility adopted above is eliminated. Due to symmetry of the joint, a reduced half-joint model is analyzed, and the stress components and stress resultants are determined in terms of the two unknown interfacial stress functions. Once again, the strain energy is determined in terms of the unknown interfacial stress functions and minimized according to the theorem of minimum complementary strain energy. In this case, the resulting governing equations consist of a system of two coupled 4th-order ODEs of constant coefficients, which are further converted into a generalized eigenvalue problem and solved numerically by designing a robust, efficient computational package using MATLAB^{TM}. This generalized method is further applied to a single-lap joint model, resulting in a more generalized system of two coupled ODEs to govern the stress field in the joint. In this way, the generality of the stress-function variational method and its potential application in a variety of bonded joint configurations is demonstrated.

In Chapter 5, the general stress-function variational method formulated in Chapter 4 is further employed to study progressive cracking in surface coatings. A cracked stiff, thin coating layer (e.g. ceramic/diamond coating) on a compliant substrate (e.g. steel) is

modeled as a single-sided bonded joint, allowing for accurate determination of the stress field and strain energy stored in the system during cracking. In this way, the important cracking criteria and relevant critical loading parameters are determined, i.e. the critical thermal and/or mechanical load for initial and progressive cracking, as well as crack density for a given set of load parameters.

Chapter 6 summarizes the present research and expects the future work in this field. Further research in this particular area includes stress and failure analysis of generalized multi-layered adhesively bonded joints, as well as adhesively bonded composite joints of generally anisotropic adherends.

3. STRESS ANALYSIS OF SINGLE-SIDED BONDED JOINTS

3.1 Problem Formulation and Solution

3.1.1 Model Formulation

In this chapter, a generalized stress-function variational method is formulated and used to determine the entire stress field of single-sided bonded joints subjected to mechanical and thermomechanical loadings. Based on the assumption of approximately equivalent curvature of the adherends, the stress field can be expressed explicitly and compared with those based on classic beam theory and FEM (i.e. ANSYS^{TM}), respectively.

Consider the model of a single-sided bonded joint consisting of a straight tension bar with a reinforcing patch as shown in Figure 3.1. The reinforcing patch has length L and thickness h_1, while the tension bar has thickness h_2 and length much larger than L; both beams have uniform width b. The coordinate systems are defined such that the x-axis is directed along the axis of the bar from the symmetric mid-plane, while y_1 and y_2 are directed vertically from the centroids of the cross-sections of the reinforcing patch and the tension bar, respectively. Uniform axial tension p_0 is applied to the tension bar far from the reinforcing patch. In addition, the whole joint is also subjected to uniform temperature change ΔT (relative to the temperature of the thermal stress-free state). As already discussed, the mismatch of material properties at the interface leads to high interfacial stresses near the edges of the overlap region of the joint; this also causes the joint ends to be in a complicated three-dimensional stress state. To simplify the subsequent analysis, the joint will be considered in one of two limiting two-dimensional (2D) stress states: either plane-stress, or plane-strain. Both joint components are considered isotropic, linearly

thermoelastic materials. For reference, all following subscripts 1 and 2 refer to the reinforcing patch and straight tension bar, respectively.
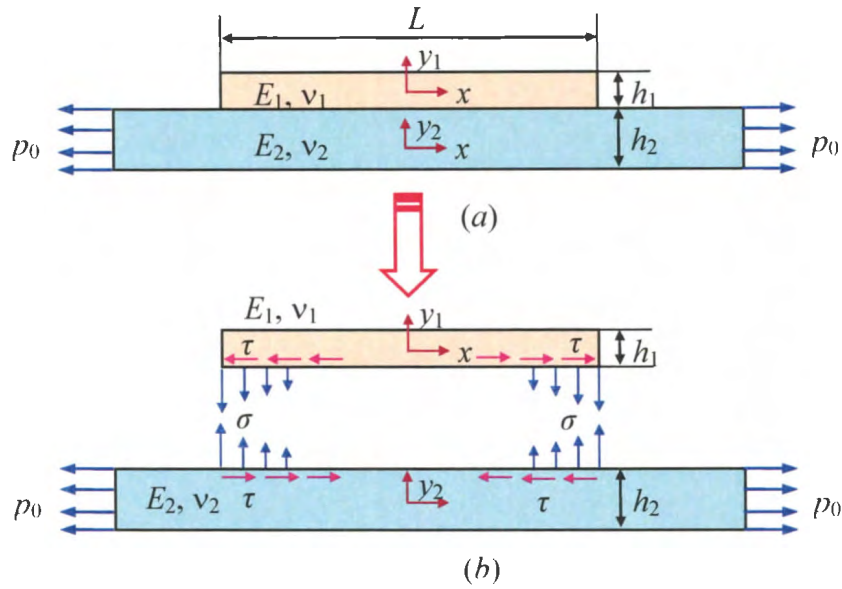
Figure 3.1. Schematic of a bonded joint, consisting of (*a*) a straight tension bar with reinforcing patch and (*b*) illustration of the interfacial stress distribution.

3.1.2 Static Equilibrium Equations and Deformation Compatibility

The loss of lateral symmetry of the joint results in deformation that is a combination of in-plane elongation and lateral deflection. The tension bar and reinforcing patch are considered slender enough to be treated as *Euler-Bernoulli* beams. Stress components and resultants are shown in the free-body diagrams of representative segmental elements of the reinforcing patch and tension bar (Figure 3.2). The equilibrium equations for such an element of the reinforcing patch are given below:

$$\Sigma F_x = 0: \quad \frac{dS_1}{dx} = -b\tau \tag{3.1}$$
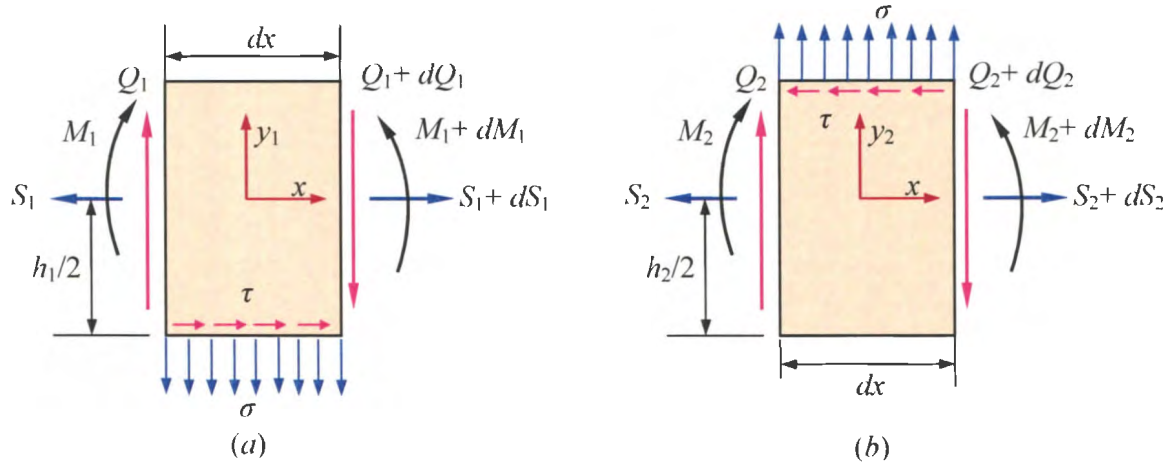
Figure 3.2. Free-body diagrams (FBDs) of representative segmental elements of (a) the reinforcing patch and (b) the tension bar.

$$\Sigma F_x = 0: \quad \frac{dQ_1}{dx} = -b\sigma \tag{3.2}$$

$$\Sigma M = 0: \quad \frac{dM_1}{dx} = Q_1 - \frac{h_1}{2}(b\tau) \tag{3.3}$$

Similarly, the equilibrium equations for the tension bar are:

$$\Sigma F_x = 0: \quad \frac{dS_2}{dx} = b\tau \tag{3.4}$$

$$\Sigma F_y = 0: \quad \frac{dQ_2}{dx} = b\sigma \tag{3.5}$$

$$\Sigma M = 0: \quad \frac{dM_2}{dx} = Q_2 - \frac{h_2}{2}(b\tau) \tag{3.6}$$

To simplify the derivation, we introduce the assumption: an approximate deformation compatibility constraint is imposed in the form of equal radius of curvature between tension bar and reinforcing patch:

$$\frac{M_1}{E_1 I_1} = \frac{M_2}{E_2 I_2} \tag{3.7}$$

19

where

$$I_1 = \frac{1}{12}bh_1^3 \text{ and } I_2 = \frac{1}{12}bh_2^3 \tag{3.8}$$

3.1.3 Stress Resultants

The interfacial shear stress τ and normal stress σ are defined as two unknown functions to be determined:

$$\tau = f(x) \text{ and } \sigma = g(x). \tag{3.9}$$

Due to the symmetry of the joint across the y-axis, $f(x)$ must be an odd function while $g(x)$ must be even:

$$f(-x) = -f(x) \text{ and } g(-x) = g(x). \tag{3.10}$$

At the ends of the overlap region of the joint (free edges of the reinforcing patch) the shear stress-free conditions yields

$$f(-L/2) = f(L/2) = 0 \tag{3.11}$$

Stress resultants of the adherends can be expressed in terms of the unknown functions f and g by the following procedure. Integration of (3.1) with respect to x from $x = -L/2$ yields

$$\int_{-L/2}^{x} dS_1 = -\int_{-L/2}^{x} bf(\xi)\, d\xi \tag{3.12}$$

By utilizing the traction-free boundary condition at $x = -L/2$ (that is, $S_1(-L/2) = 0$) the normal stress resultant can be expressed as

$$S_1(x) = -b\int_{-L/2}^{x} f(\xi)\, d\xi \tag{3.13}$$

Integrating (3.2) with respect to x from $x = -L/2$ yields

$$\int_{-L/2}^{x} dQ_1 = -\int_{-L/2}^{x} bg(\xi)\, d\xi \qquad (3.14)$$

The shear stress-free boundary condition at $x = -L/2$ (such that $Q_1(-L/2) = 0$) similarly leads to the shear stress resultant being written as

$$Q_1(x) = -b\int_{-L/2}^{x} g(\xi)\, d\xi \qquad (3.15)$$

Similarly for the moment, integration of (3.3) gives

$$\int_{-L/2}^{x} dM_1 = \int_{-L/2}^{x} \left[Q_1(\xi) - \frac{h_1}{2}(b\tau) \right] d\xi \qquad (3.16)$$

This, by applying the moment-free condition at $x=-L/2$ reduces to the expression for the bending moment:

$$M_1(x) = -b\int_{-L/2}^{x}\int_{-L/2}^{\xi} g(\varsigma)\, d\varsigma\, d\xi - \frac{bh_1}{2}\int_{-L/2}^{x} f(\xi)\, d\xi \qquad (3.17)$$

This same procedure can be used on the tension bar: integrate Eqs. (3.4) through (3.6), apply the proper boundary conditions, and arrive at the following stress resultants:

$$S_2(x) = p_0(bh_2) + b\int_{-L/2}^{x} f(\xi)\, d\xi \qquad (3.18)$$

$$Q_2(x) = b\int_{-L/2}^{x} g(\xi)\, d\xi \qquad (3.19)$$

$$M_2(x) = b\int_{-L/2}^{x}\int_{-L/2}^{\xi} g(\varsigma)\, d\varsigma\, d\xi - \frac{bh_2}{2}\int_{-L/2}^{x} f(\xi)\, d\xi \qquad (3.20)$$

Furthermore, the stress functions f and g can be correlated through the deformation compatibility constraint of equal curvature (3.7):

$$\frac{E_2 I_2}{E_1 I_1}\left[-\int_{-L/2}^{x}\int_{-L/2}^{\xi} g(\varsigma)\, d\varsigma\, d\xi - \frac{h_1}{2}\int_{-L/2}^{x} f(\xi)\, d\xi \right] = \int_{-L/2}^{x}\int_{-L/2}^{\xi} g(\varsigma)\, d\varsigma\, d\xi - \frac{h_2}{2}\int_{-L/2}^{x} f(\xi)\, d\xi$$

$$(3.21)$$

The expression in (3.21) can be reduced by differentiating both sides of the equation and simplified to get

$$f(x) = -2\frac{\eta_0}{h_2} \int_{-L/2}^{x} g(\xi)\, d\xi \tag{3.22}$$

where $\eta_0 = (e_{21}h_{21}^3 + 1)/(e_{21}h_{21}^2 - 1)$, $e_{21} = E_2/E_1$, and $h_{21} = h_2/h_1$. This allows the bending moments to be rewritten as

$$M_1(x) = -\frac{bh_1}{2}(1 - \eta_0^{-1}h_{21})\int_{-L/2}^{x} f(\xi)\, d\xi \tag{3.23}$$

$$M_2(x) = -\frac{bh_2}{2}(1 + \eta_0^{-1})\int_{-L/2}^{x} f(\xi)\, d\xi \tag{3.24}$$

3.1.4 Stress Components

The components of the joint are considered slender enough to be modeled according to *Euler-Bernoulli* beam theory; therefore the axial normal stress in the reinforcing patch can be found using the *Euler-Bernoulli* flexural stress formula:

$$\sigma_{xx}^{(1)} = \frac{S_1}{bh_1} - \frac{M_1 y_1}{I_1} = -\left[\frac{1}{h_1} - \frac{6y_1}{h_1^2}\left(1 - \frac{4}{3}\eta_0^{-1}h_{21}\right)\right]\int_{-L/2}^{x} f(\xi)d\xi \tag{3.25}$$

The shear stress in the reinforcing patch is found via integration of the elasticity equilibrium equation

$$\frac{\partial\sigma_{xx}^{(1)}}{\partial x} + \frac{\partial\tau_{y_1x}^{(1)}}{\partial y_1} = 0 \tag{3.26}$$

with respect to y_1 from an arbitrary choice of y to $y_1 = h_1/2$

$$\int_{-y_1}^{h_1/2}\frac{\partial\sigma_{xx}^{(1)}}{\partial x}dy_1 + \int_{y_1}^{h_1/2}\frac{\partial\tau_{y_1x}^{(1)}}{\partial y_1}dy_1 = 0 \tag{3.27}$$

22

Solving this equation for $\tau_{y_1 x}^{(1)}$ and utilizing the traction-free condition at the top surface,

$\tau_{y_1 x}^{(1)}(h_1/2) = 0$, gives the shear stress in the reinforcing patch:

$$\tau_{y_1 x}^{(1)} = -\left[\frac{1}{h_1}\left(\frac{h_1}{2} - y_1\right) - \frac{3}{h_1^2}\left(\frac{h_1^2}{4} - y_1^2\right)\left(1 - \frac{4}{3}\eta_0^{-1}h_{21}\right)\right] f(x) \tag{3.28}$$

Again, integration of the equilibrium equation (2D elasticity)

$$\frac{\partial \sigma_{y_1 y_1}^{(1)}}{\partial y_1} + \frac{\partial \tau_{xy_1}^{(1)}}{\partial x} = 0 \tag{3.29}$$

with respect to y_1 from y to $y_1 = h_1/2$ gives

$$\int_{y_1}^{h_1/2} \frac{\partial \sigma_{y_1 y_1}^{(1)}}{\partial y_1} dy_1 + \int_{y_1}^{h_1/2} \frac{\partial \tau_{xy_1}^{(1)}}{\partial x} dy_1 = 0 \tag{3.30}$$

Solving for the normal stress and applying the traction-free condition at the top surface of the reinforcing patch gives the result:

$$\sigma_{y_1 y_1}^{(1)} = -\left\{\frac{1}{h_1}\left[\frac{h_1}{2}\left(\frac{h_1}{2} - y_1\right) - \frac{1}{2}\left(\frac{h_1^2}{4} - y_1^2\right)\right]\right.$$
$$\left. - \frac{3}{h_1^2}\left[\frac{h_1^2}{4}\left(\frac{h_1}{2} - y_1\right) - \frac{1}{3}\left(\frac{h_1^3}{8} - y_1^3\right)\right]\left(1 - \frac{4}{3}\eta_0^{-1}h_{21}\right)\right\} f'(x) \tag{3.31}$$

The same approach can be applied to find the stresses in the tension bar. The flexural stress formula for the tension bar gives

$$\sigma_{xx}^{(2)} = \frac{S_2}{bh_2} - \frac{M_2 y_2}{I_2} = p_0 + \left[\frac{1}{h_2} + \frac{6y_2}{h_2^2}\left(1 + \frac{4}{3}\eta_0^{-1}\right)\right]\int_{-L/2}^{x} f(\xi)\, d\xi \tag{3.32}$$

Next, the equilibrium equation

$$\frac{\partial \sigma_{xx}^{(2)}}{\partial x} + \frac{\partial \tau_{y_2 x}^{(2)}}{\partial y_2} = 0 \tag{3.33}$$

can be integrated from the bottom (free) surface at $y_2 = h_2/2$ to an arbitrary point y_2:

23

$$\int_{-h_2/2}^{y_2} \frac{\partial \sigma_{xx}^{(2)}}{\partial x} dy_2 + \int_{-h_2/2}^{y_2} \frac{\partial \tau_{y_2 x}^{(2)}}{\partial y_2} dy_2 = 0 \tag{3.34}$$

Using the traction-free condition $\tau_{y_2 x}^{(2)}(-h_2/2) = 0$ on the bottom surface, this equation can be solved to give the shear stress in the tension bar:

$$\tau_{y_2 x}^{(2)} = -\left[\frac{1}{h_2}\left(y_2 + \frac{h_2}{2} \right) + \frac{3}{h_2^2}\left(y_2^2 - \frac{h_2^2}{4} \right)\left(1 + \frac{4}{3}\eta_0^{-1} \right) \right] f(x) \tag{3.35}$$

To determine the normal stress, the equilibrium equation

$$\frac{\partial \sigma_{y_2 y_2}^{(2)}}{\partial y_2} + \frac{\partial \tau_{xy_2}^{(2)}}{\partial x} = 0 \tag{3.36}$$

is integrated with respect to y_2 from the bottom surface:

$$\int_{-h_2/2}^{y_2} \frac{\partial \sigma_{y_2 y_2}^{(2)}}{\partial y_2} dy_2 + \int_{-h_2/2}^{y_2} \frac{\partial \tau_{xy_2}^{(2)}}{\partial x} dy_2 = 0 \tag{3.37}$$

Applying the stress-free condition at $y_2 = -h_2/2$ yields the normal stress in the tension bar:

$$\sigma_{y_2 y_2}^{(2)} = \left\{ \frac{1}{h_2}\left[\frac{1}{2}\left(y_2^2 - \frac{h_2^2}{4} \right) + \frac{h_2}{2}\left(y_2 + \frac{h_2}{2} \right) \right] \right.$$
$$\left. + \frac{3}{h_2^2}\left[\frac{1}{3}\left(y_2^3 + \frac{h_2^3}{8} \right) - \frac{h_2^2}{4}\left(y_2 + \frac{h_2}{2} \right) \right]\left(1 + \frac{4}{3}\eta_0^{-1} \right) \right\} f'(x) \tag{3.38}$$

3.1.5 Governing Equation of Interfacial Stresses

The theorem of minimum complementary strain energy is used to determine the stress distribution of the bonded joint problem. For the case of linearly thermoelastic materials considered here, the strain energy of the entire joint can be expressed as

$$U = b \int_{-L/2}^{L/2} \int_{-h_1/2}^{h_1/2} \left\{ \frac{1}{2} \left[\sigma_{xx}^{(1)} \varepsilon_{xx}^{(1)} + \sigma_{yy}^{(1)} \varepsilon_{yy}^{(1)} \right] + \frac{1+\nu_1}{E_1} \left(\tau_{xy_1}^{(1)} \right)^2 \right\} dx \, dy_1$$

$$+ b \int_{-L/2}^{L/2} \int_{-h_2/2}^{h_2/2} \left\{ \frac{1}{2} \left[\sigma_{xx}^{(1)} \varepsilon_{xx}^{(1)} + \sigma_{yy}^{(1)} \varepsilon_{yy}^{(1)} \right] + \frac{1+\nu_1}{E_1} \left(\tau_{xy_2}^{(2)} \right)^2 \right\} dx \, dy_2$$

(3.39)

where the normal strains

$$\varepsilon_{xx}^{(i)} = \frac{\sigma_{xx}^{(i)}}{E_i} - \nu_i \frac{\sigma_{yy}^{(i)}}{E_i} + \alpha_i \Delta T$$

$$\varepsilon_{yy}^{(i)} = \frac{\sigma_{yy}^{(i)}}{E_i} - \nu_i \frac{\sigma_{xx}^{(i)}}{E_i} + \alpha_i \Delta T$$

(3.40)

are defined according to generalized Hooke's law for isotropic, linearly thermoelastic solids in plane-stress, α_i, $(i = 1,2)$ are the coefficients of thermal expansion, and ΔT is the uniform temperature change from a thermal stress-free state. The above expressions can be conveniently converted to the corresponding plane-strain case by replacing Young's moduli E_i by $E_i / (1 - \nu_i^2)$, Poisson's ratios ν_i by $\nu_i / (1 - \nu_i)$, and thermal expansion coefficients α_i by $(1 + \nu_i)\alpha_i$. The theorem of minimum complementary strain energy states that the strain energy of the joint reaches a stationary point at the state of static equilibrium. The above strain energy expression is a functional with respect to the unknown stress function f, so the application of this theorem yields the requirement

$$\delta U = 0$$

(3.41)

where δ is the variational operator with respect to f. This leads to

$$b \int_{-L/2}^{L/2} \int_{-h_1/2}^{h_1/2} \left\{ \frac{1}{E_1} \left[\sigma_{xx}^{(1)} \delta\varepsilon_{xx}^{(1)} + \delta\sigma_{xx}^{(1)} \varepsilon_{xx}^{(1)} + \sigma_{y_1y_1}^{(1)} \delta\varepsilon_{y_1y_1}^{(1)} + \delta\sigma_{y_1y_1}^{(1)} \varepsilon_{y_1y_1}^{(1)} \right] + \frac{2(1+\nu_1)}{E_1} \tau_{xy_1}^{(1)} \delta\tau_{xy_1}^{(1)} \right\} dxdy_1$$

$$+ b \int_{-L/2}^{L/2} \int_{-h_2/2}^{h_2/2} \left\{ \frac{1}{E_2} \left[\sigma_{xx}^{(2)} \delta\varepsilon_{xx}^{(2)} + \delta\sigma_{xx}^{(2)} \varepsilon_{xx}^{(2)} + \sigma_{y_2y_2}^{(2)} \delta\varepsilon_{y_2y_2}^{(2)} + \delta\sigma_{y_2y_2}^{(2)} \varepsilon_{y_2y_2}^{(2)} \right] + \frac{2(1+\nu_2)}{E_2} \tau_{xy_2}^{(2)} \delta\tau_{xy_2}^{(2)} \right\} dxdy_2 = 0$$

(3.42)

The stress components from (3.25), (3.28), (3.31), (3.32), (3.35), and (3.38) can be substituted into (3.42) and the variational operations is performed on the strain energy expression. After simplification, the interfacial shear stress function f satisfies a 4th-order ODE of constant coefficients, given for the plane-strain case as

$$F^{(IV)}(\xi) - 2pF''(\xi) + q^2 F(\xi) + \left[-e_{21}^{-1} + \frac{1}{2}(\alpha_1 - \alpha_2)\Delta T E_1 / p_0 \right] / A_{11} = 0 \qquad (3.43)$$

where

$$F(\xi) = F(x / h_1) = -\left(\frac{1}{p_0 h_1} \right) \int_{-L/2}^{x} f(x) \, dx \qquad (3.44)$$

$$p = -A_{12} / (2A_{11}) \qquad (3.45)$$

$$q = \sqrt{A_{22} / A_{11}} \qquad (3.46)$$

$$A_{11} = \left(\frac{1}{20} - \frac{2}{15}\beta_1 + \frac{13}{140}\beta_1^2 \right) + e_{21}^{-1} h_{21}^3 \left(\frac{1}{20} - \frac{2}{15}\beta_2 + \frac{13}{140}\beta_2^2 \right) \qquad (3.47)$$

$$A_{12} = \left(-\frac{2}{3} + \beta_1 - \frac{3}{5}\beta_1^2 - \nu_1 + \beta_1\nu_1 \right) + e_{21}^{-1} h_{21} \left(-\frac{2}{3} + \beta_2 - \frac{3}{5}\beta_2^2 - \nu_2 + \beta_2\nu_2 \right) \qquad (3.48)$$

$$A_{22} = \left(1 + 3\beta_1^2 \right) + e_{21}^{-1} h_{21}^{-1} \left(1 + 3\beta_2^2 \right) \qquad (3.49)$$

$$\beta_1 = 1 - \eta_0^{-1} h_{21} \qquad (3.50)$$

$$\beta_2 = 1 + \eta_0^{-1} \qquad (3.51)$$

Because the stress function $f(x)$ is required to be an odd function (due to symmetry across the y-axis), $F(\xi)$ must be an even function. In general, there are two meaningful solution cases for the above ODE: the case that $q > p$, and $p > q$.

In the case of $q > p$, the solution (3.44) has the form

$$F(\xi) = C_1 \cosh(\beta\xi)\cos(\gamma\xi) + C_2 \sinh(\beta\xi)\sin(\gamma\xi)$$
$$+ \left[e_{21}^{-1} - \frac{1}{2}(\alpha_1 - \alpha_2)\Delta TE_1 / p_0 \right] / \left(q^2 A_{11} \right) \tag{3.52}$$

where $\beta = \sqrt{(p+q)/2}$, $\gamma = \sqrt{(q-p)/2}$, and C_1 and C_2 are unknown constants. From

(3.52), the interfacial shear stress function can be defined by

$$f(x) = p_0 h_1 \frac{dF(\xi)}{dx}$$
$$= p_0 \left[(C_1\beta + C_2\gamma)\sinh(\beta x / h_1)\cos(\gamma / h_1) \right. \tag{3.53}$$
$$\left. + (-C_1\gamma + C_2\beta)\cosh(\beta x / h_1)\sin(\gamma x / h_1) \right]$$

A relationship between the constants C_1 and C_2 can be established by applying the shear

stress-free condition at $x = \pm L / 2$:

$$\kappa = \frac{C_1}{C_2} = \frac{\gamma\sinh[\beta L/(2h_1)]\cos[\gamma L/(2h_1)] + \beta\cosh[\beta L/(2h_1)]\sin[\gamma L/(2h_1)]}{\gamma\cosh[\beta L/(2h_1)]\sin[\gamma L/(2h_1)] - \beta\sinh[\beta L/(2h_1)]\cos[\gamma L/(2h_1)]} \tag{3.54}$$

Substituting (3.54) into (3.53) and (3.52) and rearranging gives

$$f(x) = C_2 p_0 \left[(\kappa\beta + \gamma)\sinh(\beta x / h_1)\cos(\gamma x / h_1) + (-\kappa\gamma + \beta)\cosh(\beta x / h_1)\sin(\gamma x / h_1) \right] \tag{3.55}$$

and

$$F(x) = C_2 \left[\kappa\cosh(\beta x / h_1)\cos(\gamma x / h_1) + \sinh(\beta x / h_1)\sin(\gamma x / h_1) \right]$$
$$+ \left[e_{21}^{-1} - \frac{1}{2}(\alpha_1 - \alpha_2)\Delta TE_1 / p_0 \right] / (q^2 A_{11}) \tag{3.56}$$

By applying the axial traction-free and moment-free conditions at $x = \pm L / 2$, the constant

C_2 can be determined:

$$C_2 = \frac{\left[-e_{21}^{-1} + \frac{1}{2}(\alpha_1 - \alpha_2)\Delta TE_1 / p_0 \right] / (q^2 A_{11})}{\kappa\cosh[\beta L/(2h_1)]\cos[\gamma L/(2h_1)] + \sinh[\beta L/(2h_1)]\sin[\gamma L/(2h_1)]} \tag{3.57}$$

Alternatively, in the case of $p > q$, the solution takes the form

27

$$F(\xi) = C_1 \cosh(\beta\xi) + C_2 \cosh(\gamma\xi) + \left[e_{21}^{-1} - \frac{1}{2}(\alpha_1 - \alpha_2)\Delta T E_1 / p_0 \right] / (q^2 A_{11}) \tag{3.58}$$

where $\beta = \sqrt{p + \sqrt{p^2 - q^2}}$, $\gamma = \sqrt{p - \sqrt{p^2 - q^2}}$, and C_1 and C_2 are two unknown coefficients to be determined. Now the expression of f becomes

$$f(x) = p_0 h_1 \frac{dF}{dx} = p_0 \left[C_1 \beta \sinh(\beta x / h_1) + C_2 \gamma \sinh(\gamma x / h_1) \right] \tag{3.59}$$

where the ratio of the unknown constants has again been determined by applying the shear-free condition at the adherend ends:

$$\kappa = \frac{C_1}{C_2} = -\frac{\gamma \sinh[\gamma L / (2h_1)]}{\beta \sinh[\beta L / (2h_1)]} \tag{3.60}$$

and the traction- and moment-free conditions yield the constant C_2:

$$C_2 = \frac{\left[-e_{21}^{-1} + \frac{1}{2}(\alpha_1 - \alpha_2)\Delta T E_1 / p_0 \right] / (q^2 A_{11})}{\kappa \cosh[\beta L / (2h_1)] + \cosh[\gamma L / (2h_1)]} \tag{3.61}$$

For both of the cases above, the interfacial normal stress function g is found according to (3.22) as

$$g(x) = \frac{h_2}{2\eta_0} f'(x) \tag{3.62}$$

3.2 Results and Discussion

3.2.1 Comparison with Elementary Beam Theory

Now that the interfacial shear and normal stresses of the bonded joint have been explicitly determined by (3.55), (3.59), and (3.62), these solutions can be validated by several means. First, consider the shear force transferred by the interface of the left half of

the reinforcing patch. According to static equilibrium and Eq. (3.13), this force should

equal the axial force of the reinforcing patch at the mid-span of the adherend:

$$S_{10} = b \int_{-l/2}^{0} f(x)\,dx \tag{3.63}$$

Furthermore, this axial force at the mid-span should be approximately equal to that

predicted by the *transformed section technique* of composite beams (Beer et al., 2009)

from elementary mechanics of materials. Consider the half-joint shown in Figure 3.3, and
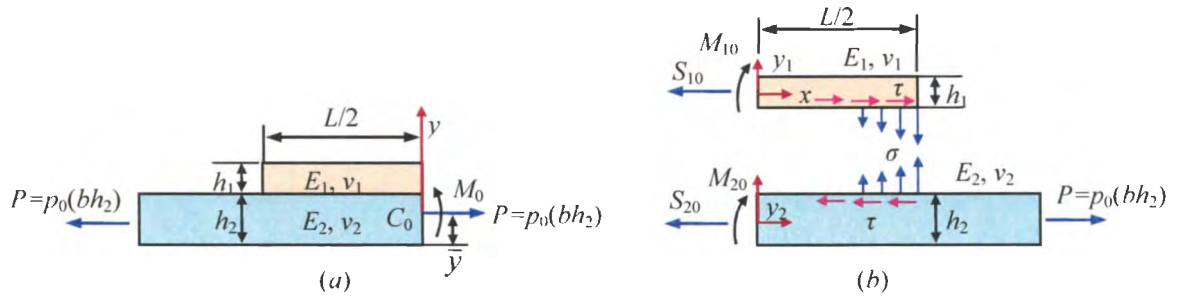
Figure 3.3. FBDs of the half-joints for determination of stress resultants at mid-span for (*a*) the centroid of the whole cross-section and (*b*) the individual adherends.

let the reinforcing patch be the reference material. Then the location of the centroid of the

joint C_0 is given by

$$\bar{y} = \frac{h_1(h_1/2 + h_2) + e_{21}h_2^2/2}{h_1 + e_{21}h_2} \tag{3.64}$$

The effective area moment of inertia of the transformed cross-section is calculated as

$$I_{effective} = \frac{bh_1^3}{12} + bh_1(h_1/2 + h_2 - \bar{y})^2 + \frac{e_{21}bh_2^3}{12} + e_{21}bh_2(h_2/2 - \bar{y})^2 \tag{3.65}$$

and the effective bending moment at C_0 is

$$M_0 = p_0(bh_2)(\bar{y} - h_2/2) \tag{3.66}$$

Therefore the flexural stress in the reinforcing patch can be described by

$$\sigma_{xx}^{(1)} = \frac{p_0 h_2}{h_1 + e_{21} h_2} - \frac{M_0 y}{I_{effective}} \qquad (3.67)$$

Substituting (3.64), (3.65), and (3.66) into (3.67) and integrating with respect to y over the thickness of the cover layer yields the effective axial force

$$S_{10}' = b \int_{A_1} \sigma_{xx}^{(1)} \, dy = \frac{p_0 h_1 h_2}{h_1 + e_{21} h_2} - \frac{M_0}{I_{effective}} \int_{h_2 - \bar{y}}^{h_1 + h_2 - \bar{y}} y \, dy$$

$$= p_0 h_2 \left[\frac{h_1}{h_1 + e_{21} h_2} - \frac{h_2 (\bar{y} - h_2 / 2)(2h_1 + h_2 - 2\bar{y})}{2 I_{effective}} \right] \qquad (3.68)$$

To compare the results from the present model to those predicted by (3.68), consider a bonded joint consisting of an aluminum tension bar (E_2 = 70 GPa, v_2 = 0.34) with a steel reinforcing patch (E_1 = 200 GPa, v_1 = 0.29). The geometric parameters of the joint are h_1/h_2 = 1/4 and L/h_2 = 20. Substituting these variables into the present formulation yields the following parameters:

$$
\begin{aligned}
p &= 0.430357 & \beta &= 0.865787 \\
q &= 1.06882 & \gamma &= 0.565005 \\
& & \kappa &= -2.47821
\end{aligned}
\qquad (3.69)
$$

Now (3.53) and (3.62) can be expressed as

$$f(x) = -7.24913 \times 10^{-16} p_0 \left[2.26599 \cosh(0.865787x) \sin(0.565005x) \right.$$
$$\left. -1.58059 \sinh(0.865787x) \cos(0.565005x) \right] \qquad (3.70)$$

$$g(x) = -7.12512 \times 10^{-17} p_0 \left[-0.0881639 \cosh(0.865787) \cos(0.565005x) \right.$$
$$\left. + 2.85491 \sinh(0.865787x) \sin(0.565005x) \right] \qquad (3.71)$$

Substituting (3.70) into (3.63) gives the shear force transferred by the reinforcing patch as

$$S_{10} = 0.580789(p_0 h_1) \qquad (3.72)$$

The corresponding calculation of force by the *transformed section technique* (3.68) gives the axial force at the reinforcing patch mid-span as

$$S_{10}' = 0.580789(p_0 h_1)$$ (3.73)

These results show the axial tensile force at the mid-span of a long ($L/h_2 = 20$) reinforcing patch obtained by the present method are accurate, despite being far removed from classic beam theory.

The effect of length ratio on the transferred axial force is examined in Table 1, which shows the relative deviation of axial force at the mid-span for varying length ratios. The same joint parameters (Young's moduli, Poisson's ratios, thickness ratio) used above were substituted into (3.55), (3.59), and (3.63) with varying length ratios to compare with (3.68). Table 3.1 shows a clear dependence on the length ratio for the deviation between the two models: the present method covers the classic beam theory predictions well for a longer reinforcing patch, while the deviation grows for shorter lengths. This can be attributed to the tendency of classic beam theory to break down for shorter and thicker beams.

Table 3.1. Comparison of the relative deviation between the axial forces at the mid-span of the reinforcing patch determined via the present method vs. the *transformed section technique*.

Length ratio (L/h_2)	2	3	4	5	10
Relative deviation (%)	3.57	1.47	0.332	3.49×10^{-3}	7.02×10^{-6}

3.2.2 Comparison with FEM

To further validate the results, comparison is made with those obtained by commercial FEA package, ANSYS™. The joint is constructed of an aluminum substrate with a steel reinforcing patch, with the same Young's moduli and Poisson's ratios as detailed above. The thickness of the reinforcing patch is $h_1 = 2$ mm, and the aluminum

31

substrate has thickness h_2 = 4 mm; the length of the patch is L = 40 mm (see Figure 3.1) and the width of the adherends is taken as unity. The joint is considered in a *plane-stress* state and subjected to uniform axial tensile stress p_0 = 1 MPa. The model was constructed in ANSYS™ using four-node elements (PLANE182) with a mapped uniform quadrilateral mesh. In order to address the stress singularity near the free edges of the joint, several different mesh configurations were utilized. The uniform mapped quadrilateral mesh was employed at four different sizes (0.4×0.4 mm, 0.2×0.2 mm, 0.1×0.1 mm, and 0.05×0.05 mm), so that the sensitivity of the free-edge stress to mesh size could be captured. An element plot showing the meshing at 0.2×0.2 mm for the ANSYS model is shown Figure 3.4. Note that a symmetry BC has been applied along the left edge representing the vertical axis of symmetry for the bonded joint, and a uniform pressure of 1 MPa has been applied as the axial load; a single corner node has been constrained to prevent deflection in the vertical direction near the applied load so as to mimic the realistic loading conditions of the joint subjected to tensile strength testing.

The results of the analysis are found in Figures 3.5 through 3.7, which show the interfacial shear stress (Figures 3.5 a, 3.6 a and 3.7 a) and interfacial normal stress (Figures 3.5 b, 3.6 b and 3.7 b) near the right free edge of the joint. The stress singularity near the free edge of the joint is evidenced in the FEM analysis by the rapidly increasing peak interfacial stress with decreasing mesh size. Like other analytic models available in the literature, the present semi-analytic model is unable to predict the stress singularity near the free edge, while it does fit the growth tendency of interfacial stresses predicted by FEM reasonably well. This result verifies that the current method is accurate enough to be used for simple scaling analysis and general optimization of joint design.
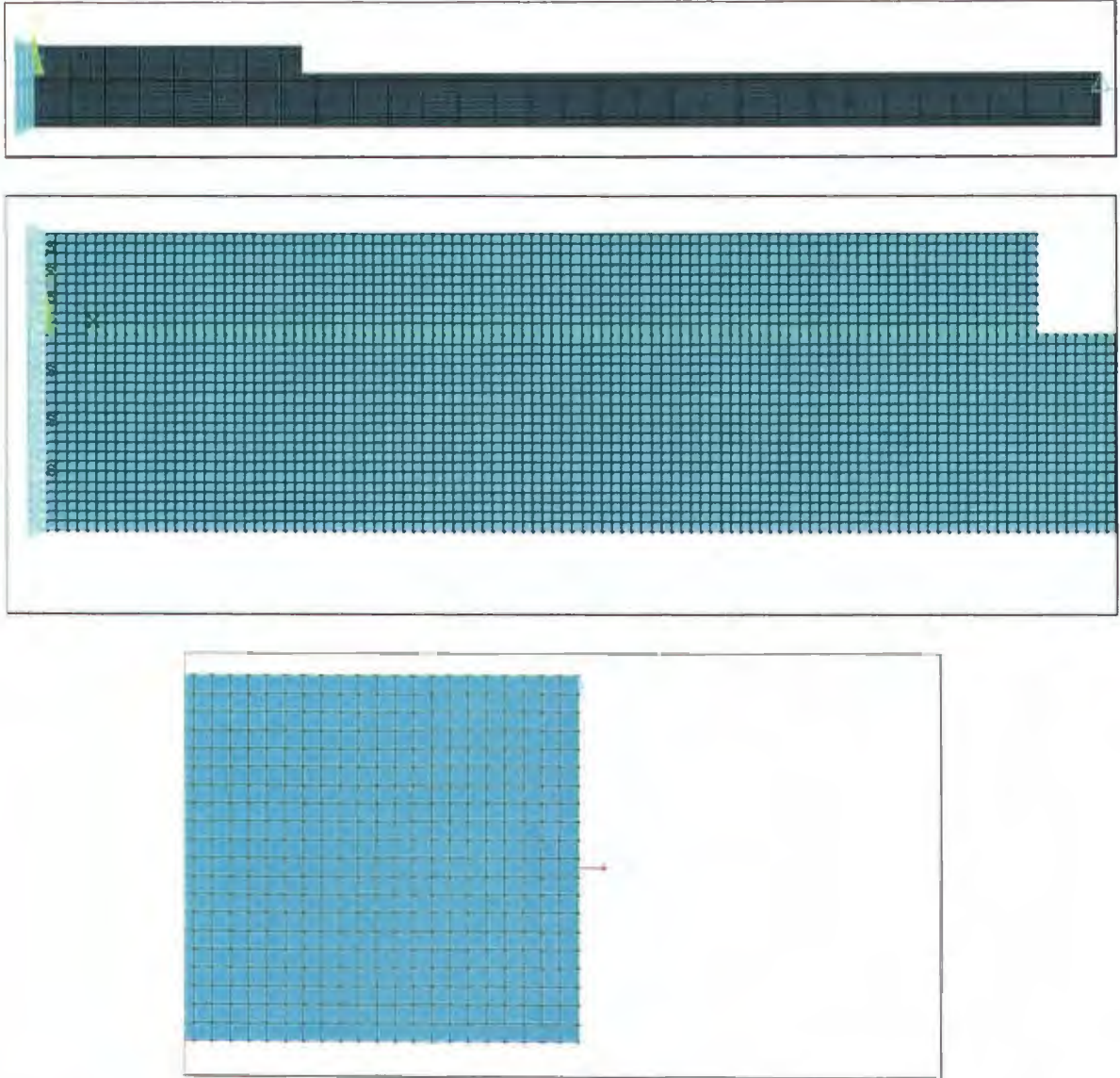
Figure 3.4. Element plot for the single-sided bonded joint model in ANSYS™; full model (top), symmetry BCs (middle), and applied load (bottom).

33
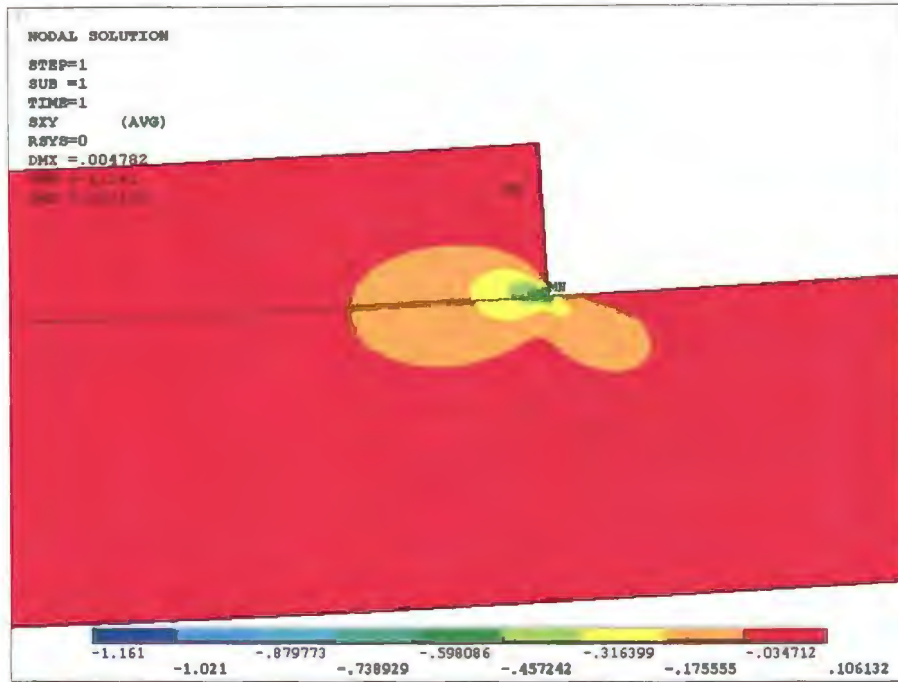
(a)
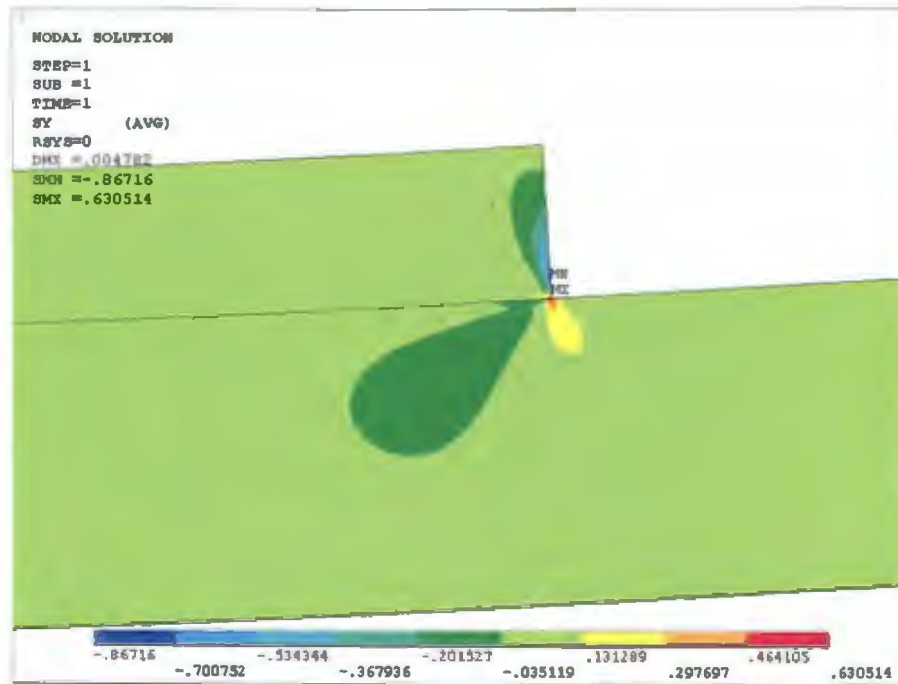
(b)

Figure 3.5. FEA contour plots showing the (a) shear and (b) normal stress distributions in ANSYS™.

34

a)

(b)
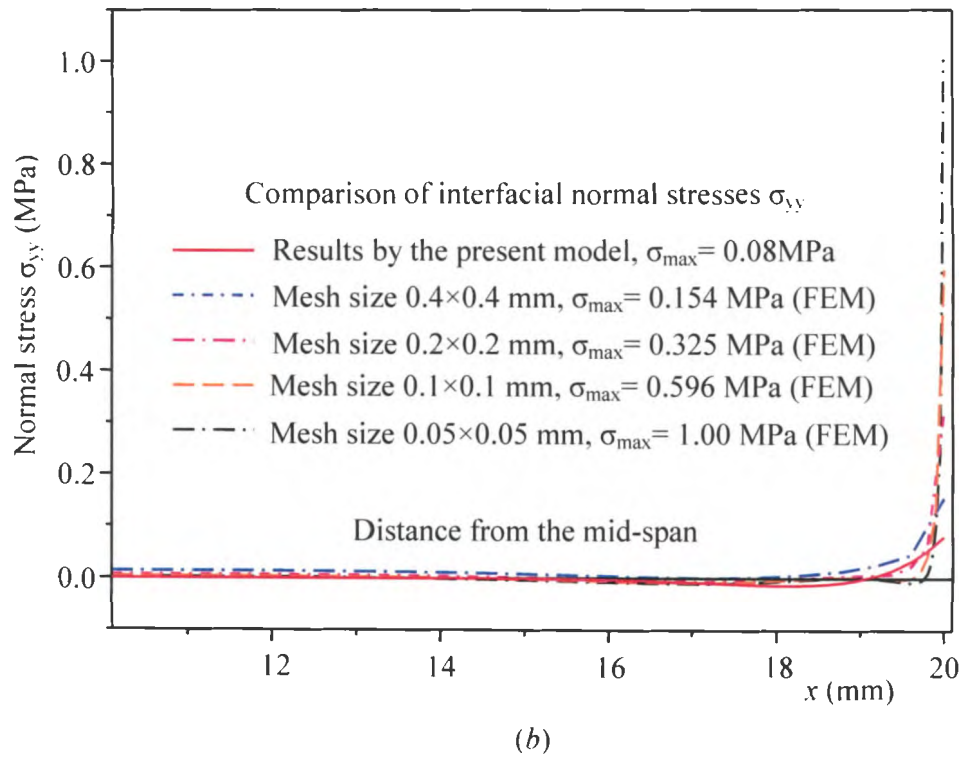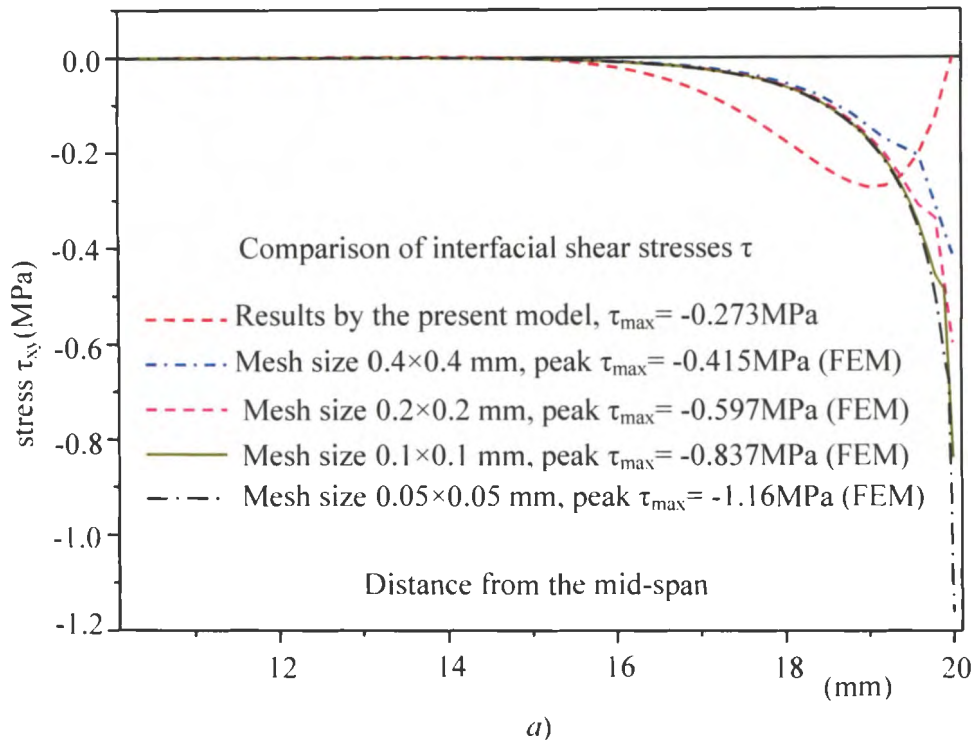
Figure 3.6. Comparison of interfacial shear (*a*) and normal (*b*) stresses predicted by the present method with those obtained via finite element analysis (ANSYS™).
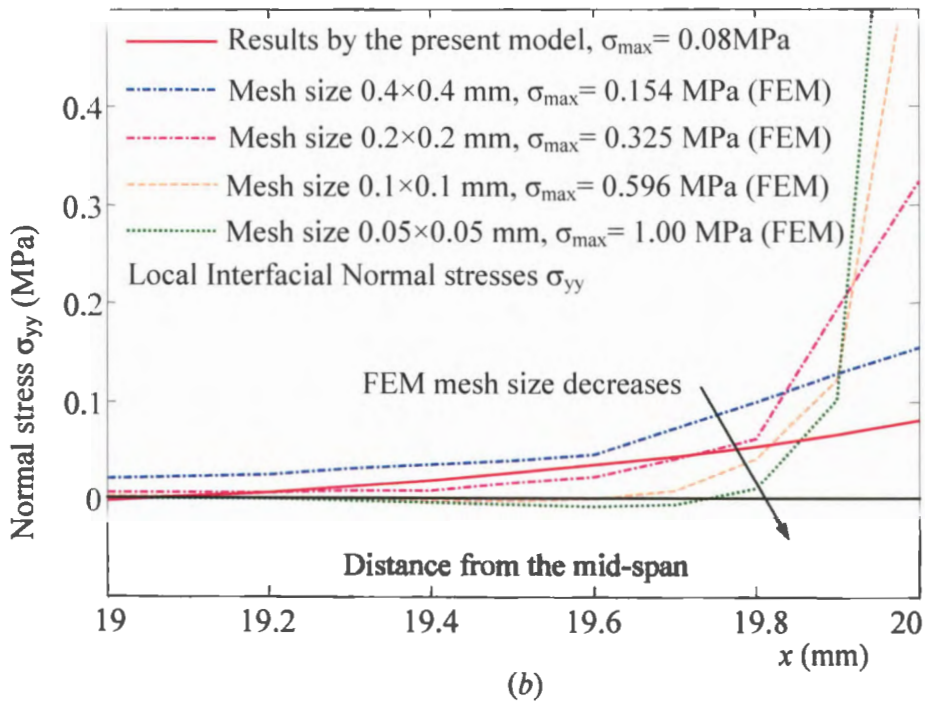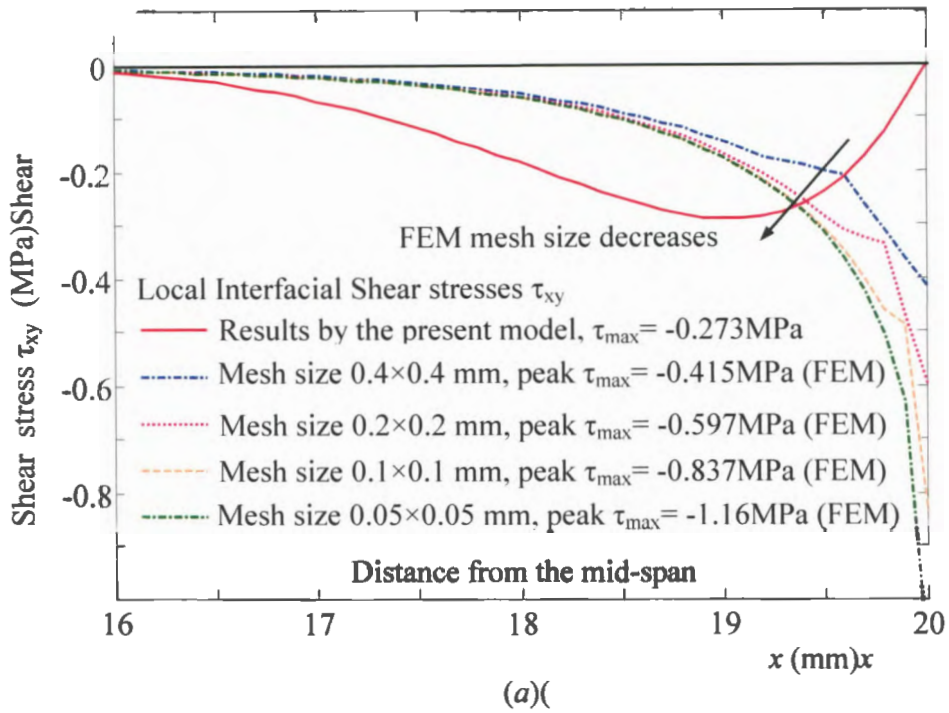
Figure 3.7. Interfacial shear (*a*) and normal (*b*) stress comparison, localized near the free edges of the right half-joint.

3.2.3 Interfacial Stresses Due to Thermal Loads

The single-sided bonded joint of this analysis subjected to purely thermal loads is equivalent to a bimaterial thermostat. The following will consider an aluminum/molybdenum thermostat such as those studied by Suhir (1989 a & b), Eischen et al. (1990) and Ru (2002). The joint parameters for this study are as follows: $E_1 = 70$ GPa, $v_1 = 0.345$, $h_1 = 2.5$ mm for the cover layer, and $E_2 = 325$ GPa, $v_2 = 0.293$, and $h_2 = 2.5$ mm for the substrate layer. Thermal expansion coefficients for the materials are $\alpha_1 = 23.6 \times 10^{-6} / °C$ and $\alpha_2 = 4.9 \times 10^{-6} / °C$; the joint is $L = 50.8$ mm long and subjected to uniform temperature change $\Delta T = 240 °C$ in *plane-strain*. The interfacial shear and normal stresses (τ and σ, respectively) are calculated from (3.59) and (3.62) as

$$\tau = 6.60932 \times 10^{-9} \left[2.33459 \sinh(0.933937x) - 1.04659 \times 10^{-9} \sinh(1.7813x) \right] \text{MPa} \quad (3.74)$$

$$\sigma = 5.24334 \times 10^{-9} \left[2.18013 \cosh(0.933937x) - 1.86429 \times 10^{-9} \cosh(1.7813x) \right] \text{MPa} \quad (3.75)$$

Figure 3.8 shows the distribution of interfacial shear and normal stresses in a bimaterial thermostat (single-sided bonded joint) subjected purely to uniform temperature change. As expected, the figures show high stress concentration near the free edges of the joint; these stresses are in a good agreement with those found in the literature. For instance, the present model predicts a peak value of interfacial normal stress $\sigma_{max} = 103.7$ MPa very close to the value predicted by Eischen et al. (1990) of $\sigma_{max} = 102.8$ MPa. Also, the location of the peak value of interfacial shear stress is found at a distance of approximately $L/25$ from the free edges; this value is close (although slightly further from the free edges) to those found in the literature [e.g. the Chen and Cheng (1983) result that located the peak stress at a distance of approximately 20% the adherend thickness from the edge].
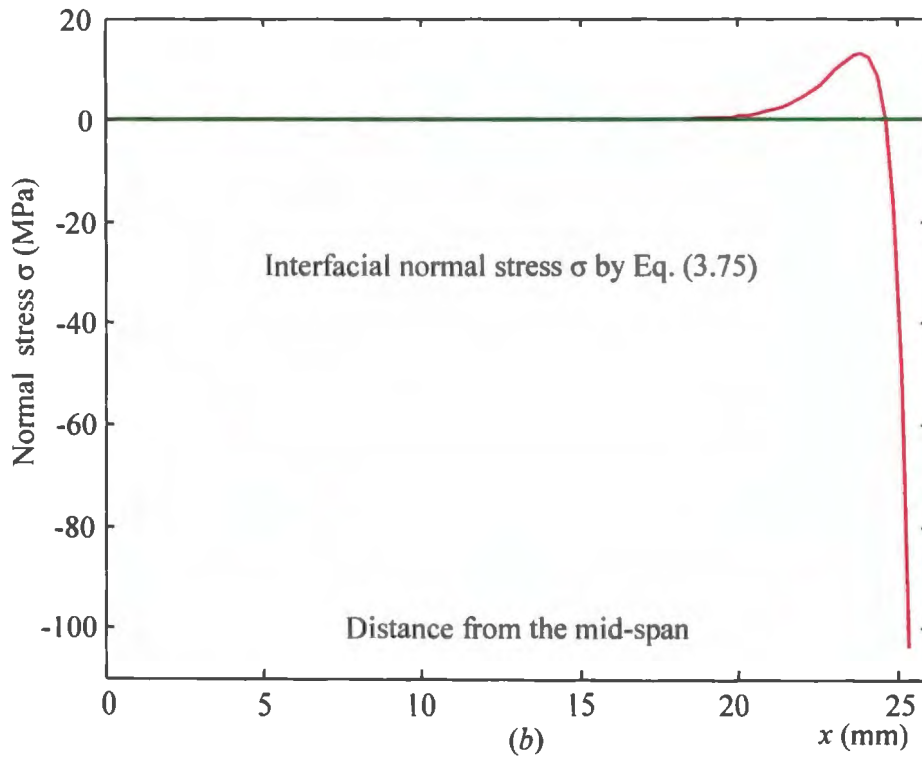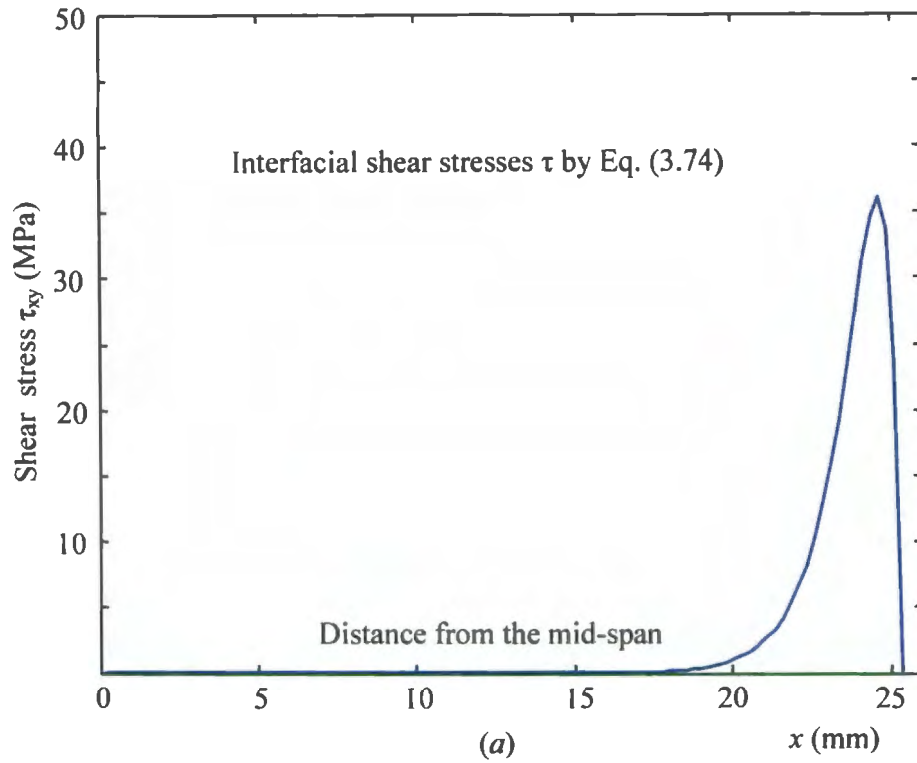
Figure 3.8. Interfacial shear (*a*) and normal (*b*) stresses of a bimaterial thermostat subjected to uniform temperature change.

3.2.4 Conclusions

This chapter has presented a novel analytic approach to the interfacial stress analysis of bonded joints subjected to axial tension and uniform temperature change. All planar stress components were defined in terms of two unknown interfacial stress functions f and g using classic *Euler-Bernoulli* beam theory and 2D elasticity. An approximate deformation compatibility constraint was introduced to correlate the stress functions f and g in the form of equal curvature of the adherends. Through minimization of the total complementary strain energy of the joint, a governing 4th-order ODE of constant coefficients in the shear stress function f was determined and solved explicitly.

There are several technical advantages of the current model; the first of these is that the interfacial stresses are explicitly determined in the analytic solution. Also, all BCs are satisfied in the derivation, including the shear stress-free condition at the free edges of the adherends. Furthermore, all pertinent material and geometric parameters (Young's moduli, Poisson's ratios, thickness ratios, etc.) have been fully incorporated into the solution, yielding a model well-suited to scaling analysis and joint design that gives insight into the variational behavior of interfacial stresses in bonded joints. The method has been validated by comparison with finite element models, and it has been shown to agree with elementary mechanics of materials in the asymptotic case (sufficiently long and slender joints).

There remain some technical deficiencies in the present model, including the approximate deformation compatibility constraint. Equating the curvatures of the adherends of a bonded joint allows for the interfacial stress functions f and g to be correlated, but this requirement is a weak approximation which may lead to noticeable deviation in refined stress analysis of bonded joints as seen above. Furthermore, while the

FEA comparison did provide evidence for the validation of the model, the noticeable deviations of results between the FEM and analytic methods indicate that further refinements to the process can be made.

In the following chapter, refinements to the stress-function variational method are made and applied to the analyses of single-sided strap joints and single-lap joints under mechanical and thermal loads. The approximate deformation compatibility constraint (i.e. equal curvature of adherends) is removed from the derivation, leading to a system of two coupled 4th-order ODEs in terms of the interfacial stress functions f and g. The improved method is validated through comparison with detailed FE analyses of the joints, and scaling analyses are performed to provide insight into the scaling behavior of interfacial stresses with changing joint parameters.

4. GENERALIZED STRESS-FUNCTION VARIATIONAL

METHOD

4.1 Problem Formulation—Single-Sided Strap Joint

4.1.1 Model Formulation

To begin, consider the single-sided strap joint shown in Figure 4.1 consisting of two identical slender substrate layers and a slender cover layer. The thicknesses of the upper and lower adherends are h_1 and h_2, respectively; the length of the cover layer is L and all adherends have width b. The x-coordinate is taken from the symmetric mid-span of the joint and directed along the axis, while the vertical coordinates y_1 and y_2 are directed upward from the centroids of the cross-sections of their respective layers. The joint is subjected to uniform tensile stress p_0 on the substrate layer far from the cover layer and a uniform temperature change ΔT from the temperature of a thermal stress-free state. Subsequent analysis of the joint will consider only the right half-portion due to the symmetry of both the joint geometry and loads (see Figure 4.2 for representative segmental elements of the cover layer and right substrate). As in the analysis of the previous chapter, the joint is in a complicated 3D stress state due to the mismatch of material properties across the interface; to simplify the derivation, two limiting planar cases are to be considered, i.e. the *plane-stress* or *plane-strain* state. As before, the adherends are taken to be isotropic, linearly thermoelastic solids. For convenience, all subsequent variables with subscripts 1 and 2 refer to the cover layer and substrate, respectively.
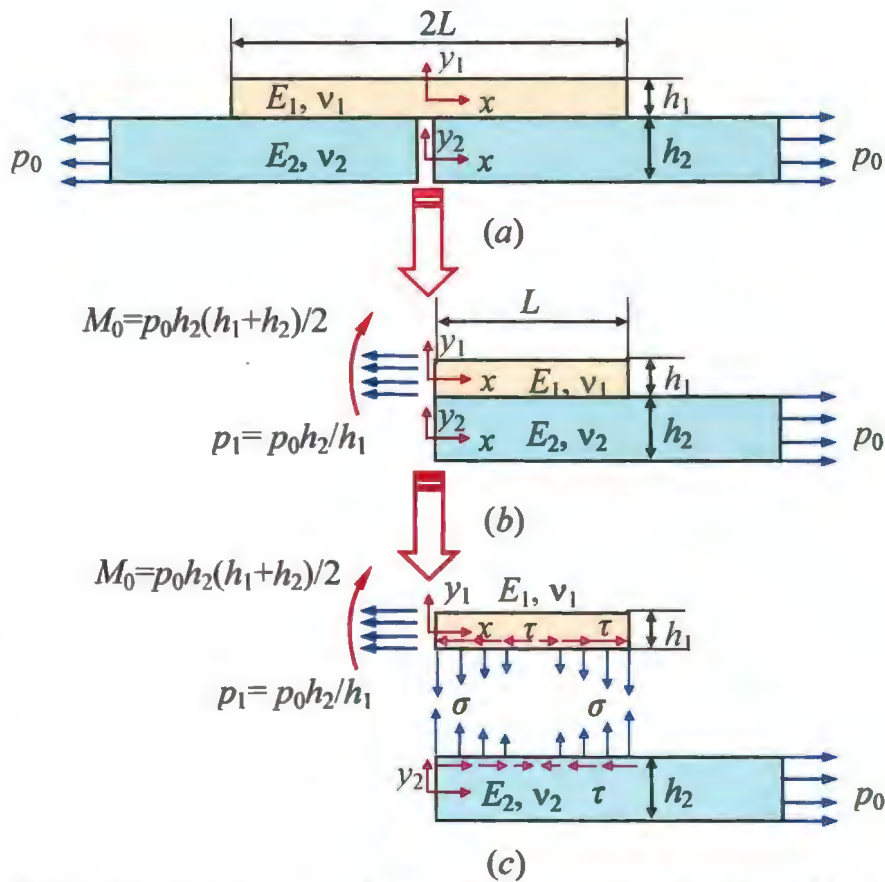
Figure 4.1. Schematic of a single-sided strap joint consisting of (a) two identical substrate layers and a slender cover layer; the reduced right half-joint (based on symmetry) is shown in (b), and (c) depicts the interfacial stresses in the joint.
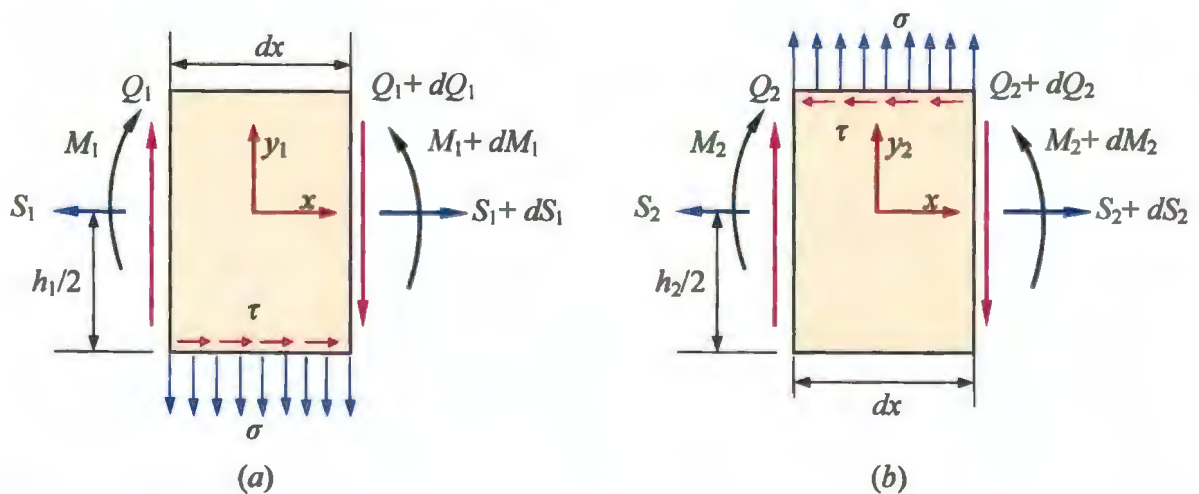
Figure 4.2. FBDs of representative segmental elements of (a) the cover layer and (b) the right substrate.

42

4.1.2 Static Equilibrium Equations

The loss of lateral symmetry of the single-sided strap joint results in a combination of in-plane elongation and lateral deflection under the influences of axial tension and/or uniform temperature change. Because the joint adherends are considered to be slender enough, they may be analyzed as *Euler-Bernoulli* beams. Figure 4.2 shows free-body-diagrams (FBDs) of representative elements of the cover layer and substrate; note that the stresses, forces and moments are defined according to standard sign conventions from elementary *Mechanics of Materials* (Beer et al., 2009). For the element of the cover layer, the static equilibrium equations are:

$$\Sigma F_x = 0: \qquad \frac{dS_1}{dx} = -b\tau \tag{4.1}$$

$$\Sigma F_y = 0: \qquad \frac{dQ_1}{dx} = -b\sigma \tag{4.2}$$

$$\Sigma M = 0: \qquad \frac{dM_1}{dx} = Q_1 - \frac{h_1}{2}(b\tau) \tag{4.3}$$

Similarly, the relevant static equilibrium equations for the right substrate layer are:

$$\Sigma F_x = 0: \qquad \frac{dS_2}{dx} = b\tau \tag{4.4}$$

$$\Sigma F_y = 0: \qquad \frac{dQ_2}{dx} = b\sigma \tag{4.5}$$

$$\Sigma M = 0: \qquad \frac{dM_2}{dx} = Q_2 - \frac{h_2}{2}(b\tau) \tag{4.6}$$

43

4.1.3 Stress Resultants

The interfacial shear (τ) and normal (σ) stress are defined as two independent, as-yet-unknown functions:

$$\tau = f(x) \quad \text{and} \quad \sigma = g(x) \tag{4.7}$$

The shear stress-free condition at the free edges of the adherends requires that:

$$f(0) = f(L) = 0 \tag{4.8}$$

Furthermore, the physical conditions of the axial traction, transverse shear force and bending moments at the joint free edges can be expressed as:

$$S_1(0) = p_0 b h_2 \tag{4.9}$$

$$S_1(L) = 0 \tag{4.10}$$

$$Q_1(0) = 0 \tag{4.11}$$

$$Q_1(L) = 0 \tag{4.12}$$

$$M_1(0) = M_0 = p_0 b h_2 (h_1 + h_2)/2 \tag{4.13}$$

$$M_1(L) = 0 \tag{4.14}$$

$$S_2(0) = 0 \tag{4.15}$$

$$S_2(L) = p_0 b h_2 \tag{4.16}$$

$$Q_2(0) = 0 \tag{4.17}$$

$$Q_2(L) = 0 \tag{4.18}$$

$$M_2(0) = 0 \tag{4.19}$$

$$M_2(L) = 0 \tag{4.20}$$

Two important notes about the above BCs: firstly, of the fourteen BCs listed in (4.8) through (4.20), only eight are linearly independent (this will be dealt with in Section 4.1.5). Furthermore, for the case of the bonded joint subjected only to uniform temperature change, the BCs in (4.9), (4.13), and (4.16) would all become trivial, resulting in the problem being reduced to that of the bimaterial thermostat such as those studied by Timoshenko (1925) and Suhir (1986, 1989a &1989b).

Just as in the preceding chapter, the stress resultants for segmental elements of both adherends can be expressed in terms of f and g by integrating Eqs. (4.1) through (4.6) with respect to x and applying the pertinent BCs as follows: for example, integrating (4.1) from $x = 0$ yields

$$\int_0^x dS_1 = -\int_0^x bf(\xi)\,d\xi \tag{4.21}$$

By applying the BC at the left edge of the upper adherend [which is Eq. (4.9)], the axial normal force in the cover layer is determined to be

$$S_1(x) = p_0 b h_2 - b\int_0^x f(\xi)\,d\xi \tag{4.22}$$

Similarly, the shear force in the cover layer is found via integration of (4.1) with respect to x:

$$\int_0^x dQ_1 = -\int_0^x bg(\xi)\,d\xi \tag{4.23}$$

Applying the BC from Eq. (4.11) gives:

$$Q_1(x) = -b\int_0^x g(\xi)\,d\xi \tag{4.24}$$

Integration of (4.3) with respect to x yields

$$\int_0^x dM_1 = \int_0^x \left[Q_1(\xi) - \frac{h_1}{2}(b\tau) \right] d\xi \tag{4.25}$$

45

Once more, applying the bending moment condition from (4.13) gives the bending moment for the cover layer as

$$M_1(x) = M_0 - b \int_0^x \int_0^\xi g(\varsigma)\, d\varsigma\, d\xi - \frac{bh_1}{2} \int_0^x f(\xi)\, d\xi \qquad (4.26)$$

By using the same procedure outlined above, the resultants in the right substrate layer can be determined as:

$$S_2(x) = b \int_0^x f(\xi)\, d\xi \qquad (4.27)$$

$$Q_2(x) = b \int_0^x g(\xi)\, d\xi \qquad (4.28)$$

$$M_2(x) = b \int_0^x \int_0^\xi g(\varsigma)\, d\varsigma\, d\xi - \frac{bh_2}{2} \int_0^x f(\xi)\, d\xi \qquad (4.29)$$

4.1.4 Stress Components

Because the adherends of the joint under consideration are slender enough, they may be modeled as *Euler-Bernoulli* beams. Therefore, the axial normal stress in the components of the joint can be described by the *Euler-Bernoulli* flexural stress formula; for the cover layer, this is expressed as

$$\sigma_{xx}^{(1)} = \frac{S_1}{bh_1} - \frac{M_1 y_1}{I_1} = p_1 - \frac{1}{h_1} \int_0^x f(\xi)\, d\xi - \frac{12 y_1}{h_1^3} \left[M_0 - \int_0^x \int_0^\xi g(\varsigma)\, d\varsigma\, d\xi - \frac{h_1}{2} \int_0^x f(\xi)\, d\xi \right] \qquad (4.30)$$

Subsequently, the shear stress $\tau_{y_1 x}^{(1)}$ can be found using the equilibrium equation (2D elasticity) of a representative element:

$$\frac{\partial \sigma_{xx}^{(1)}}{\partial x} + \frac{\partial \tau_{y_1 x}^{(1)}}{\partial y_1} = 0 \qquad (4.31)$$

46

Integration of (4.31) with respect to y_1 from an arbitrary choice of y to the top surface of

the adherend:

$$\int_{y_1}^{h_1/2} \frac{\partial \sigma_{xx}^{(1)}}{\partial x} \, dy_1 + \int_{y_1}^{h_1/2} \frac{\partial \tau_{y_1 x}^{(1)}}{\partial y_1} \, dy_1 = 0 \qquad (4.32)$$

and applying the traction-free BC $\tau_{y_1 x}^{(1)}(h_1/2) = 0$ at the free surface of the adherend leads to

the shear stress in the cover layer:

$$\tau_{y_1 x}^{(1)} = -\frac{1}{h_1}\left[\left(\frac{h_1}{2} - y_1\right) - \frac{3}{h_1}\left(\frac{h_1^2}{4} - y_1^2\right)\right] f(x) + \frac{6}{h_1^3}\left(\frac{h_1^2}{4} - y_1^2\right)\int_0^x g(\xi)\, d\xi \qquad (4.33)$$

Similarly, the 2D equilibrium equation

$$\frac{\partial \sigma_{y_1 y_1}^{(1)}}{\partial y_1} + \frac{\partial \tau_{xy_1}^{(1)}}{\partial x} = 0 \qquad (4.34)$$

can be integrated with respect to y_1 from an arbitrary location in the adherend to the top

free surface as follows:

$$\int_{y_1}^{h_1/2} \frac{\partial \sigma_{y_1 y_1}^{(1)}}{\partial y_1} \, dy_1 + \int_{y_1}^{h_1/2} \frac{\partial \tau_{xy_1}^{(1)}}{\partial x} \, dy_1 = 0 \qquad (4.35)$$

to give the transverse normal stress in the cover layer:

$$\sigma_{y_1 y_1}^{(1)} = -\frac{1}{h_1}\left\{\frac{h_1}{2}\left(\frac{h_1}{2} - y_1\right) - \frac{1}{2}\left(\frac{h_1^2}{4} - y_1^2\right) - \frac{3}{h_1}\left[\frac{h_1^2}{4}\left(\frac{h_1}{2} - y_1\right) - \frac{1}{3}\left(\frac{h_1^3}{8} - y_1^3\right)\right]\right\} f'(x)$$
$$+ \frac{6}{h_1^3}\left[\frac{h_1^2}{4}\left(\frac{h_1}{2} - y_1\right) - \frac{1}{3}\left(\frac{h_1^3}{8} - y_1^3\right)\right] g(x) \qquad (4.36)$$

This same method can be applied to the substrate layer to obtain the corresponding

stress components. The axial normal stress is found using the flexural stress formula for

Euler-Bernoulli beams:

$$\sigma_{xx}^{(2)} = \frac{S_2}{bh_2} - \frac{M_2 y_2}{I_2} = \frac{1}{h_2}\int_0^x f(\xi)\, d\xi - \frac{12 y_2}{h_2^3}\left[\int_0^x \int_0^\xi g(\varsigma)\, d\varsigma\, d\xi - \frac{h_2}{2}\int_0^x f(\xi)\, d\xi\right] \qquad (4.37)$$

47

Once again, the 2D equilibrium equation is integrated with respect to y_2 to determine the shear stress in the substrate layer; however, in this case the integration is carried out from the bottom surface at $y_2 = -h_2/2$ (stress-free surface) to an arbitrary choice of y_2 as follows:

$$\int_{-h_2/2}^{y_2} \frac{\partial \sigma_{xx}^{(2)}}{\partial x}\, dy_2 + \int_{-h_2/2}^{y_2} \frac{\partial \tau_{y_2 x}^{(2)}}{\partial y_2}\, dy_2 = 0 \tag{4.38}$$

Solving (4.38) for the shear stress in the substrate layer yields

$$\tau_{y_2 x}^{(2)} = -\frac{1}{h_2}\left[\left(y_2 + \frac{h_2}{2}\right) + \frac{3}{h_2}\left(y_2^2 - \frac{h_2^2}{4}\right)\right] f(x) + \frac{6}{h_2^3}\left(y_2^2 - \frac{h_2^2}{4}\right)\int_0^x g(\xi)\, d\xi \tag{4.39}$$

The transverse normal stress $\sigma_{y_2 y_2}^{(2)}$ in the substrate layer is determined by integrating the corresponding equilibrium equation with respect to y_2 from the bottom surface to an arbitrary y_2:

$$\int_{-h_2/2}^{y_2} \frac{\partial \sigma_{y_2 y_2}^{(2)}}{\partial y_2}\, dy_2 + \int_{-h_2/2}^{y_2} \frac{\partial \tau_{xy_2}^{(2)}}{\partial x}\, dy_2 = 0 \tag{4.40}$$

This leads to the transverse normal stress in the substrate

$$\begin{aligned}
\sigma_{y_2 y_2}^{(2)} = &\left\{\frac{1}{h_2}\left[\frac{1}{2}\left(y_2^2 - \frac{h_2^2}{4}\right) + \frac{h_2}{2}\left(y_2 + \frac{h_2}{2}\right)\right] + \frac{3}{h_2^2}\left[\frac{1}{3}\left(y_2^3 + \frac{h_2^3}{8}\right) - \frac{h_2^2}{4}\left(y_2 + \frac{h_2}{2}\right)\right]\right\} f'(x) \\
&- \frac{6}{h_2^3}\left[\frac{1}{3}\left(y_2^3 + \frac{h_2^3}{8}\right) - \frac{h_2^2}{4}\left(y_2 + \frac{h_2}{2}\right)\right] g(x)
\end{aligned} \tag{4.41}$$

4.1.5 Governing Equations of Interfacial Stresses

With the stress components in the cover and substrate layers defined by (4.30), (4.33), (4.36), (4.37), (4.39), and (4.41), the strain energy of the right half-joint can be defined as

48

$$U = b \int_0^{l} \int_{-h_1/2}^{h_1/2} \left\{ \frac{1}{2} \left[\sigma_{xx}^{(1)} \varepsilon_{xx}^{(1)} + \sigma_{yy}^{(1)} \varepsilon_{yy}^{(1)} \right] + \frac{1+\upsilon_1}{E_1} \left(\tau_{xy_1}^{(1)} \right)^2 \right\} dx \, dy_1$$

$$+ b \int_0^{l} \int_{-h_2/2}^{h_2/2} \left\{ \frac{1}{2} \left[\sigma_{xx}^{(2)} \varepsilon_{xx}^{(2)} + \sigma_{yy}^{(2)} \varepsilon_{yy}^{(2)} \right] + \frac{1+\upsilon_1}{E_1} \left(\tau_{xy_2}^{(2)} \right)^2 \right\} dx \, dy_2 \qquad (4.42)$$

where the axial and transverse normal strains in the adherends are defined according to

generalized Hooke's law for isotropic, linearly thermoelastic solids (*plane-stress*):

$$\varepsilon_{xx}^{(i)} = \frac{1}{E_i} \sigma_{xx}^{(i)} - \frac{\upsilon_i}{E_i} \sigma_{yy}^{(i)} + \alpha_i \Delta T$$

$$\varepsilon_{yy}^{(i)} = \frac{1}{E_i} \sigma_{yy}^{(i)} - \frac{\upsilon_i}{E_i} \sigma_{xx}^{(i)} + \alpha_i \Delta T \qquad (4.43)$$

where α_i ($i = 1, 2$) are the thermal expansion coefficients for the upper and lower

adherends, respectively; ΔT represents the uniform temperature change from the thermal

stress-free state. Due to the removal of the approximate deformation compatibility

constraint (equal adherend curvature) from the previous chapter, the strain energy is now a

functional with respect to the two unknown interfacial stress functions, both f and g. The

theorem of minimum complementary strain energy is again invoked such that $\delta U = 0$, or

$$b \int_0^{l} \int_{-h_1/2}^{h_1/2} \left\{ \frac{1}{2} \left[\sigma_{xx}^{(1)} \delta \varepsilon_{xx}^{(1)} + \delta \sigma_{xx}^{(1)} \varepsilon_{xx}^{(1)} + \sigma_{yy}^{(1)} \delta \varepsilon_{yy}^{(1)} + \delta \sigma_{yy}^{(1)} \varepsilon_{yy}^{(1)} \right] + \frac{2(1+\upsilon_1)}{E_1} \tau_{xy_1}^{(1)} \delta \tau_{xy_1}^{(1)} \right\} dx \, dy_1$$

$$+ b \int_0^{l} \int_{-h_2/2}^{h_2/2} \left\{ \frac{1}{2} \left[\sigma_{xx}^{(2)} \delta \varepsilon_{xx}^{(2)} + \delta \sigma_{xx}^{(2)} \varepsilon_{xx}^{(2)} + \sigma_{yy}^{(2)} \delta \varepsilon_{yy}^{(2)} + \delta \sigma_{yy}^{(2)} \varepsilon_{yy}^{(2)} \right] + \frac{2(1+\upsilon_2)}{E_2} \tau_{xy_2}^{(2)} \delta \tau_{xy_2}^{(2)} \right\} dx \, dy_2 = 0$$

$$(4.44)$$

where δ is the variational operator with respect to f or g.

Now the stress expressions (4.30), (4.33), (4.36), (4.37), (4.39), (4.41) and (4.43)

are substituted into (4.44), and the appropriate variational operations are performed. After

integration of the strain energy and some simplification, the governing equation of

interfacial stresses is determined: a system of two coupled 4th-order ODEs of constant coefficients:

$$A_{11}F^{(IV)}(\xi) + A_{12}G^{(IV)}(\xi) + B_{11}F''(\xi) + B_{12}G''(\xi) + C_{11}F(\xi) + C_{12}G(\xi) + D_1 = 0$$
$$A_{12}F^{(IV)}(\xi) + A_{22}G^{(IV)}(\xi) + B_{12}F''(\xi) + B_{22}G''(\xi) + C_{12}F(\xi) + C_{22}G(\xi) + D_2 = 0$$

(4.45)

where

$$F(\xi) = F(x/h_2) = -\frac{1}{p_0 h_2}\int_0^x f(\zeta)\,d\zeta$$

$$G(\xi) = G(x/h_2) = \frac{1}{p_0 h_2^2}\int_0^x \int_0^\zeta g(\eta)\,d\eta\,d\zeta$$

(4.46)

$$A_{11} = \frac{1}{105}(h_{12}^3 + e_{12})$$

$$A_{12} = \frac{11}{210}(-h_{12}^2 + e_{12})$$

$$A_{22} = \frac{13}{35}(h_{12} + e_{12})$$

(4.47)

$$B_{11} = -\frac{4}{15}(h_{12} + e_{12})$$

$$B_{12} = \frac{1}{5}\left[(1 - 5v_1) - (1 - 5v_2)e_{12}\right]$$

$$B_{22} = -\frac{12}{5}(h_{12}^{-1} + e_{12})$$

(4.48)

$$C_{11} = 4(h_{12}^{-1} + e_{12})$$

$$C_{12} = 6(-h_{12}^{-2} + e_{12})$$

$$C_{22} = 12(h_{12}^{-3} + e_{12})$$

(4.49)

$$D_1 = \begin{cases} (3 + 4h_{12})h_{12}^{-2} + \dfrac{1}{2}(\alpha_1 - \alpha_2)\Delta TE_1 / p_0, \\ \quad \text{(for combined mechanical and thermal loads--}plane - stress) \\[4pt] (3 + 4h_{12})h_{12}^{-2} + \dfrac{1}{2}\left[(1 + v_1)\alpha_1 - (1 + v_2)\alpha_2\right]\Delta TE_1 / p_0, \\ \quad \text{(for combined mechanical and thermal loads--}plane - strain) \\[4pt] (3 + 4h_{12})h_{12}^{-2}, \quad \text{(for pure mechanical load--either } plane - stress \text{ or } plane - strain) \\[4pt] \dfrac{1}{2}(\alpha_1 - \alpha_2)\Delta TE_1 / p_0, \quad \text{(for pure thermal load--}plane - stress) \\[4pt] \dfrac{1}{2}\left[(1 + v_1)\alpha_1 - (1 + v_2)\alpha_2\right]\Delta TE_1 / p_0, \quad \text{(for pure thermal load--}plane - strain) \end{cases} \tag{4.50}$$

$$D_2 = \begin{cases} -6(1 + h_{12})h_{12}^{-3}, & \text{(for pure mechanical or combined mechanical and thermal loads)} \\ 0, & \text{(for pure thermal loads)} \end{cases} \tag{4.51}$$

Also in the above, there are two parameter ratios defined: $h_{12} = h_1 / h_2$ and $e_{12} = E_1 / E_2$. It is important to note that when pure thermal loads (uniform temperature change) are considered in the analysis, the stress p_0 in (4.50) and (4.51) is taken as a reference stress for dimensionless analysis, as is its purpose in (4.46). Another feature to note is that the governing equations can be readily converted to the *plane-strain* case by replacing the parameters E_i with $E_i / (1 - v_i^2)$, v_i with $v_i / (1 - v_i)$, and α_i with $\alpha_i(1 + v_i)$.

Now the system of governing equations can be recast in matrix form:

$$\begin{bmatrix} A_{11} & A_{12} \\ A_{12} & A_{22} \end{bmatrix} \begin{Bmatrix} F^{(IV)}(\xi) \\ G^{(IV)}(\xi) \end{Bmatrix} + \begin{bmatrix} B_{11} & B_{12} \\ B_{12} & B_{22} \end{bmatrix} \begin{Bmatrix} F''(\xi) \\ G''(\xi) \end{Bmatrix} + \begin{bmatrix} C_{11} & C_{12} \\ C_{12} & C_{22} \end{bmatrix} \begin{Bmatrix} F(\xi) \\ G(\xi) \end{Bmatrix} + \begin{Bmatrix} D_1 \\ D_2 \end{Bmatrix} = \begin{Bmatrix} 0 \\ 0 \end{Bmatrix} \tag{4.52}$$

or, in a more concise form:

$$[A]\{\Phi^{(IV)}\} + [B]\{\Phi''\} + [C]\{\Phi\} + \{D\} = \{0\} \tag{4.53}$$

where [A], [B] and [C] are symmetric, real 2×2 matrices:

$$[A] = [A]^T = \begin{bmatrix} A_{11} & A_{12} \\ A_{12} & A_{22} \end{bmatrix} \tag{4.54}$$

$$[B] = [B]^{\mathrm{T}} = \begin{bmatrix} B_{11} & B_{12} \\ B_{12} & B_{22} \end{bmatrix} \qquad (4.55)$$

$$[C] = [C]^{\mathrm{T}} = \begin{bmatrix} C_{11} & C_{12} \\ C_{12} & C_{22} \end{bmatrix} \qquad (4.56)$$

and $\{\Phi\}$, $\{D\}$, and $\{0\}$ are the vectors:

$$\{\Phi\} = \{F(\xi), G(\xi)\}^T \qquad (4.57)$$

$$\{D\} = \{D_1, D_2\}^T \qquad (4.58)$$

$$\{0\} = \{0, 0\}^T \qquad (4.59)$$

Now the solution of (4.53) can be expressed as the superposition of the general solution $\{\Psi\}$ of the corresponding homogeneous system and the particular solution $\{\Phi_0\}$ such that

$$\{\Phi\} = \{\Psi\} + \{\Phi_0\} \qquad (4.60)$$

where

$$[A]\{\Psi^{(IV)}\} + [B]\{\Psi''\} + [C]\{\Psi\} = \{0\} \qquad (4.61)$$

and

$$\{\Phi_0\} = -[C]^{-1}\{D\} \qquad (4.62)$$

The homogeneous system of (4.61) is solved by assuming the general solution must be of the form

$$\{\Psi\} = \{\Psi_0\}\exp(\lambda\xi) \qquad (4.63)$$

where λ and $\{\Psi_0\}$ are the eigenvalue and eigenvector, respectively, of the corresponding characteristic equation for (4.61):

$$\lambda^4[A]\{\Psi_0\} + \lambda^2[B]\{\Psi_0\} + [C]\{\Psi_0\} = \{0\} \qquad (4.64)$$

We can convert the problem of (4.64) to a generalized eigenvalue problem by introducing

52

$$\{\Psi_1\} = \lambda^2 \{\Psi_0\}$$ (4.65)

such that the system can be rearranged as

$$\begin{bmatrix} I & 0 \\ 0 & A \end{bmatrix} \begin{Bmatrix} \Psi_0 \\ \Psi_1 \end{Bmatrix} = -\lambda^{-2} \begin{bmatrix} 0 & -I \\ C & B \end{bmatrix} \begin{Bmatrix} \Psi_0 \\ \Psi_1 \end{Bmatrix}$$ (4.66)

This generalized eigenvalue problem can be solved efficiently by any of several robust numerical algorithms available in the literature [for example the "eig( )" function in Matlab™]. Now the expression of the general solution (4.60) becomes

$$\{\Phi\} = \sum_{k=1}^{4} \left[c_k \{\Psi_0^k\} \exp(\lambda_k \xi) + d_k \{\Psi_0^k\} \exp(-\lambda_k \xi) \right] + \{\Phi_0\}$$ (4.67)

In (4.67), note that $\{\Psi_0^k\}$ ($k = 1, 2, 3, 4$) are the eigenvectors associated to the eigenvalues λ_k ($k = 1, 2, 3, 4$); c_k and d_k are the constants (may be real or complex) to be determined by the BCs from (4.8) through (4.20). During the application of these BC equations, it is found that only eight are linearly independent; the system reduces to the following eight BCs to determine the constants c_k and d_k:

$$F(0) = 0$$ (4.68)

$$F(L/h_2) = -1$$ (4.69)

$$F'(0) = 0$$ (4.70)

$$F'(L/h_2) = 0$$ (4.71)

$$G(0) = 0$$ (4.72)

$$G(L/h_2) = 1/2$$ (4.73)

$$G'(0) = 0$$ (4.74)

$$G'(L/h_2) = 0$$ (4.75)

53

Substituting these BCs into (4.67) yields the following set of linear algebraic equations:

$$\sum_{k=1}^{4} c_k \Psi_0^{k,1} + \sum_{k=1}^{4} d_k \Psi_0^{k,1} = -\Phi_0^{(1)} \tag{4.76}$$

$$\sum_{k=1}^{4} c_k \Psi_0^{k,1} \exp(\lambda_k L / h_2) + \sum_{k=1}^{4} d_k \Psi_0^{k,1} \exp(-\lambda_k L / h_2) = -\left[1 + \Phi_0^{(1)}\right] \tag{4.77}$$

$$\sum_{k=1}^{4} c_k \lambda_k \Psi_0^{k,1} - \sum_{k=1}^{4} d_k \lambda_k \Psi_0^{k,1} = 0 \tag{4.78}$$

$$\sum_{k=1}^{4} c_k \lambda_k \Psi_0^{k,1} \exp(\lambda_k L / h_2) - \sum_{k=1}^{4} d_k \lambda_k \Psi_0^{k,1} \exp(-\lambda_k L / h_2) = 0 \tag{4.79}$$

$$\sum_{k=1}^{4} c_k \Psi_0^{k,2} + \sum_{k=1}^{4} d_k \Psi_0^{k,2} = -\Phi_0^{(2)} \tag{4.80}$$

$$\sum_{k=1}^{4} c_k \Psi_0^{k,2} \exp(\lambda_k L / h_2) + \sum_{k=1}^{4} d_k \Psi_0^{k,2} \exp(-\lambda_k L / h_2) = 1/2 - \Phi_0^{(2)} \tag{4.81}$$

$$\sum_{k=1}^{4} c_k \lambda_k \Psi_0^{k,2} - \sum_{k=1}^{4} d_k \lambda_k \Psi_0^{k,2} = 0 \tag{4.82}$$

$$\sum_{k=1}^{4} c_k \lambda_k \Psi_0^{k,2} \exp(\lambda_k L / h_2) - \sum_{k=1}^{4} d_k \lambda_k \Psi_0^{k,2} \exp(-\lambda_k L / h_2) = 0 \tag{4.83}$$

Note that $\Psi_0^{k,1}$ and $\Psi_0^{k,2}$ ($k = 1, 2, 3, 4$) are the first and second elements, respectively, of the k-th eigenvector; similarly, $\Phi_0^{(1)}$ and $\Phi_0^{(2)}$ are the first and second elements of the particular solution vector $\{\Phi_0\}$. Once again it bears mentioning that for pure thermal loads, the BCs (4.69) and (4.73) should become zero; this will in turn influence the BCs (4.77) and (4.81).

Numerically solving the above set of linear algebraic equations results in the full

determination of the coefficients c_k and d_k; once these constants have been defined, the

interfacial stress functions f and g are completely described by:

$$f(x)/p_0 = \sum_{k=1}^{4} c_k \Psi_0^{k,1} \lambda_k \exp(\lambda_k x / h_2) - \sum_{k=1}^{4} d_k \Psi_0^{k,1} \lambda_k \exp(-\lambda_k x / h_2) \qquad (4.84)$$

$$g(x)/p_0 = \sum_{k=1}^{4} c_k \Psi_0^{k,2} \lambda_k^2 \exp(\lambda_k x / h_2) + \sum_{k=1}^{4} d_k \Psi_0^{k,2} \lambda_k^2 \exp(-\lambda_k x / h_2) \qquad (4.85)$$

With the stress functions f and g explicitly defined by (4.84) and (4.85), all planar stress

components from Section 4.1.4 can also be fully determined. One critical aspect of the

stress-function variational method developed in this chapter is that all the derivations to

this point, with the exception of the traction BCs, are completely independent of joint

configuration. This means that this method is easily and efficiently generalized to virtually

any statically equivalent bonded joint made of two adherends; this generalization will be

explored at the end of this chapter by applying the present method to the single-lap joint

model.

4.2 Model Validation

4.2.1 Interfacial Stresses in a Single-Sided Strap Joint Due to Mechanical Loads

Validation of the current model formulation begins with an analysis of the single-

sided strap joint subjected to uniform axial tension (*plane-stress*); the results of the present

method are compared with those obtained by FEM (ANSYS™). The joint parameters are

identical to those defined in the previous chapter: $E_1 = 200$ GPa, $v_1 = 0.29$, $h_1 = 2$ mm,

$E_2 = 70$ GPa, $v_2 = 0.34$, $h_2 = 4$ mm, and $L = 20$ mm (see Figure 4.1). The adherends have

identical width, b, taken as unity; the uniform tensile stress applied to the substrate is $p_0 = 1$ MPa. The finite element model is constructed in ANSYS™ using four-node (PLANE182) elements and mapped uniform quadrilateral meshes. Just as in Section 3.2.2 of the previous chapter, four mesh sizes of increasing levels of refinement were applied to the model to illustrate the behavior of the stress singularities near the free edges of the joint. Figure 4.3 shows element plots of the relevant regions of the ANSYS™ model; symmetry BCs are applied to the left edge of the upper adherend while the lower adherend edge remains free, and a pressure of 1 MPA is applied to the line of the right edge to represent uniform tensile stress. The contour stress plots created using ANSYS™ are shown in Figure 4.4.
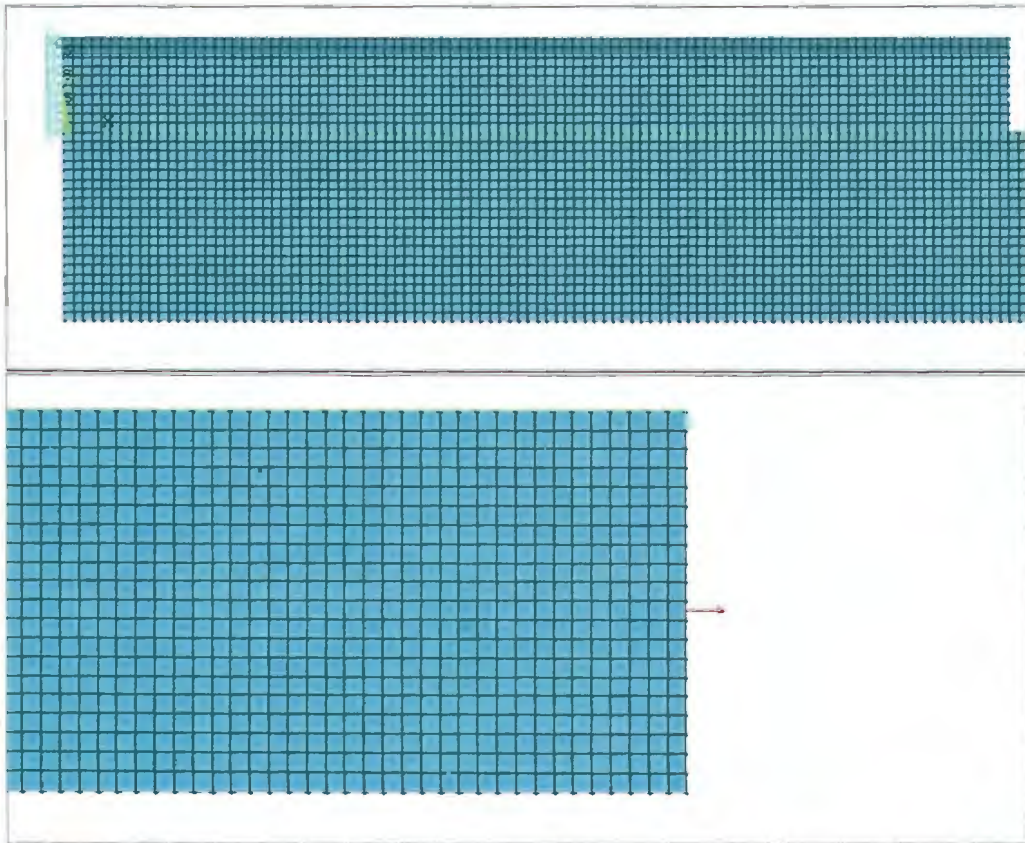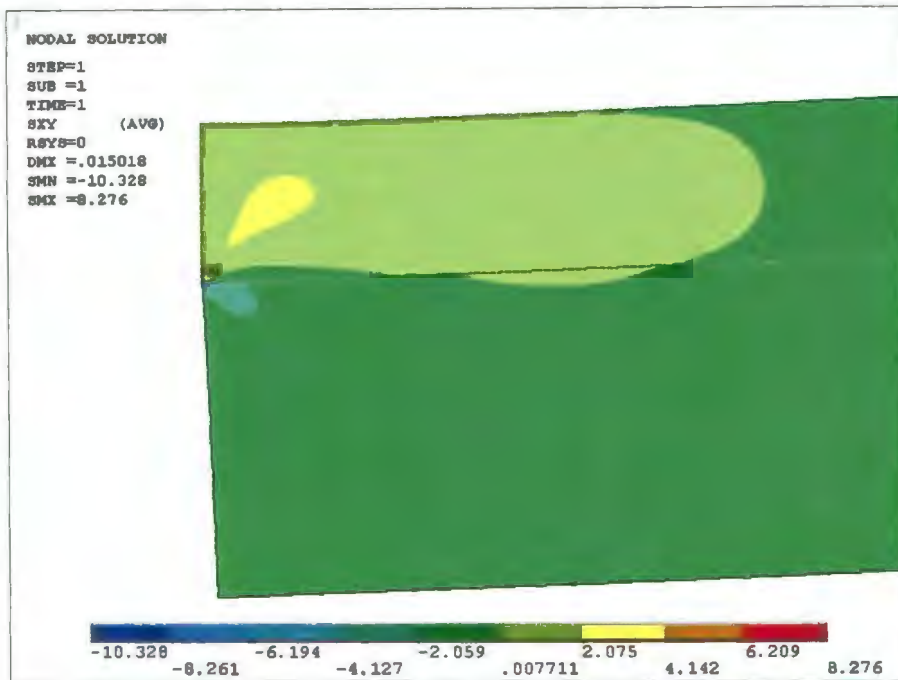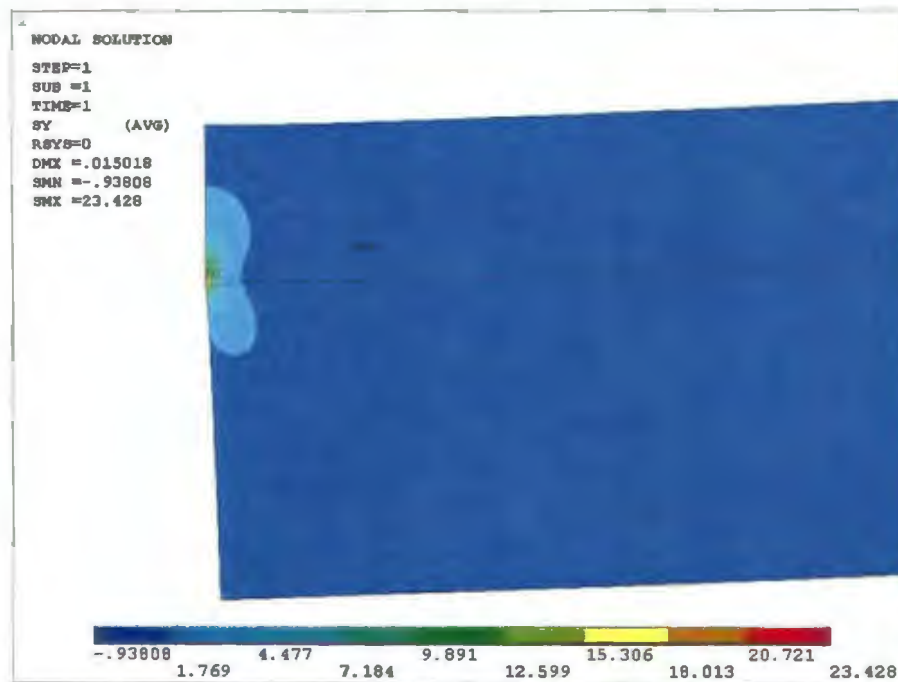

Figure 4.3. ANSYS™ element plots depicting the symmetry BCs at the joint mid-span (top) and the applied tensile load (bottom).

(a)

(b)

Figure 4.4. ANSYS™ contour stress plots depicting the shear (a) and normal (b) stresses in the single-sided strap joint.

Interfacial shear and normal stress distributions predicted by the present model, compared with the FEA results, are shown in Figure 4.5. It is clear from the figure that the highest interfacial stresses occur near the left edge of the reduced half-joint (that is, at the center of the full strap-joint model); this stress concentration can be attributed to the bending moment at the mid-span of the joint. Once again, as in Chapter 3, it should be noted that the interfacial stresses scale up rapidly with decreasing mesh size due to the stress singularity near the free edges. However, despite the failure of the current method to address this singularity (like most other analytic models in the literature), the otherwise very close agreement between the FEA results and those of the new semi-analytic model seem to validate the new stress-function variational method.

4.2.2 Interfacial Stresses in a Single-Sided Strap Joint Due to Thermal Loads

It was mentioned in Section 4.1.3 that for the single-sided strap joint subjected purely to uniform temperature change, the system was analogous to that of a bimaterial thermostat. In order to further validate the interfacial stress solutions of this model, the pure thermal loading scenario is subsequently compared to the bimaterial thermostat analysis of Suhir (1989a & 1989b), Eischen et al. (1990), and Ru (2002). The joint parameters remain identical to those given in the thermal analysis of the previous chapter (Section 3.2.3), and the joint is considered in *plane-strain*. Figure 4.6 shows the interfacial shear and normal stress distributions across the joint under the thermal load. Just as in the previous chapter, the interfacial stresses are concentrated near the free edges of the joint; the peak interfacial shear stress value ($\tau_{max} = 69.32 \, \text{MPa}$) is located at a distance approximately $L/20$ from the free edges, a result in close agreement with Ru's (2002)
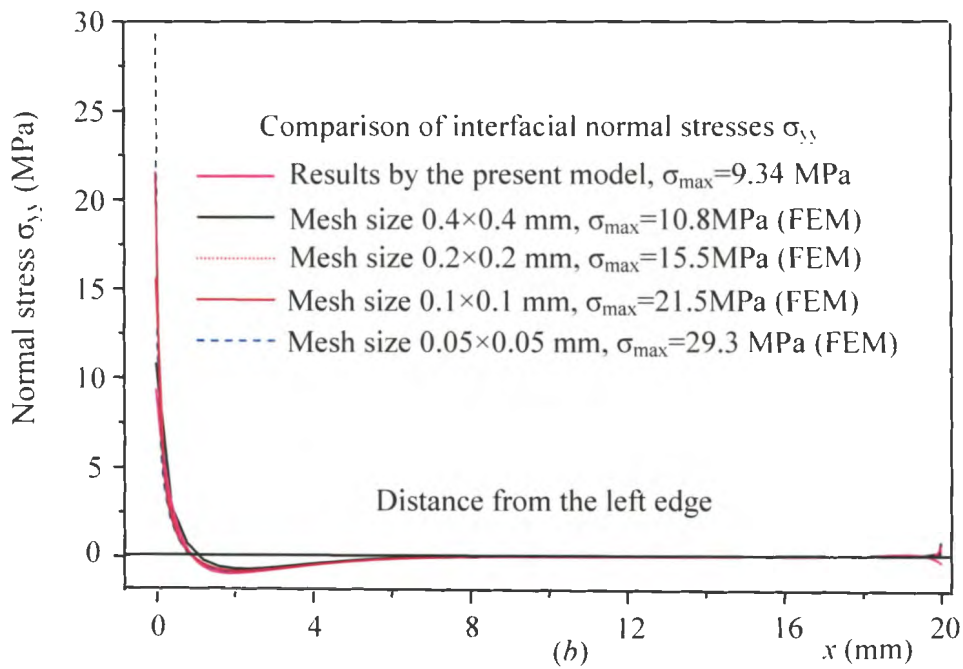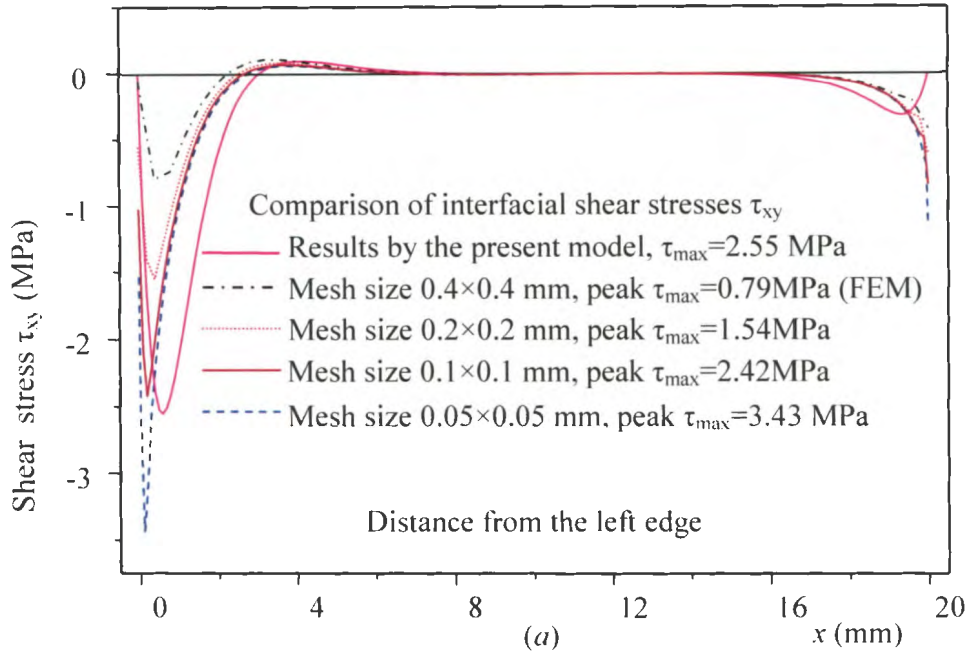
Figure 4.5. Comparison of the interfacial shear (*a*) and normal (*b*) stresses predicted by the current method with results obtained by FEM (ANSYS[TM]).
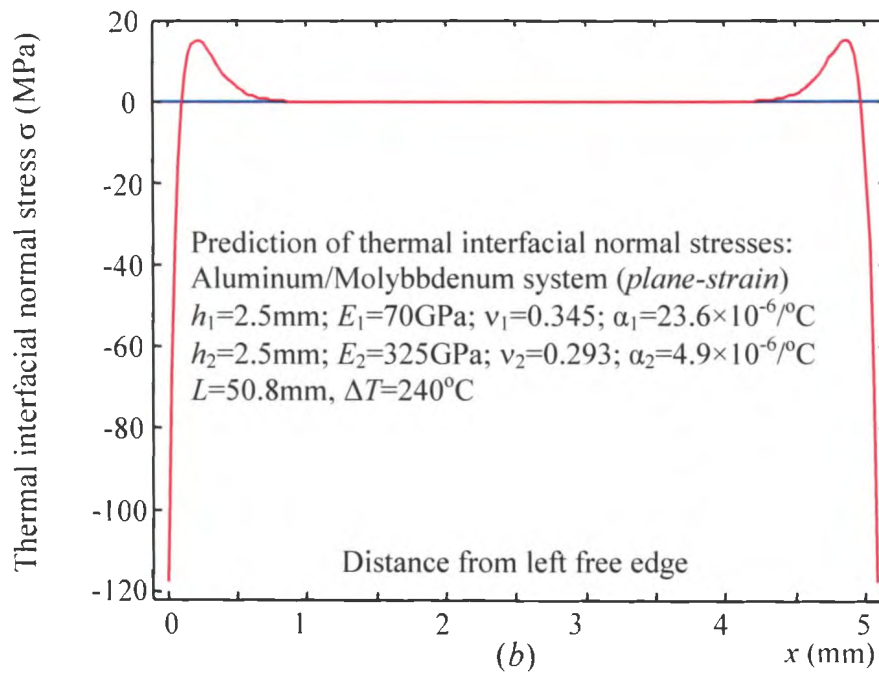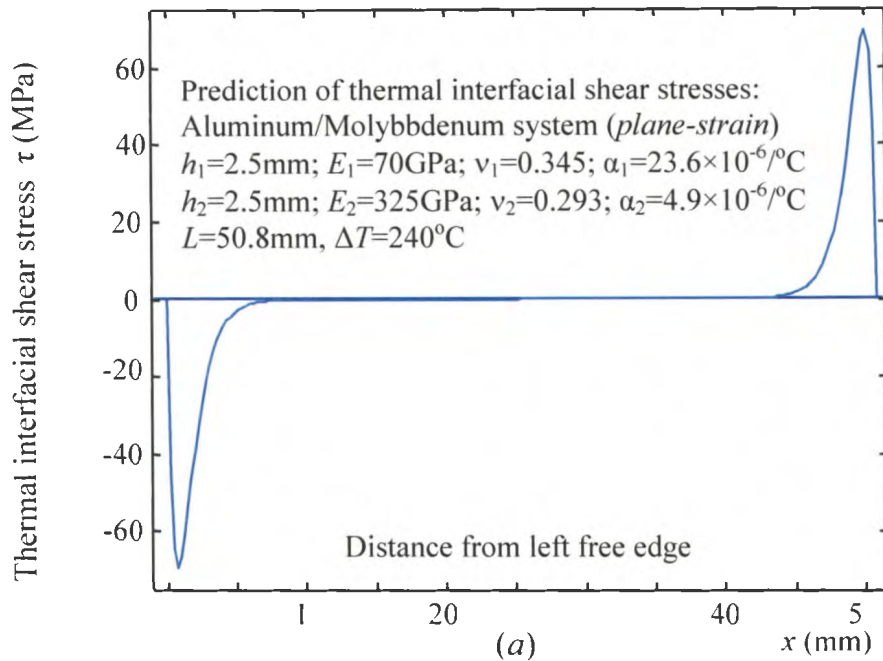
Figure 4.6. Thermomechanical interfacial shear (*a*) and normal (*b*) stresses in a bimaterial thermostat subjected to uniform temperature change $\Delta T = 240^\circ C$.

solution of $\tau_{max} = 70$ MPa. The maximum value of the interfacial normal stress, $\sigma_{max} = 117.70$ MPa, lies between the data found in the literature (specifically, this value is higher than the results by Ru (2002) and Eischen et al. (1990), yet lower than those found by Suhir (1989a & 1989b)). These findings indicate the reliability of the current model.

4.3 Scaling Analysis

4.3.1 Scaling Analysis of Interfacial Stresses Due to Mechanical Loads

One of the strengths of the present method is that all pertinent joint parameters and material properties (i.e., Young's moduli, Poisson's ratios, thicknesses of the adherend, etc.) are fully incorporated into the formulation; this sheds some insight onto how the interfacial stresses scale with various model parameters. To begin with, a set of four differing adherend thickness ratios ($h_1/h_2 = 0.2$, 0.5, 1, and 2), two length ratios ($L/h_2 = 5$ and 10), and two modulus ratios ($E_1/E_2 = 3$ and 10) are considered. Poisson's ratios are maintained at the constants $v_1 = 0.293$ and $v_2 = 0.34$, and the joint is considered in *plane-stress*. For the scaling analysis, the dimensionless interfacial shear and normal stresses, τ/p_0 and σ/p_0 respectively, are examined over the dimensionless distance from the joint mid-span, x/h_2. Figures 4.7 through 4.12 show the variation of the shear stress distribution with respect to changing length and thickness ratios. Note that the interfacial stresses satisfy the shear-free BC perfectly at the adherend ends. Also notice the high concentration of interfacial stresses near the interior edges of the joint; this, as previously mentioned, is caused by the bending moment induced at the joint mid-span. These high stress concentrations strongly indicate that debonding failure caused by high peeling (normal) stress at the joint mid-span is likely the main failure mode for single-sided strap joints.

61
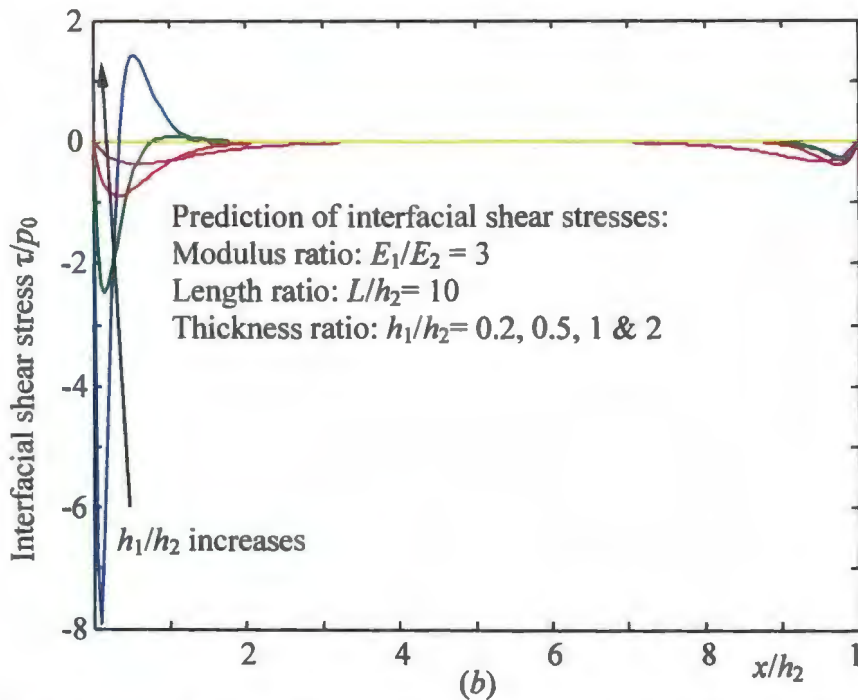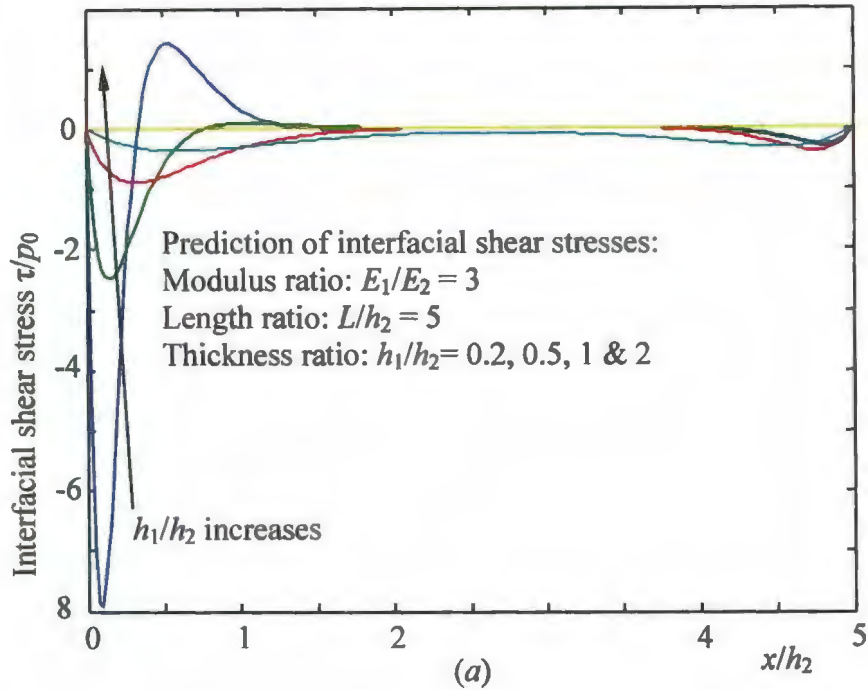
Figure 4.7. Variations of the dimensionless interfacial shear stresses in the single-sided strap joint over dimensionless distance from the mid-span: (a) the shear stress for length ratio $L/h_2 = 5$, (b) the shear stress for length ratio $L/h_2 = 10$. The modulus ratio for both cases is $E_1/E_2 = 3$.
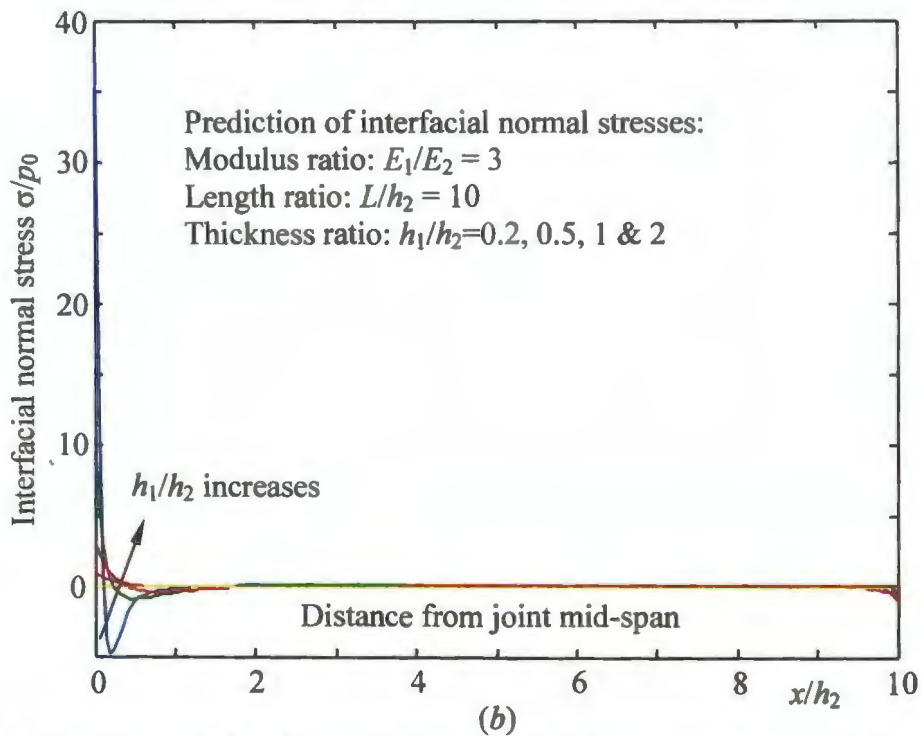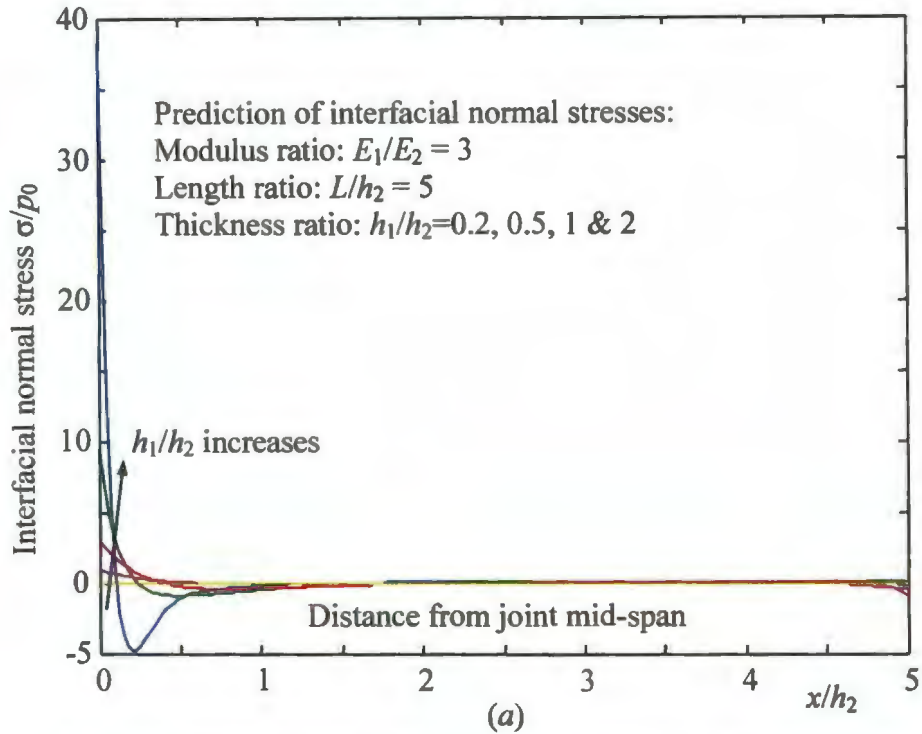
Figure 4.8. Variations of the dimensionless interfacial normal stresses in the single-sided strap joint over dimensionless distance from the mid-span: (a) the normal stress for length ratio $L/h_2 = 5$; (b) the normal stress for $L/h_2 = 10$. The modulus ratio for both cases is $E_1/E_2 = 3$.
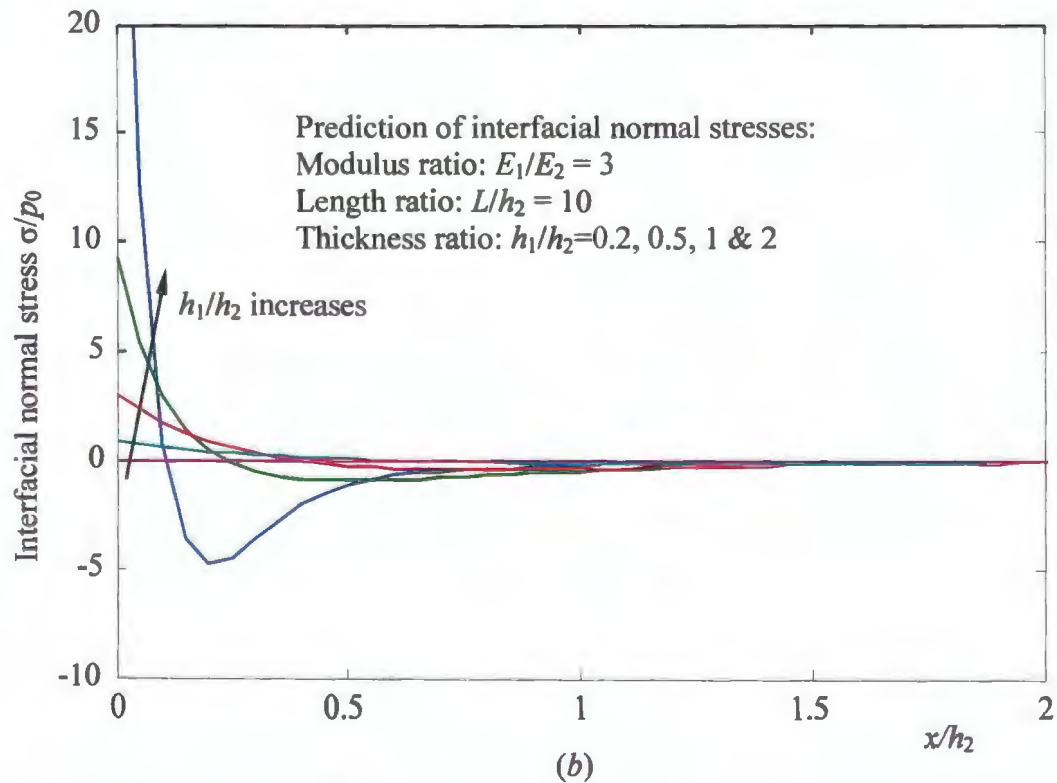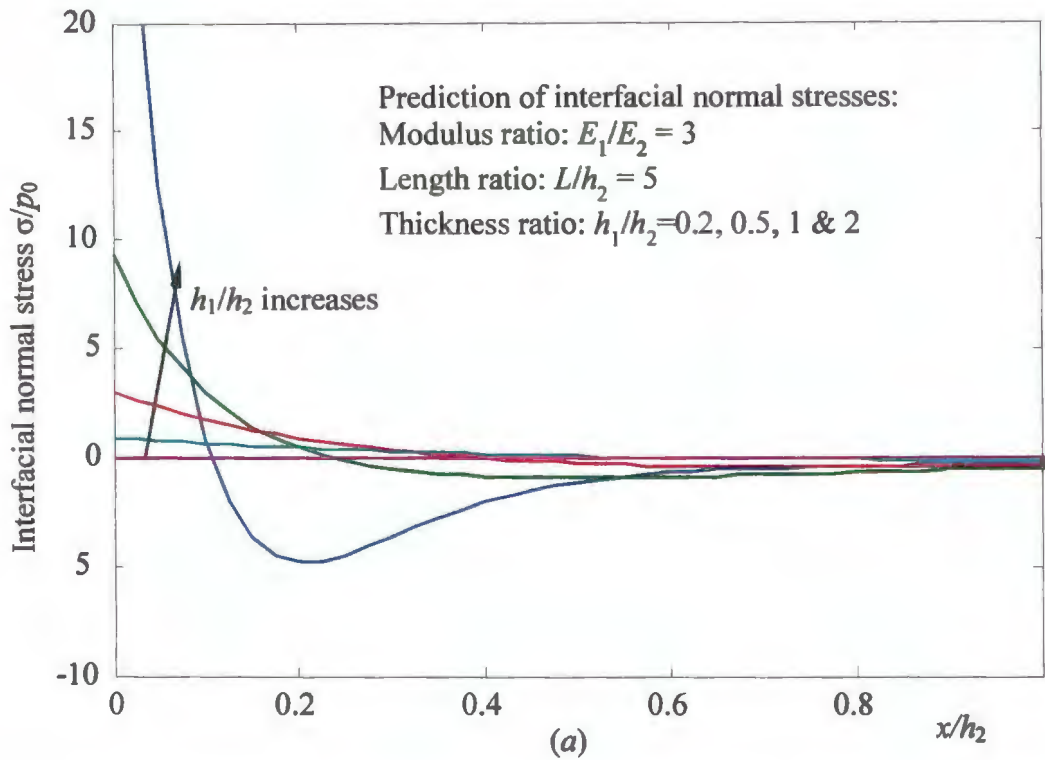
Figure 4.9. Comparison of the variation of interfacial normal stresses for (a) $L/h_2 = 5$ and (b) $L/h_2 = 10$ over a distance of 20% L/h_2 from the mid-span.
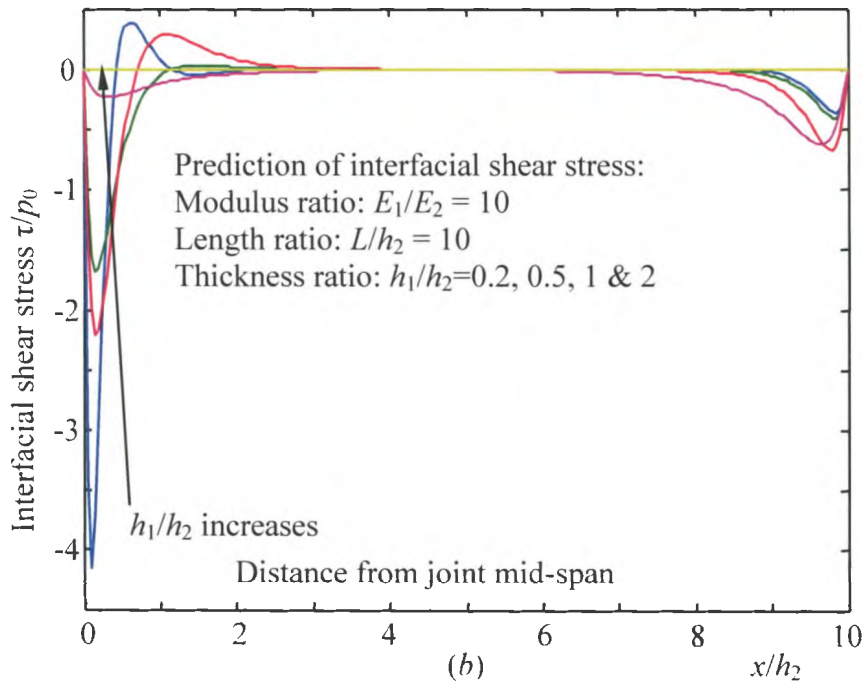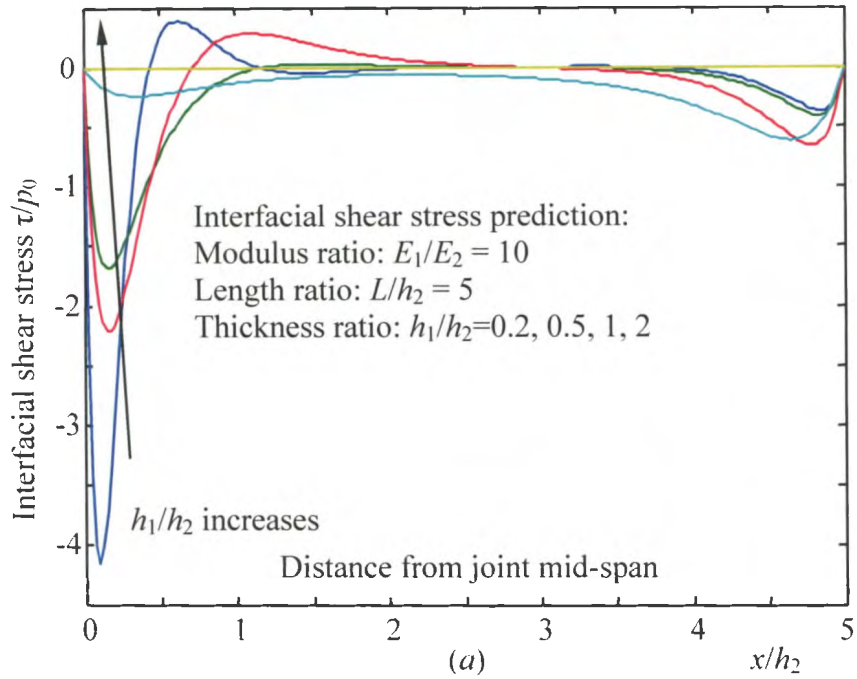
Figure 4.10. Variations of the dimensionless interfacial shear stress in the single-sided strap joint: (a) the stress distribution for length ratio $L/h_2 = 5$, and (b) the stress distribution for $L/h_2 = 10$. The modulus ratio for both cases is $E_1/E_2 = 10$.
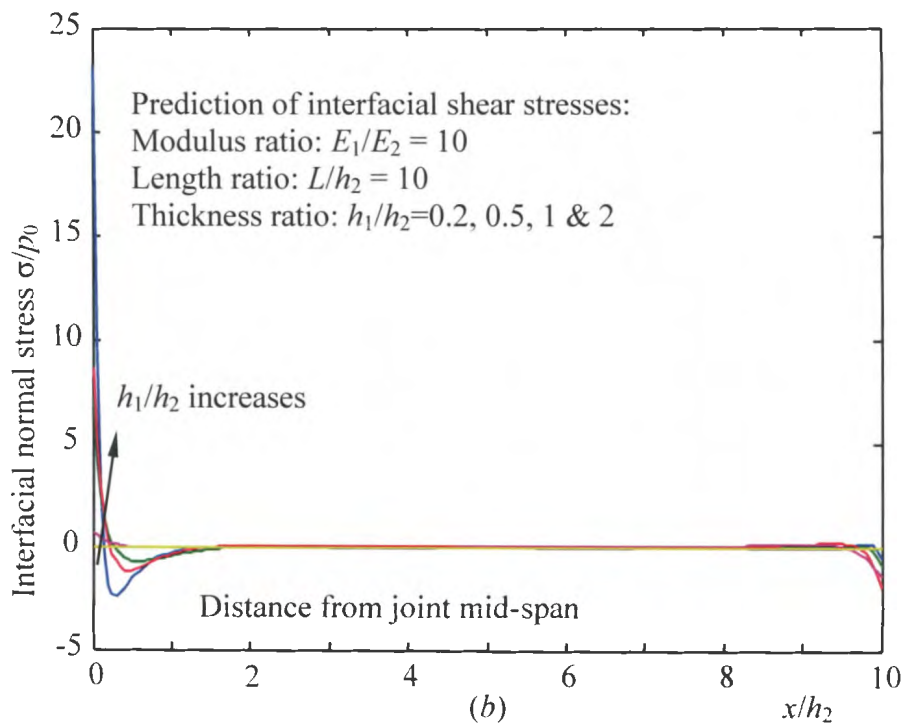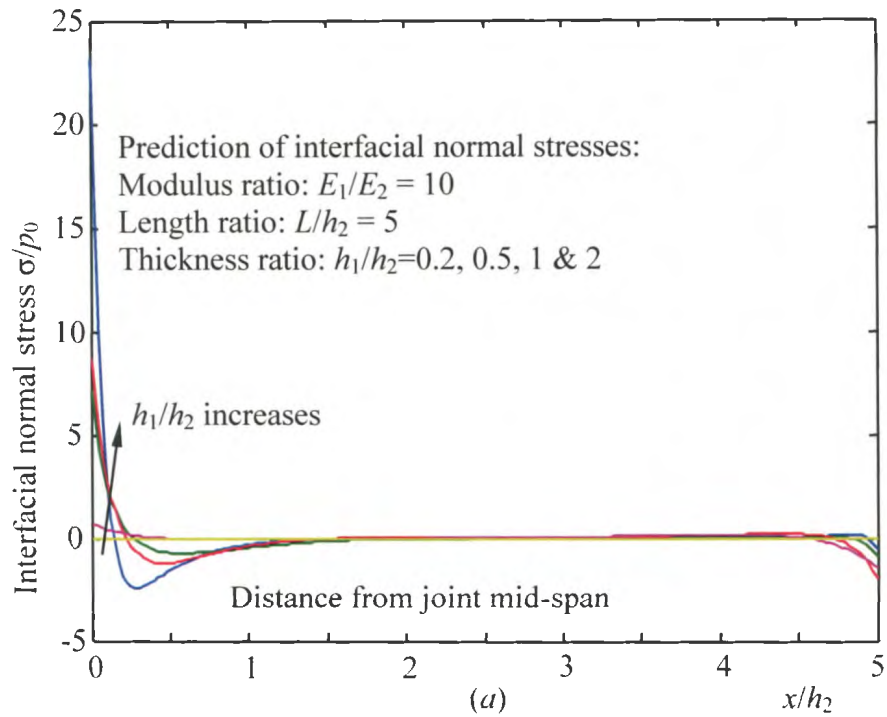
Figure 4.11. Variations of the dimensionless interfacial normal stress in the single-sided strap joint for length ratio $L/h_2 = 5$ (*a*), and $L/h_2 = 10$ (*b*). The modulus ratio is $E_1/E_2 = 10$.
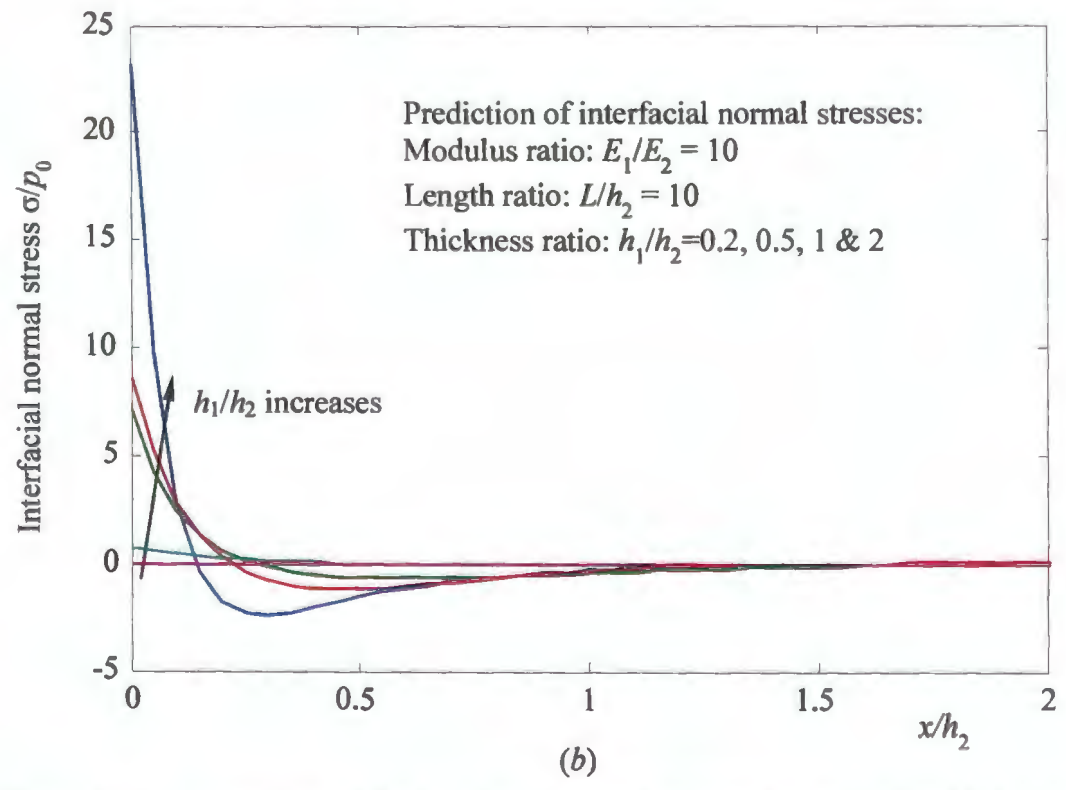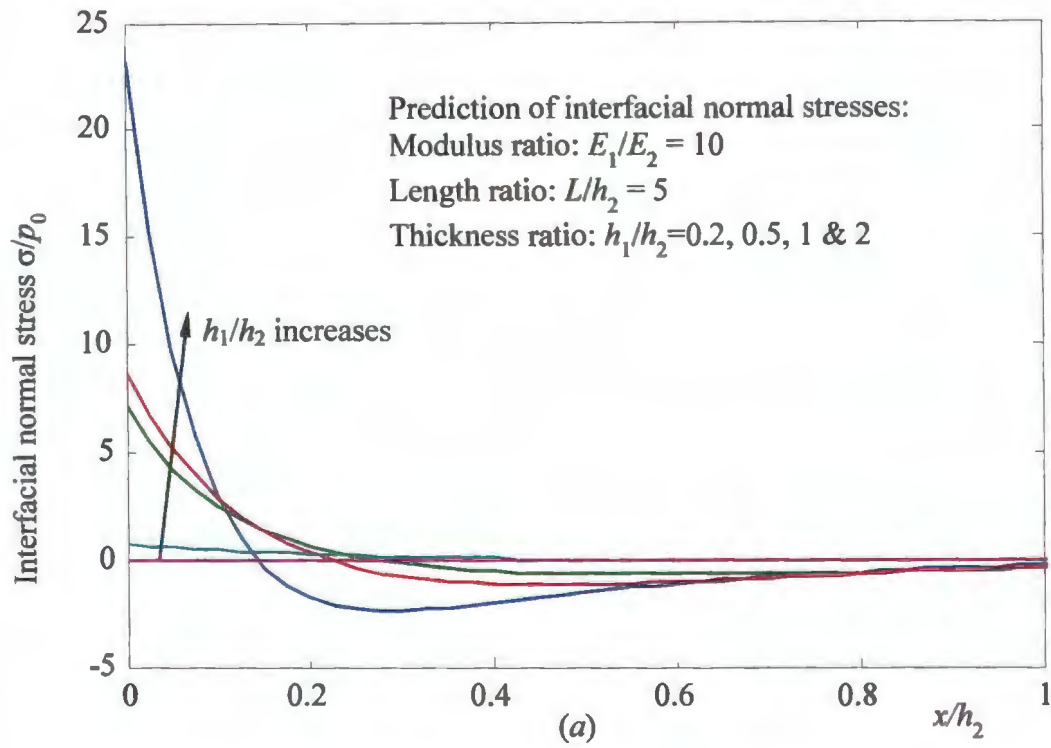
Figure 4.12. Comparison of the interfacial normal stresses in the single-sided strap joint for (*a*) $L/h_2 = 5$, and (*b*) $L/h_2 = 10$ over a distance of 20% L/h_2 from the mid-span for $E_1/E_2 = 10$.

Furthermore, it can be observed from Figures 4.7 through 4.12 that the length ratio L/h_2 does not have a pronounced effect on the interfacial stress distribution, while both the adherend thickness and modulus ratio appreciably alter the interfacial stresses. The data suggest that for a given length ratio, increasing either the modulus ratio or adherend thickness ratio will decrease the value of maximum interfacial stress in the joint. This phenomenon can be described as increasing the effective flexural rigidity of the cover layer (making it thicker or stiffer), which tends to suppress the large deflections at the joint mid-span that cause the high concentrations of interfacial stresses near the interior joint edges. As these mid-span stress concentrations have already been identified as the leading cause of debonding failure in the joint, it can be concluded that stiffer or thicker cover layers will increase the strength and durability of single-sided strap joints.

4.3.2 Scaling Analysis of Interfacial Stresses Due to Pure Temperature Change

As Section 4.2.2 explained, the stress analysis of the single-sided strap joint subjected to uniform temperature change is equivalent to that of a bimaterial thermostat; to that end, the joint parameters from Section 4.2.2 will continue to be used in the scaling analysis of the joint due to thermal loads. The joint is still considered in the *plane-strain* state for the thermal scaling analysis, and the dimensionless interfacial shear and normal stresses are now taken to be $\tau / \{E_2[(1+v_1)\alpha_1 - (1+v_2)\alpha_2]\Delta T\}$ and $\sigma / \{E_2[(1+v_1)\alpha_1 - (1+v_2)\alpha_2]\Delta T\}$. Similar to the previous section, stress variation over the dimensionless length coordinate x/h_2 with respect to variable thickness, length and modulus ratios is studied. Just as in the previous section, the thickness ratio appears to

have little effect on the stress distribution, while the thickness and modulus ratios have an appreciable impact on the magnitude of the interfacial stresses.

Figures 4.13 through 4.16 show the stress distributions for varying modulus and length ratios. There are several important differences between the scaling behavior of the interfacial stresses from the previous (mechanical) section and this bimaterial thermostat analysis which should be noted. The first is the scaling behavior of interfacial stresses with thickness ratio: all other parameters being held constant, decreasing the thickness ratio leads to lower values of interfacial shear stress, but increased values of interfacial normal stress. This can be explained as follows: the thicker cover layer results in a higher bending stiffness in the joint. This increased stiffness causes higher bending flexural stress which directly influences the interfacial normal stress. Furthermore, the increased bending stiffness also acts to suppress shearing strain at the joint interface (resulting in lower shear stress).

The second notable trend in the thermomechanical scaling behavior of the joint stresses concerns the modulus ratio. For a given thickness and length ratio, an increase in the modulus ratio of the joint results in a marked increase in the value of both interfacial shear and normal stresses. This is because the mismatch of thermal expansion properties of the adherends directly influences the mismatch of thermal strains when the joint is subjected to a uniform temperature change. These thermal strain mismatches, in turn, affect the bending of the joint, and therefore the interfacial stresses induced by that bending. In general, the greater the discrepancy between Young's moduli for the adherends of the joint, the greater the expected thermomechanical interfacial stresses.
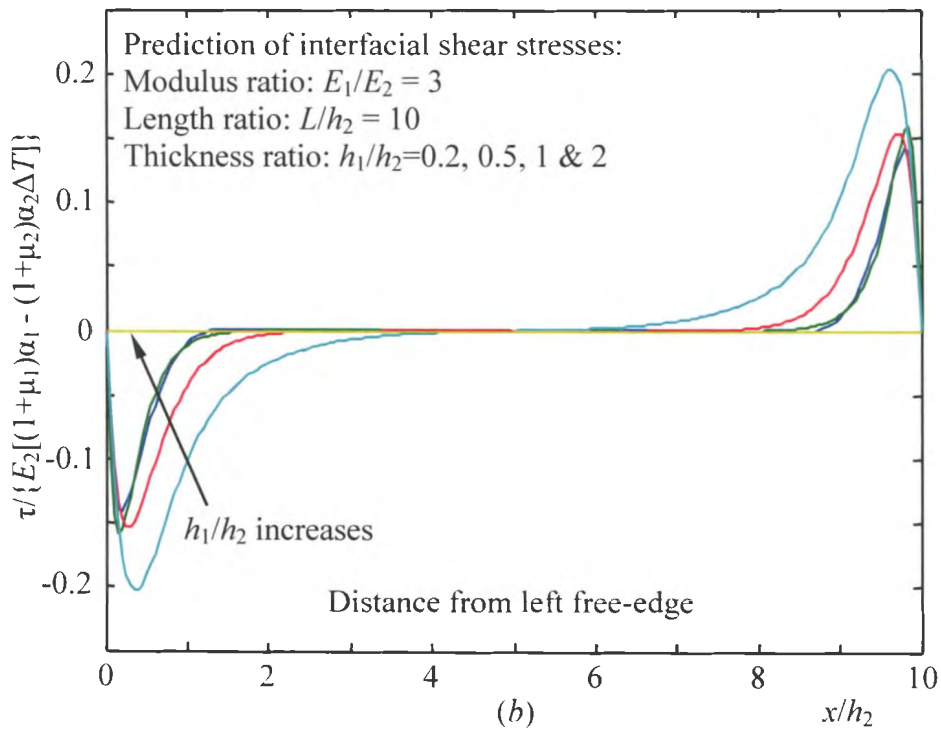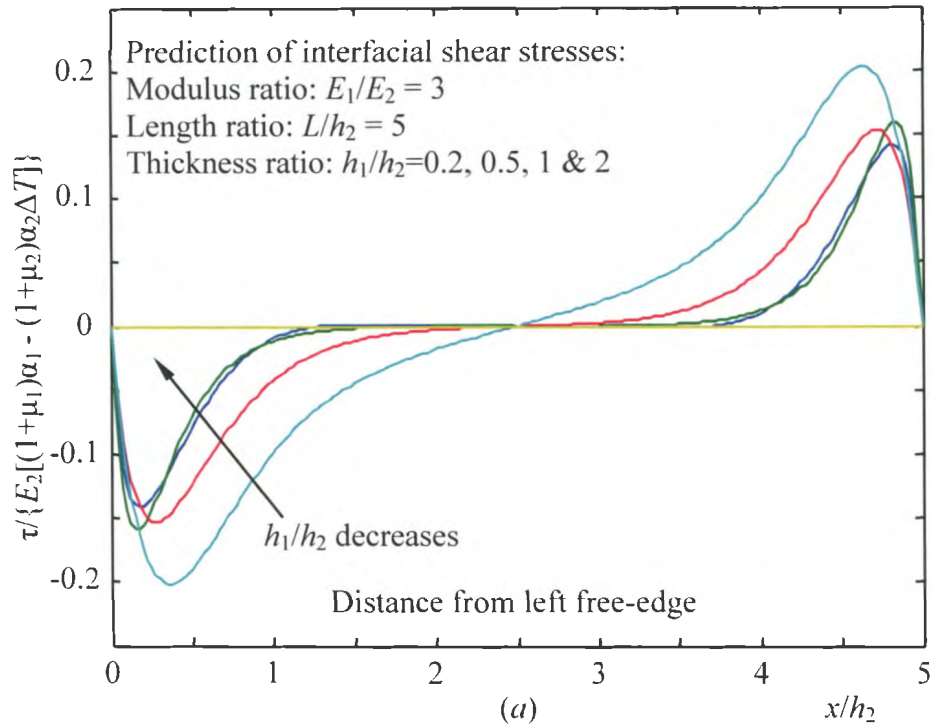
Figure 4.13. Variations of dimensionless thermomechanical interfacial shear stresses in a bimaterial thermostat subjected to uniform temperature change with respect to dimensionless distance from the left free-edge over varying thickness and length ratios ($E_1/E_2 = 3$).

70
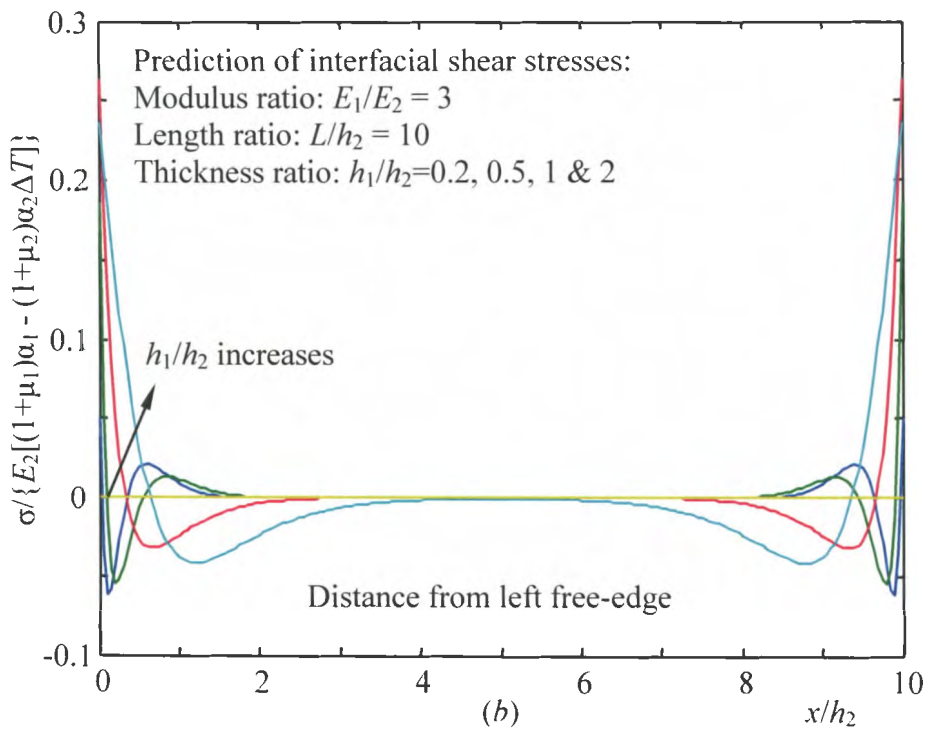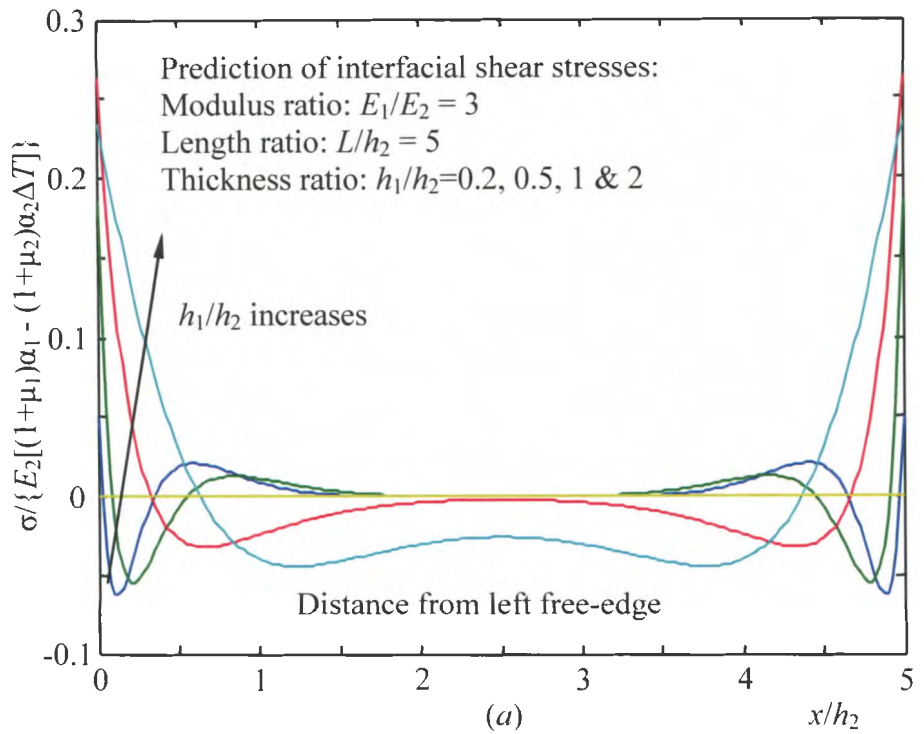
Figure 4.14. Variations of dimensionless thermomechanical interfacial normal stresses in a bimaterial thermostat subjected to uniform temperature change with respect to dimensionless distance from the left free-edge over varying thickness and length ratios ($E_1/E_2 = 3$).

71
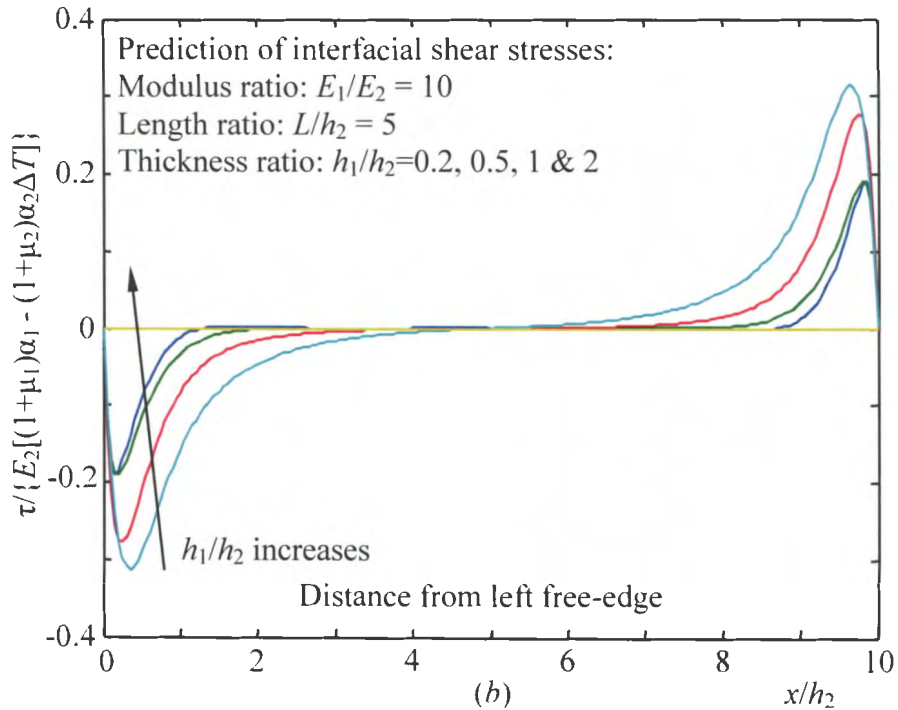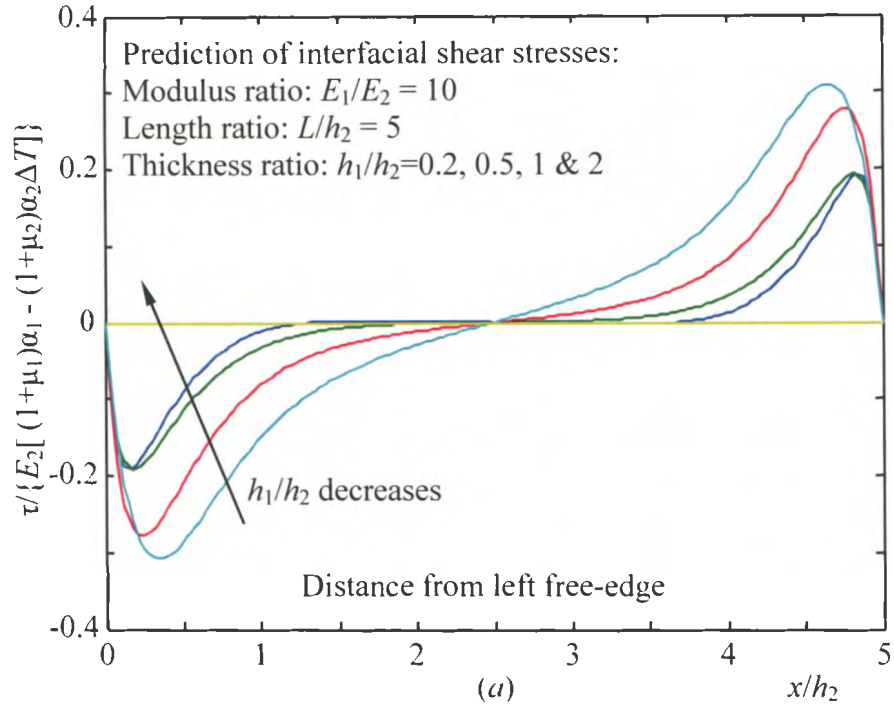
Figure 4.15. Variations of the dimensionless thermomechanical interfacial shear stresses in the bimaterial thermostat for varying thickness and length ratios ($E_1/E_2 = 10$).
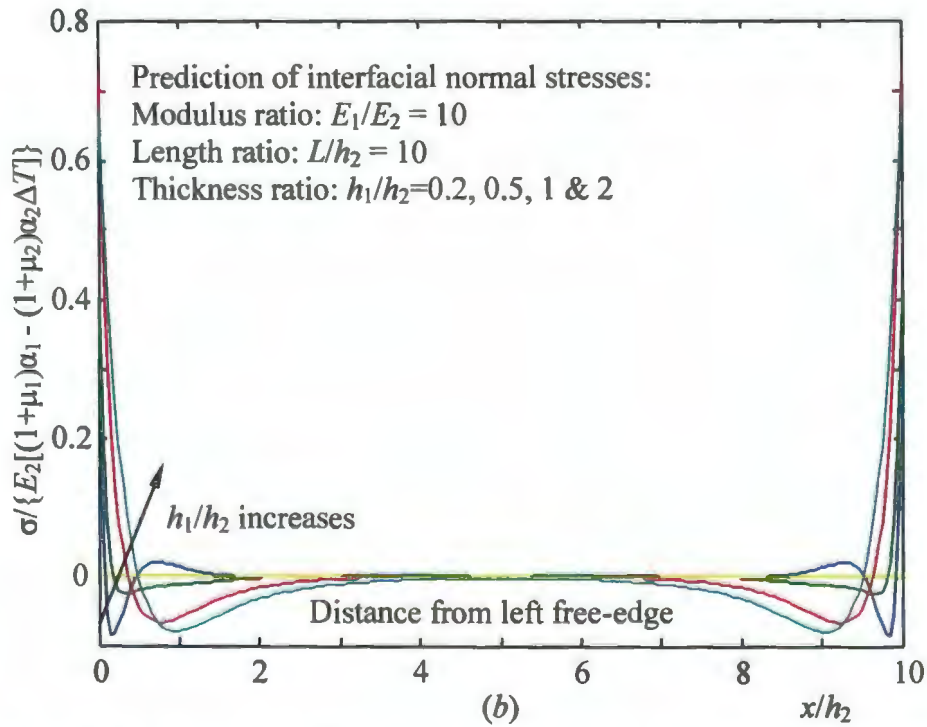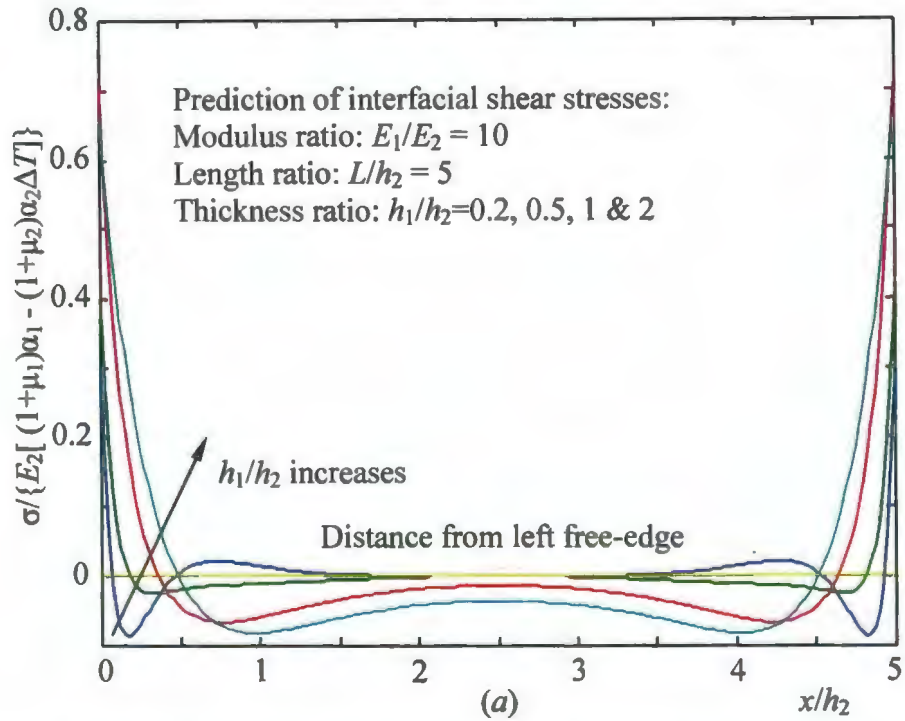
Figure 4.16. Variations of the dimensionless thermomechanical interfacial normal stresses in the bimaterial thermostat for varying thickness and length ratios ($E_1/E_2 = 10$).

Lastly, the figures show that for all the given cases of thickness and modulus ratios, the maximum value of the interfacial normal stress is greater than that of the interfacial shear stress. This characteristic phenomenon indicates that debonding failure caused by high peeling (normal) stress is the primary mode of failure for bimaterial thermostats.

As the previous sections have demonstrated, the current stress-function variational method provides a robust and accurate model for the interfacial stresses of the single-sided bonded joint. However, it should be noted again that one of the strengths of the current model is its generality and applicability to other bonded joint configurations as well. The following section outlines how the method is applied to determine the stress solutions for a single-lap joint subjected to mechanical and thermal loads.

4.4 Application of the Stress-Function Variational Method to Single-Lap Joints

4.4.1 Model Formulation

Consider a bonded single-lap joint (SLJ) shown in Figure 4.17 consisting of two isotropic, linearly thermoelastic adherends. Consistent with the previous derivation, the thicknesses, Young's moduli and Poisson's ratios for each of the adherends are h_i, E_i, and v_i ($i = 1, 2$) where the subscripts 1 and 2 refer to the upper and lower adherend, respectively.

As the figure shows, the overlap region of the joint has length L, and both adherends are assumed to have identical thickness b (assumed unit thickness). The x-coordinate is defined from the left edge of the lower adherend along the beam axis; the y-coordinates are directed vertically from the centroid of the cross-section of each adherend

respectively. In general, the joint is subjected to a combination of traction BCs of tensile force P_0, transverse shear force V_0, and bending moments M_1 and M_2 as shown in Figure 4.17, in addition to the uniform temperature change ΔT.
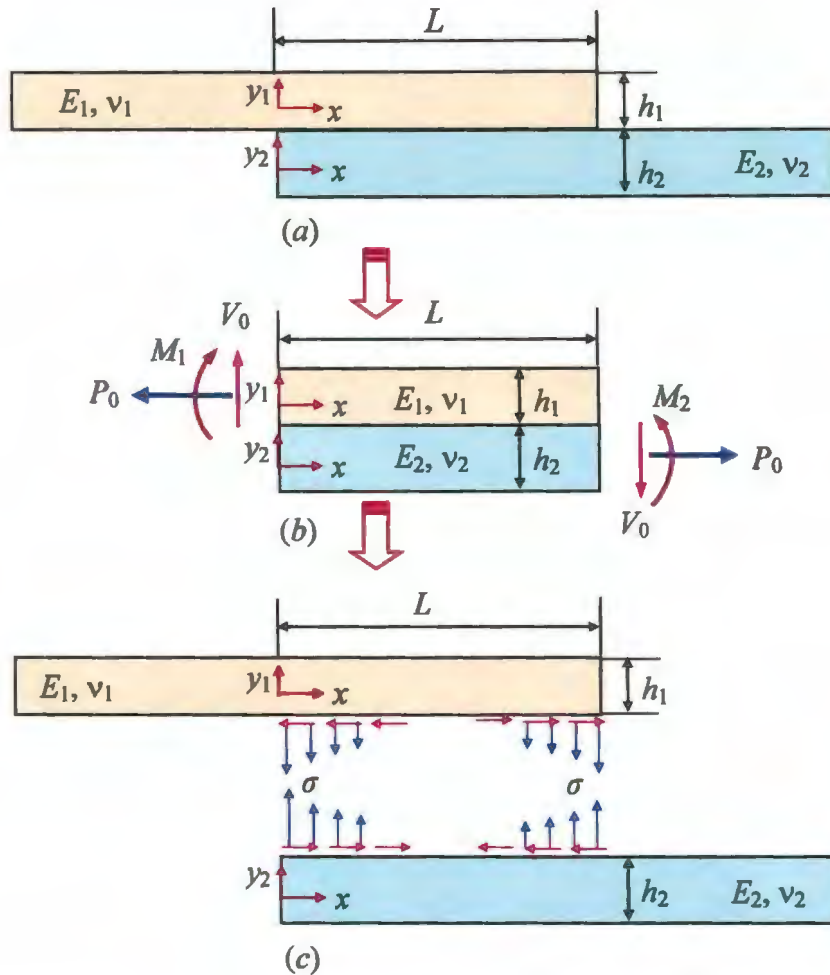
Figure 4.17. Schematic of the single-lap joint consisting of two slender adherends (a); FBD of the joint overlap region with effective traction BCs (b); and depiction of the interfacial shear and normal stresses (c).

4.4.2 Planar Stresses in the Single-Lap Joint

Due to the universality of the present method, much of the problem derivation can be exactly repeated from the previous work. To begin with, representative segmental elements of the upper and lower adherends can be described exactly as in Figure 4.2; the corresponding static equilibrium equations may be directly used from (4.1) through (4.6). With the two unknown interfacial stress functions defined as in (4.7), the first modification of the SLJ-specific model is in the traction BCs, which are now:

$$S_1(0) = p_0 b h_2 \tag{4.86}$$

$$S_1(L) = 0 \tag{4.87}$$

$$Q_1(0) = t_0 b h_2 \tag{4.88}$$

$$Q_1(L) = 0 \tag{4.89}$$

$$M_1(0) = M_1 b \tag{4.90}$$

$$M_1(L) = 0 \tag{4.91}$$

$$S_2(0) = 0 \tag{4.92}$$

$$S_2(L) = p_0 b h_2 \tag{4.93}$$

$$Q_2(0) = 0 \tag{4.94}$$

$$Q_2(L) = t_0 b h_2 \tag{4.95}$$

$$M_2(0) = 0 \tag{4.96}$$

$$M_2(L) = -M_2 b \tag{4.97}$$

where p_0, t_0, M_1, and M_2 are the average normal stress, shear stress, and bending moments per unit width in the joint [Compare (4.88), (4.90), (4.95) and (4.97) to (4.11), (4.13),

(4.18) and (4.20) for the BC modifications]. Now by following the exact procedure outlined in Section 4.1.3, the stress resultants of the SLJ are determined as:

$$S_1(x) = p_0 b h_2 - \int_0^x b f(\xi) \, d\xi \tag{4.98}$$

$$Q_1(x) = t_0 b h_2 - b \int_0^x g(\xi) \, d\xi \tag{4.99}$$

$$M_1(x) = M_1 b + t_0 h_2 b x - b \int_0^x \int_0^\xi g(\varsigma) \, d\varsigma \, d\xi - \frac{b h_1}{2} \int_0^x f(\xi) \, d\xi \tag{4.100}$$

$$S_2(x) = b \int_0^x f(\xi) \, d\xi \tag{4.101}$$

$$Q_2(x) = b \int_0^x g(\xi) \, d\xi \tag{4.102}$$

$$M_2(x) = b \int_0^x \int_0^\xi g(\varsigma) \, d\varsigma \, d\xi - \frac{b h_2}{2} \int_0^x f(\xi) \, d\xi \tag{4.103}$$

Here, note that the expressions of Q_1 and M_1 have altered from the previous formulation [Eqs. (4.24) and (4.26), respectively].

According to the method of Section 4.1.4, using the *Euler-Bernoulli* flexural stress formula and integration of the static equilibrium equations, the stress components for the SLJ can be determined as:

$$\sigma_{xx}^{(1)} = p_1 - \frac{1}{h_1} \int_0^x f(\xi) \, d\xi - \frac{12 y_1}{h_1^3} \left[M_1 + t_0 h_2 x - \int_0^x \int_0^\xi g(\varsigma) \, d\varsigma \, d\xi - \frac{h_1}{2} \int_0^x f(\xi) \, d\xi \right] \tag{4.104}$$

$$\tau_{y_1 x}^{(1)} = -\frac{1}{h_1} \left[\left(\frac{h_1}{2} - y_1 \right) - \frac{3}{h_1} \left(\frac{h_1^2}{4} - y_1^2 \right) \right] f(x) + \frac{6}{h_1^3} \left(\frac{h_1^2}{4} - y_1^2 \right) \left[\int_0^x g(\xi) \, d\xi - t_0 h_2 \right] \tag{4.105}$$

$$\sigma_{y_1 y_1}^{(1)} = -\frac{1}{h_1} \left\{ \frac{h_1}{2} \left(\frac{h_1}{2} - y_1 \right) - \frac{1}{2} \left(\frac{h_1^2}{4} - y_1^2 \right) - \frac{3}{h_1} \left[\frac{h_1^2}{4} \left(\frac{h_1}{2} - y_1 \right) - \frac{1}{3} \left(\frac{h_1^3}{8} - y_1^3 \right) \right] \right\} f'(x)$$
$$+ \frac{6}{h_1^3} \left[\frac{h_1^2}{4} \left(\frac{h_1}{2} - y_1 \right) - \frac{1}{3} \left(\frac{h_1^3}{8} - y_1^3 \right) \right] g(x) \tag{4.106}$$

$$\sigma_{xx}^{(2)} = \frac{1}{h_2} \int_0^x f(\xi)\,d\xi - \frac{12 y_2}{h_2^3} \left[\int_0^x \int_0^\xi g(\varsigma)\,d\varsigma\,d\xi - \frac{h_2}{2} \int_0^x f(\xi)\,d\xi \right] \tag{4.107}$$

$$\tau_{y_2 x}^{(2)} = -\frac{1}{h_2}\left[\left(y_2 + \frac{h_2}{2}\right) + \frac{3}{h_2}\left(y_2^2 - \frac{h_2^2}{4}\right)\right] f(x) + \frac{6}{h_2^3}\left(y_2^2 - \frac{h_2^2}{4}\right)\int_0^x g(\xi)\,d\xi \tag{4.108}$$

$$\sigma_{y_2 y_2}^{(2)} = \left\{\frac{1}{h_2}\left[\frac{1}{2}\left(y_2^2 - \frac{h_2^2}{4}\right) + \frac{h_2}{2}\left(y_2 + \frac{h_2}{2}\right)\right] + \frac{3}{h_2^2}\left[\frac{1}{3}\left(y_2^3 + \frac{h_2^3}{8}\right) - \frac{h_2^2}{4}\left(y_2 + \frac{h_2}{2}\right)\right]\right\} f'(x)$$
$$-\frac{6}{h_2^3}\left[\frac{1}{3}\left(y_2^3 + \frac{h_2^3}{8}\right) - \frac{h_2^2}{4}\left(y_2 + \frac{h_2}{2}\right)\right] g(x) \tag{4.109}$$

Note that in the above, the expression for the axial normal stress in the upper adherend has taken into account the axial normal force, transverse shear force, and bending moment contributions; also note that due to the left-end BCs for the lower adherend remaining trivial, the stress expressions in (4.107) to (4.109) are the same as those in (4.37), (4.39), and (4.41).

4.4.3 Governing Equations of Interfacial Stresses in the Single-Lap Joint

The strain energy of the SLJ is written according to (4.42) and (4.43), with the same variational constraint $\delta U = 0$ according to the theorem of minimum complementary strain energy. The variational operations on the single-lap joint result in Eqs. (4.45) through (4.49) remaining exactly intact; however the constants D_1 and D_2 are now defined as:

$$
D_1 = \begin{cases}
h_{12}^{-1} + 6h_{12}^{-2}\left(\dfrac{M_1}{p_0 h_2^2} + \dfrac{t_0}{p_0}\xi\right) + \dfrac{1}{2}(\alpha_1 - \alpha_2)\Delta TE_1 / p_0, \\[4pt]
\quad \text{(for thermomechanical loads--}plane - stress \text{ state)} \\[6pt]
h_{12}^{-1} + 6h_{12}^{-2}\left(\dfrac{M_1}{p_0 h_2^2} + \dfrac{t_0}{p_0}\xi\right) + \dfrac{1}{2}[\alpha_1(1+\upsilon_1) - \alpha_2(1+\upsilon_2)]\Delta TE_1 / p_0, \\[4pt]
\quad \text{(for thermomechanical loads--}plane - strain \text{ state)} \\[6pt]
h_{12}^{-1} + 6h_{12}^{-2}\left(\dfrac{M_1}{p_0 h_2^2} + \dfrac{t_0}{p_0}\xi\right), \\[4pt]
\quad \text{(for pure mechanical load--either }plane - stress \text{ or }plane - strain \text{ state)} \\[6pt]
\dfrac{1}{2}(\alpha_1 - \alpha_2)\Delta TE_1 / p_0, \quad \text{(for pure thermal loads--}plane - stress \text{ state)} \\[6pt]
\dfrac{1}{2}[\alpha_1(1+\upsilon_1) - \alpha_2(1+\upsilon_2)]\Delta TE_1 / p_0, \\[4pt]
\quad \text{(for pure thermal loads--}plane - strain \text{ state)}
\end{cases}
\tag{4.110}
$$

$$
D_2 = \begin{cases}
-12h_{12}^{-3}\left(\dfrac{M_1}{p_0 h_2^2} + \dfrac{t_0}{p_0}\xi\right), & \text{(pure mechanical or thermomechanical loads)} \\[6pt]
0, & \text{(pure thermal loads)}
\end{cases}
\tag{4.111}
$$

This demonstrates the universality of the governing ODEs for the stress analysis of any bonded joint made of two adherends. Two notes must be made concerning the derivation above, however; for the SLJ subjected to loads excluding axial tension (any combination of bending and shearing), the term h_{12}^{-1} in the first three cases of D_1 should be discarded, and p_0 should be taken as a reference stress for dimensionless analysis.

The governing ODEs of the system are the same as (4.64) except for

$$
\frac{d}{d\xi}\{\Phi_0\} = -[C]^{-1}\frac{d}{d\xi}\{D\} = -6h_{12}^{-2}[C]^{-1}\begin{Bmatrix} 1 \\ -2h_{12}^{-1} \end{Bmatrix}(t_0 / p_0)
\tag{4.112}
$$

Note that in the above, the particular solution $\{\Phi_0\}$ is a linear function of ξ; this is due to the fact that [C] is a nonsingular matrix of constant coefficients, while [D] carries a linear dependence on ξ. The general solution becomes:

$$\{\Phi\} = \sum_{k=1}^{4} [c_k \{\Psi_0^k\} \exp(\lambda_k \xi) + d_k \{\Psi_0^k\} \exp(-\lambda_k \xi)] + \{\Phi_0(\xi)\} \tag{4.113}$$

with the constants c_k and d_k determined by the application of eight linearly independent BC equations. Most of the BCs from (4.68) to (4.75) remain intact; however, (4.73) is modified to now become

$$G(L/h_2) = \frac{M_1}{p_0 h_2^2} + \frac{t_0}{p_0}\frac{L}{h_2} - \frac{h_{12}}{2} \tag{4.114}$$

while (4.75), which before was trivial, now contains a shear-force contribution:

$$G'(L/h_2) = \frac{t_0}{p_0} \tag{4.115}$$

Substitution of the general solution (4.113) along with (4.112) into the traction BCs leads to the system of linear algebraic equations:

$$\sum_{k=1}^{4} c_k \Psi_0^{k,1} + \sum_{k=1}^{4} d_k \Psi_0^{k,1} = -\Phi_0^{(1)}(0) \tag{4.116}$$

$$\sum_{k=1}^{4} c_k \Psi_0^{k,1} \exp(\lambda_k L/h_2) + \sum_{k=1}^{4} d_k \Psi_0^{k,1} \exp(-\lambda_k L/h_2) = -[1 + \Phi_0^{(1)}(L/h_2)] \tag{4.117}$$

$$\sum_{k=1}^{4} c_k \lambda_k \Psi_0^{k,1} - \sum_{k=1}^{4} d_k \lambda_k \Psi_0^{k,1} = -\frac{d\Phi_0^{(1)}}{d\xi} \tag{4.118}$$

$$\sum_{k=1}^{4} c_k \lambda_k \Psi_0^{k,1} \exp(\lambda_k L/h_2) - \sum_{k=1}^{4} d_k \lambda_k \Psi_0^{k,1} \exp(-\lambda_k L/h_2) = -\frac{d\Phi_0^{(1)}}{d\xi} \tag{4.119}$$

$$\sum_{k=1}^{4} c_k \Psi_0^{k,2} + \sum_{k=1}^{4} d_k \Psi_0^{k,2} = -\Phi_0^{(2)}(0) \tag{4.120}$$

$$\sum_{k=1}^{4} c_k \Psi_0^{k,2} \exp(\lambda_k L / h_2) + \sum_{k=1}^{4} d_k \Psi_0^{k,2} \exp(-\lambda_k L / h_2) = \frac{M_1}{p_0 h_2^2} + \frac{t_0}{p_0} \frac{L}{h_2} - \frac{h_{12}}{2} - \Phi_0^{(2)}(L / h_2) \qquad (4.121)$$

$$\sum_{k=1}^{4} c_k \lambda_k \Psi_0^{k,2} - \sum_{k=1}^{4} d_k \lambda_k \Psi_0^{k,2} = -\frac{d\Phi_0^{(2)}}{d\xi} \qquad (4.122)$$

$$\sum_{k=1}^{4} c_k \lambda_k \Psi_0^{k,2} \exp(\lambda_k L / h_2) - \sum_{k=1}^{4} d_k \lambda_k \Psi_0^{k,2} \exp(-\lambda_k L / h_2) = \frac{t_0}{p_0} - \frac{d\Phi_0^{(2)}}{d\xi} \qquad (4.123)$$

In the above, $\Psi_0^{k,1}$ and $\Psi_0^{k,2}$ ($k = 1, 2, 3, 4$) are the first and second elements of the k-th eigenvector; also note that $\Phi_0^{(1)}$ and $\Phi_0^{(2)}$ are the first and second elements of the particular solution vector $\{\Phi_0\}$ as mentioned in Section 4.1.5. For the SLJ subjected to a pure temperature change, all the traction BCs should become trivial; this will, in turn, affect the linear algebraic equations (4.116) to (4.123) accordingly. With all the coefficients c_k and d_k fully determined by the BCs, the explicit solutions for the interfacial shear and normal stresses are:

$$f(x) / p_0 = \sum_{k=1}^{4} c_k \Psi_0^{k,1} \lambda_k \exp(\lambda_k x / h_2) - \sum_{k=1}^{4} d_k \Psi_0^{k,1} \lambda_k \exp(-\lambda_k x / h_2) + \frac{d\Phi_0^{(1)}}{d\xi} \qquad (4.124)$$

$$g(x) / p_0 = \sum_{k=1}^{4} c_k \Psi_0^{k,2} \lambda_k^2 \exp(\lambda_k x / h_2) + \sum_{k=1}^{4} d_k \Psi_0^{k,2} \lambda_k^2 \exp(-\lambda_k x / h_2) \qquad (4.125)$$

4.4.4 Validation of the Single-Lap Joint Model

The current analysis of the single-lap joint has been based on a generalized version of the model created for a single-sided strap joint. In the limiting case that the transverse shear force t_0 is discarded from the SLJ formulation (i.e., a cantilevered single-lap joint subjected to axial tension), all the formulas and relations derived above reduce to those of the single-sided strap joint considered already. The static equivalency of these two systems

81

is shown in Figure 4.18. Also consider that, just as with the previous model, the case of pure temperature change reduces any two-adherend bonded joint model to that of the simple bimaterial thermostat. Furthermore, the stress distribution solutions obtained from the single-sided strap joint model have been carefully validated in Section 4.2. Therefore, the validity of the present (SLJ) model has already been demonstrated for the case of applied uniform axial tension and pure temperature change.
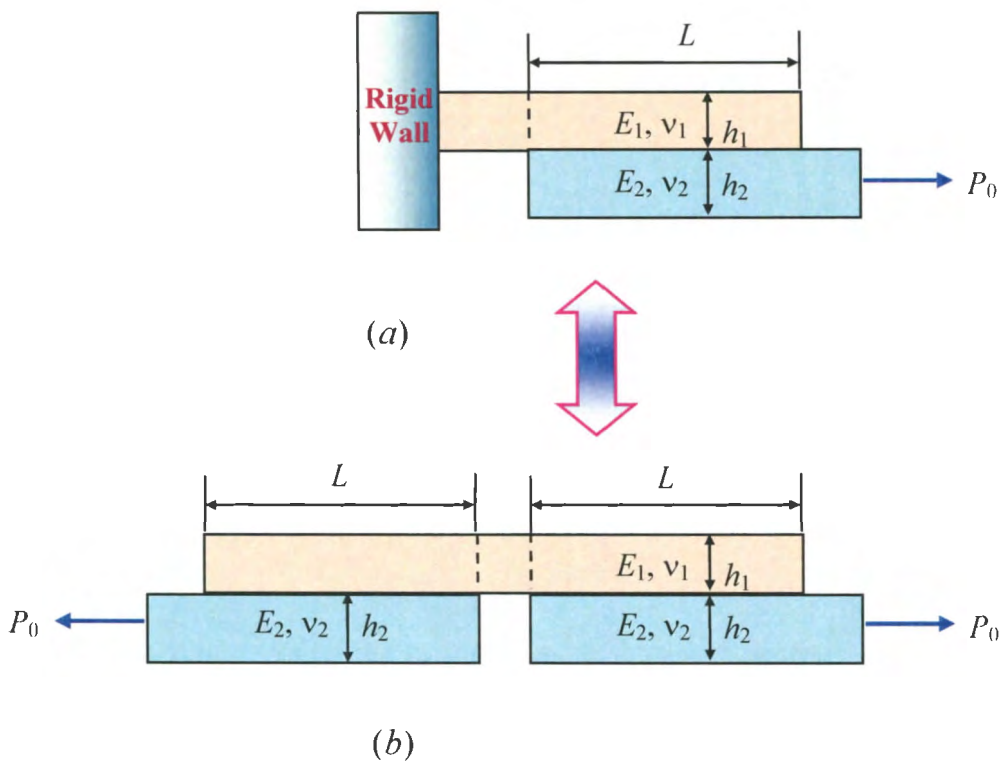
Figure 4.18. Static equivalency between (*a*) a cantilevered single-lap joint and (*b*) a single-sided strap joint subjected to axial tension.

To further validate the current model, the case of the single-lap joint under shear loading will be examined. Consider the single-lap joint constructed of a steel upper adherend ($E_1 = 210$ GPa, $v_1 = 0.293$) and an aluminum lower adherend ($E_2 = 70$ GPa,

$v_2 = 0.34$); the adherends have identical width, thicknesses $h_1 = 2$ mm and $h_2 = 4$ mm, and $L = 20$ mm (see Figure 4.17). An average shear traction of $t_0 = 1$ MPa is applied to the right end of the joint. As in the previous sections, the FEM model is constructed in ANSYS™ using four-node *plane-stress* (PLANE182) elements and mapped uniform quadrilateral meshes of four different sizes. The interfacial stresses from the present model and the FEM simulations are plotted in Figure 4.19. The figure shows a close match between the present method and the FEM simulations; also note that the current model accurately predicts the shear stress-free condition at the adherend ends.

One important feature of the stress distributions shown in Figure 4.19 is the concentration of interfacial stresses near the left end of the joint. Due to the non-identical thickness of the adherends, the effective neutral axis of the joint does not lie along the bonding line; this results in a bending moment which is responsible for an increase in shear stress along the interface (which is not located at the neutral axis of joint) as well as the concentration of stresses near the left joint edge. This indicates that debonding failure of this particular joint due to high interfacial stresses would most likely initiate at the left edge of the joint.

One final note should be made concerning the preceding stress analysis of the single-lap joint: due to the assumptions made during formulation of this model (specifically, adherends of homogeneous, isotropic, linearly thermoelastic solids under small deformation), stresses in the joint obey superposition. In other words, the stress solutions for a joint subjected to any combination of tension, shear force, bending moment, or temperature change can be accurately represented as the sum of the interfacial stresses caused by each load separately.

83
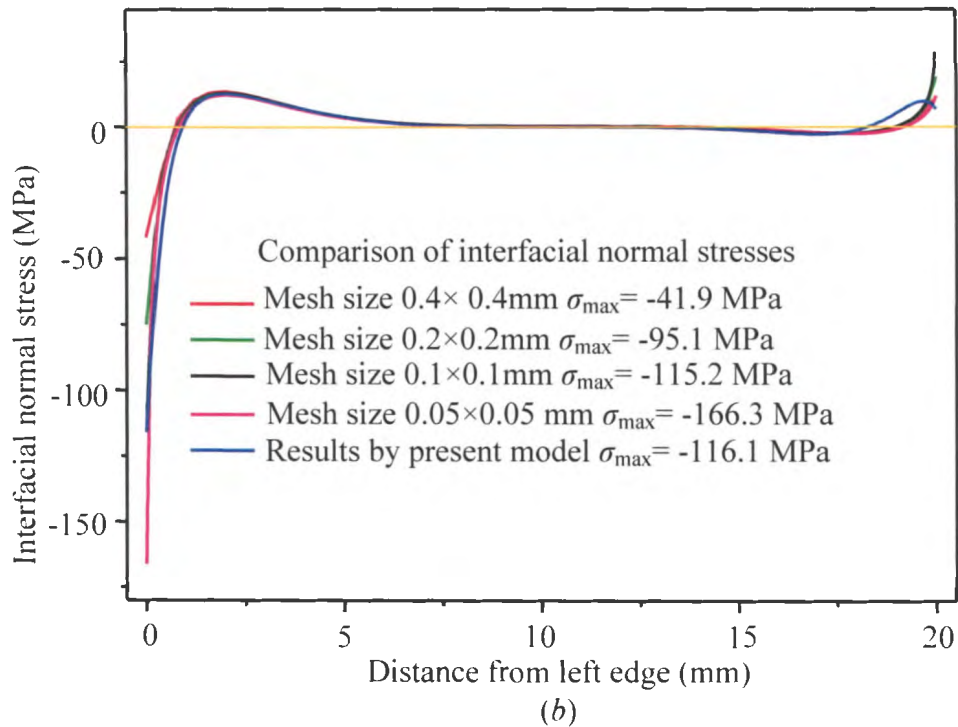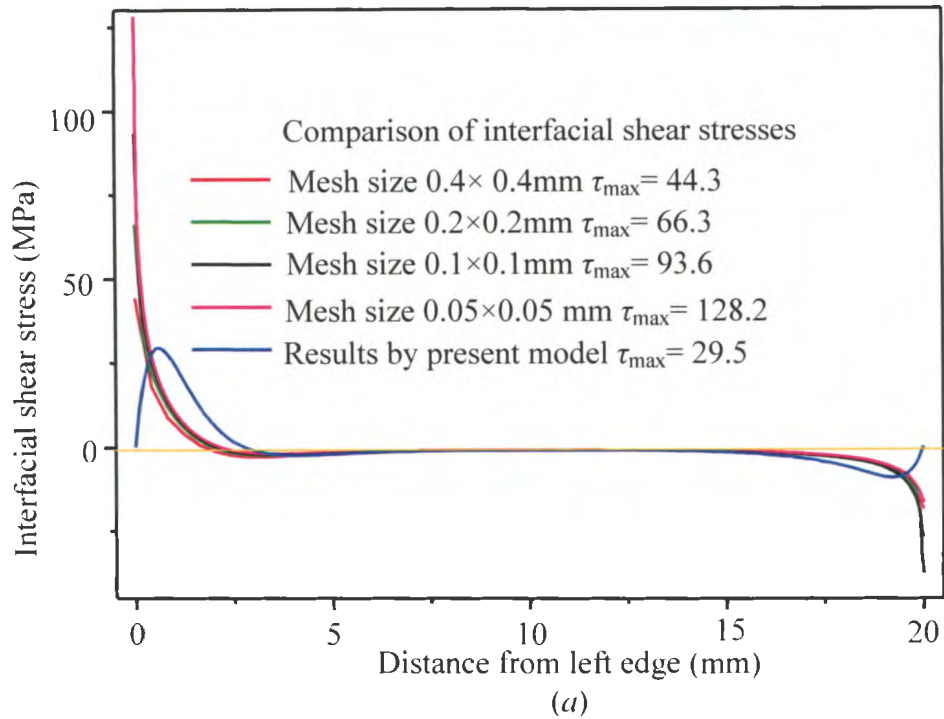
Figure 4.19. Interfacial shear (*a*) and normal (*b*) stresses in a single-lap joint subjected to a transverse shear force: comparison of stresses predicted by the current method with FEM (ANSYS™).

84

4.5 Conclusions

This chapter has developed a generalized stress-function variational method for the interfacial stress analysis of bonded joints, based on a single-sided strap joint model and then generalized to arbitrary joint configurations. Technical deficiencies of the model proposed in Chapter 3 have been remedied successfully; specifically, the approximate deformation compatibility has been removed, leading to a governing system of 4th-order ODEs obtained via the theorem of minimum complementary strain energy. The system of ODEs was explicitly solved with the use of eigenfunctions, resulting in the complete satisfaction of all traction BCs at the joint ends; relevant compact robust computational codes have been developed. Numerical results of the model have been validated through comparison with those obtained by FEM. Scaling analysis has been performed to study the dependencies of interfacial stresses upon the joint parameters and adherend material properties. In the final sections of the chapter, the generality and reliability of the present method has been proven by applying the procedure to the stress analysis of a single-lap joint. Static equivalency of the two joint systems has been shown in a special limiting case; new results for the stress solution of the SLJ under the influence of a shear load have been compared to those based on FEM models. The close agreement between the results based on the current method and those based on FEM simulations indicates the validity of the model, as well as its general applicability for bonded joints of arbitrary configuration.

In the following chapter, this stress-function variational method will be further applied to study the phenomenon of cracking in hard coatings. The coating-substrate system will be modeled as a two-adherend bonded joint, allowing the current methodology to be used for accurate determination of the interfacial stresses and strain energy in the

coating-substrate system under thermal or mechanical loads. By incorporating the strain

energy density and the fracture energy of the joint, the model will be used to determine the

important cracking criterion, i.e. the critical load condition for initial crack in the coating,

critical loads required for progressive cracking, and determination of crack spacing with

respect to given loading conditions. This energy-based approach will lead to some physical

insight into the physical phenomenon of progressive cracking in systems containing hard

coatings.

5. ANALYSIS OF PROGRESSIVE CRACKING IN HARD COATINGS

5.1 Introduction

Surface coatings have found broad applications in industry: from wear resistant coatings, solid lubricants, thermal protection, and many others. These coatings are generally found in the form of a hard thin-film on a compliant substrate; under external loads (e.g. tension, compression, bending, or temperature change) these systems typically experience cracking and debonding of the coating layer. It is therefore desirable to understand the progressive cracking and delamination behavior of these surface coating systems for improved design and health monitoring.

The problem of cracking and buckling delamination has been the focus of much research in recent years (Chakravarthy et al., 2005; Faulhaber et al., 2006); Mishnaevsky and Gross, 2004, 2005; Hutchinson, 2001). A comprehensive review of many previous works on the subject has been made by Hutchinson and Suo (1992). These works considered the propagation of a "blister" along the thin-film/substrate interface, as well as the channeling behavior and mixed-mode nature of the cracks under external loads. In addition to cracking behavior, free-edge stresses of thin-film systems have also been studied: for laminated composites (Pipes and Pagano, 1970; Mittelstedt and Becker, 2004a, b; Wu and Dzenis, 2005) and circular torsion bars (Wu et al., 2007).

The following work will utilize the stress-function variational method developed in the preceding chapter to perform a stress analysis of a thin-film/substrate system under the

influence of externally applied loads (e.g. tension, bending moments, or temperature change). By modeling the film/substrate system as an idealized bonded joint, the previously obtained solutions for the strain energy of the joint will be used to determine the strain energy released by the cracking event in the coating layer. Used in conjunction with a linear-elastic fracture mechanics (LEFM) approach, the progressive cracking behavior of thin-film/substrate systems can be examined.

5.2 Problem Formulation and Solution

5.2.1 Model Formulation

Consider a system consisting of a hard coating deposited on a compliant substrate layer as shown in Figure 5.1. Subjected to any combination of axial tension, transverse bending, or temperature change, periodic cracks may form as the coating layer fails. Stress and failure analysis of this system can be achieved by idealizing the region between surface cracks as a single-sided bonded joint; such a representative section is shown in Figure 5.2. According to the stress-function variational method detailed in Chapters 3 and 4 of this work, the entire interfacial stress field of the joint as well as energy-based failure criteria can be determined.

For the sake of simplifying the following derivation, it is assumed that the periodic cracks form instantaneously through the entire thickness of the coating layer; realistically, the surface crack propagation is not instantaneous and the system may experience a combination of surface cracking, substrate cracking, and interface debonding, but such considerations would make the model prohibitively complicated. Despite these

simplifications, the strengths of the present method lie in the general applicability of the analysis for the interfacial stress prediction and scaling analysis of hard coating systems.

Begin by considering the single-sided bonded joint consisting of a slender substrate layer with a slender cover layer. Consistent with the derivation of previous chapters, the joint is assumed to carry the length L and width b, while the cover and substrate layers have thickness h_1 and h_2, respectively. The axes are defined, as before, with the x-axis directed
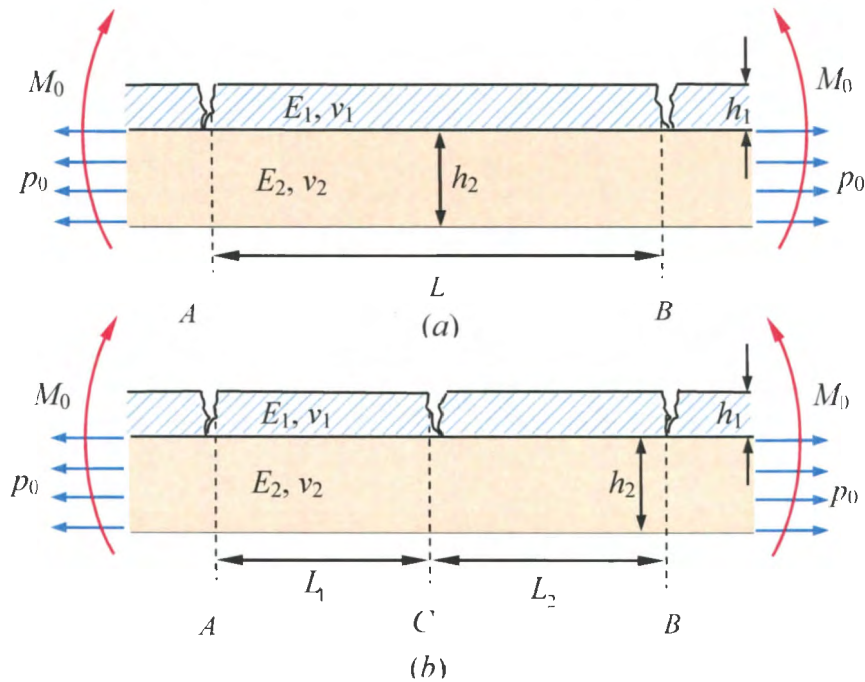
Figure 5.1. (a) Through-thickness cracks in the coating layer of a thin-film/substrate system; (b) formation of secondary crack at arbitrary location C' between adjacent cracks.

from the left edge along the joint axis; y_1 and y_2 are directed vertically from the centroids of cross-sections of the cover layer and substrate, respectively. The joint is assumed to be subjected to uniform tensile stress p_0, bending moment M_0, and uniform temperature change ΔT from a thermal stress-free state. As before, the mismatch of material properties across the interface yields a complicated 3D stress state characterized by high

89

concentrations of interfacial shear and normal stresses near the free edges of the cover layer.

5.2.2 Stress Analysis

The stress analysis of the single-sided bonded joint has been carried out in detail in the preceding two chapters. The same analytic method is applied to the coating/substrate
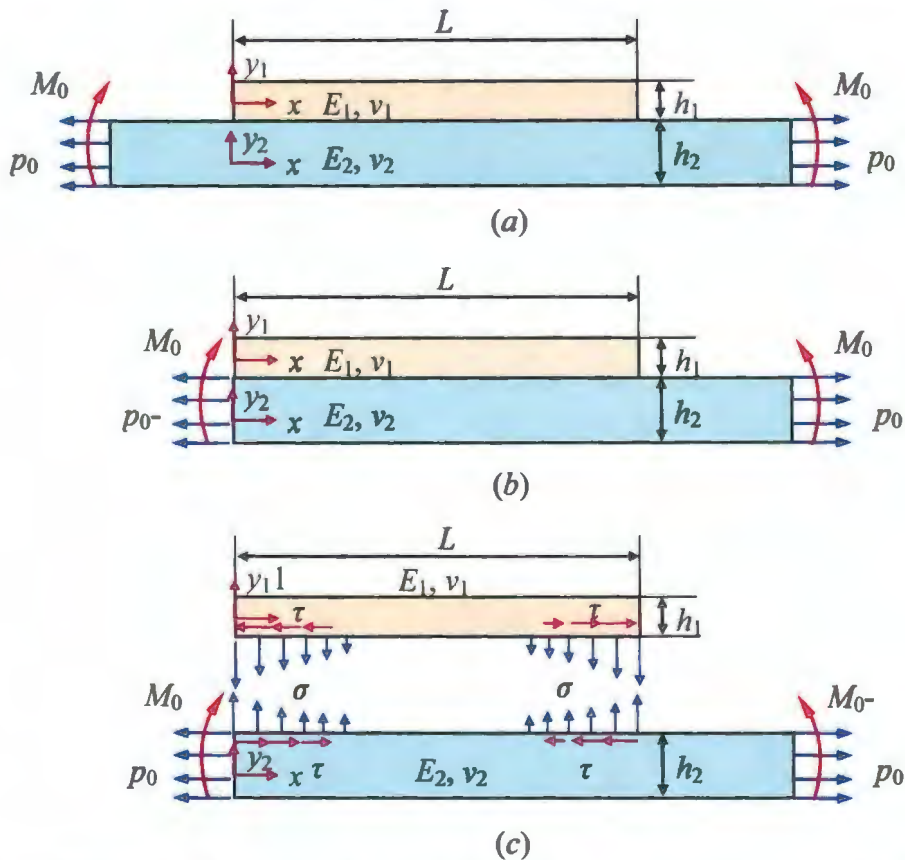
Figure 5.2. Schematic of idealized region between two neighboring surface cracks in a periodically cracked coating layer: (*a*) the single-sided bonded joint model; (*b*) the reduced structure based on symmetry; (*c*) interfacial stresses present in the coating/substrate interface.

model, with a proper modification of traction BCs. Specifically, note that in this case all traction BCs are trivial except for:

$$S_2(0) = p_0 b h_2 \tag{5.1}$$

90

$$S_2(L) = p_0 b h_2 \tag{5.2}$$

$$M_2(0) = M_0 b \tag{5.3}$$

$$M_2(L) = M_0 b \tag{5.4}$$

By following the same procedure outlined in Chapter 4, the planar stress components can be determined explicitly in terms of the interfacial shear and normal stress functions f and g, where the axial normal stresses vary linearly, shear stresses vary parabolically, and transverse normal stresses vary cubically across the substrate and cover layers.

Writing the strain energy of the whole joint as

$$U = b \int_0^L \int_{-h_1/2}^{h_1/2} \left\{ \frac{1}{2} \left[\sigma_{xx}^{(1)} \varepsilon_{xx}^{(1)} + \sigma_{yy}^{(1)} \varepsilon_{yy}^{(1)} \right] + \frac{1+\upsilon_1}{E_1} (\tau_{xy_1}^{(1)})^2 \right\} dy_1 \, dx$$
$$+ b \int_0^L \int_{-h_2/2}^{h_2/2} \left\{ \frac{1}{2} \left[\sigma_{xx}^{(2)} \varepsilon_{xx}^{(2)} + \sigma_{yy}^{(2)} \varepsilon_{yy}^{(2)} \right] + \frac{1+\upsilon_1}{E_1} (\tau_{xy_2}^{(2)})^2 \right\} dy_2 \, dx \tag{5.5}$$

and applying the theorem of minimum complementary strain energy leads to the familiar system of coupled 4$^{\text{th}}$-order ODEs:

$$A_{11} F^{(IV)}(\xi) + A_{12} G^{(IV)}(\xi) + B_{11} F''(\xi) + B_{12} G''(\xi) + C_{11} F(\xi) + C_{12} G(\xi) + D_1 = 0 \tag{5.6}$$

$$A_{12} F^{(IV)}(\xi) + A_{22} G^{(IV)}(\xi) + B_{12} F''(\xi) + B_{22} G''(\xi) + C_{12} F(\xi) + C_{22} G(\xi) + D_2 = 0 \tag{5.7}$$

where all constant coefficients A, B, and C remain as they are given in (4.47) through (4.49); the remaining coefficients are:

$$D_1 = \begin{cases} e_{12} - \dfrac{6M_0}{p_0 h_2^2} - \dfrac{1}{2}(\alpha_1 - \alpha_2)\Delta TE_1 / p_0 \\ \quad \text{(for combined mechanical and thermal loads--\textit{plane} - \textit{stress})} \\[2mm] e_{12} - \dfrac{6M_0}{p_0 h_2^2} - \dfrac{1}{2}[\alpha_1(1+\upsilon_1) - \alpha_2(1+\upsilon_2)]\Delta TE_1 / p_0 \\ \quad \text{(for combined mechanical and thermal loads--\textit{plane} - \textit{strain})} \\[2mm] e_{12} - \dfrac{6M_0}{p_0 h_2^2} \\ \quad \text{(for pure mechanical load--either \textit{plane} - \textit{stress} or \textit{plane} - \textit{strain})} \\[2mm] -\dfrac{1}{2}(\alpha_1 - \alpha_2)\Delta TE_1 / p_0 \\ \quad \text{(for pure thermal load--\textit{plane} - \textit{stress})} \\[2mm] -\dfrac{1}{2}[\alpha_1(1+\upsilon_1) - \alpha_2(1+\upsilon_2)]\Delta TE_1 / p_0 \\ \quad \text{(for pure thermal load--\textit{plane} - \textit{strain})} \end{cases} \tag{5.8}$$

$$D_2 = \begin{cases} e_{12} - \dfrac{12M_0}{p_0 h_2^2} & \text{(pure mechanical or combined mechanical/thermal loads)} \\[2mm] 0 & \text{(pure thermal loads)} \end{cases} \tag{5.9}$$

Note that in the above, for the case of pure temperature change the stress p_0 is considered a reference stress for dimensionless stress analysis.

Following the solution procedure of the previous chapter, the governing ODE is recast as

$$[A]\{\Phi^{(IV)}\} + [B]\{\Phi''\} + [C]\{\Phi\} + \{D\} = \{0\} \tag{5.10}$$

where [A], [B], and [C] are the 2×2 real symmetric matrices of the constant coefficients, and

$$\begin{aligned} \{\Phi\} &= \{F(\xi), G(\xi)\}^T \\ \{D\} &= \{D_1, D_2\}^T \\ \{0\} &= \{0, 0\}^T \end{aligned} \tag{5.11}$$

92

The solution is assumed to be a superposition of the general solution $\{\Psi\}$ and the particular solution $\{\Phi_0\}$:

$$\{\Phi\} = \{\Psi\} + \{\Phi_0\} \tag{5.12}$$

where

$$[A]\{\Psi^{(IV)}\} + [B]\{\Psi''\} + [C]\{\Psi\} = \{0\}$$
$$\{\Phi_0\} = -[C]^{-1}\{D\} \tag{5.13}$$

By converting the expression into a generalized eigenvalue problem, the final expression of the general solution is determined to be

$$\{\Phi\} = \sum_{k=1}^{4} \left[c_k \{\Psi_0^k\} \exp(\lambda_k \xi) + d_k \{\Psi_0^k\} \exp(-\lambda_k \xi) \right] + \{\Phi_0\} \tag{5.14}$$

In this case, the eight linearly independent BCs extracted from the original traction conditions [see Eqs. (5.1)-(5.4)] are all trivial; note the deviation from the conditions of the previous derivation [Eqs. (4.68)-(4.75)]. Given this solution, the interfacial shear and normal stress functions are found to be

$$f(x) / p_0 = \sum_{k=1}^{4} c_k \Psi_0^{k,1} \lambda_k \exp(\lambda_k x / h_2) - \sum_{k=1}^{4} d_k \Psi_0^{k,1} \lambda_k \exp(-\lambda_k x / h_2) \tag{5.15}$$

$$g(x) / p_0 = \sum_{k=1}^{4} c_k \Psi_0^{k,2} \lambda_k^2 \exp(\lambda_k x / h_2) + \sum_{k=1}^{4} d_k \Psi_0^{k,2} \lambda_k^2 \exp(-\lambda_k x / h_2) \tag{5.16}$$

From these stress solutions, all planar stresses in the joint can be fully determined.

5.2.3 Strain Energy and Surface Cracks

By using the strain energy functional given above [Eq. (5.6)], the strain energy density of the coating layer (strain energy per unit length) can be expressed as

$$e = \int_{-h_1/2}^{h_1/2} \left\{ \frac{1}{2} \left[\sigma_{xx}^{(1)} \varepsilon_{xx}^{(1)} + \sigma_{yy}^{(1)} \varepsilon_{yy}^{(1)} \right] + \frac{1+\upsilon_1}{E_1} (\tau_{xy_1}^{(1)})^2 \right\} dy_1$$
$$+ \int_{-h_2/2}^{h_2/2} \left\{ \frac{1}{2} \left[\sigma_{xx}^{(2)} \varepsilon_{xx}^{(2)} + \sigma_{yy}^{(2)} \varepsilon_{yy}^{(2)} \right] + \frac{1+\upsilon_1}{E_1} (\tau_{xy_2}^{(2)})^2 \right\} dy_2$$

(5.17)

Utilizing the same variation process as before and the solution already attained (5.14), the strain energy density per unit length is determined to be

$$e = \frac{1}{2} \{\Phi\}^T \{D\} \frac{p_0^2 h_2}{E_1} + \frac{6}{E_2 h_2^3} M_0^2 + \frac{h_2}{2E_2} p_0^2 + \frac{\alpha_2 h_2}{2} \Delta T p_0$$

(5.18)

Alternatively, the full expression can be recast as

$$e(\xi) = \frac{1}{2} \sum_{k=1}^{4} \left[c_k \{\Psi_0^k\}^T \{D\} \exp(\lambda_k \xi) + d_k \{\Psi_0^k\}^T \{D\} \exp(-\lambda_k \xi) \right] \frac{p_0^2 h_2}{E_1}$$
$$- \frac{1}{2} \{D\}^T [C]^{-1} \{D\} \frac{p_0^2 h_2}{E_1} + \frac{6}{E_2 h_2^3} M_0^2 + \frac{h_2}{2E_2} p_0^2 + \frac{\alpha_2 h_2}{2} \Delta T p_0$$

(5.19)

Note that in (5.19), the first term results from the stress concentrations near the free edges of the joint (coating layer cracks); the remaining terms indicate the strain energy density of an un-cracked coating/substrate system. This energy density is denoted e_0:

$$e_0(\xi) = -\frac{1}{2} \{D\}^T [C]^{-1} \{D\} \frac{p_0^2 h_2}{E_1} + \frac{6}{E_2 h_2^3} M_0^2 + \frac{h_2}{2E_2} p_0^2 + \frac{\alpha_2 h_2}{2} \Delta T p_0$$

(5.20)

Furthermore, consider the case of a single crack in the coating layer; setting the system origin at the location of the crack, the energy density in the right-half of the system is given by:

$$e_\infty(\xi) = \frac{1}{2} \sum_{k=1}^{4} d_k \{\Psi_0^k\}^T \{D\} \exp(-\lambda_k \xi) \frac{p_0^2 h_2}{E_1}$$
$$- \frac{1}{2} \{D\}^T [C]^{-1} \{D\} \frac{p_0^2 h_2}{E_1} + \frac{6}{E_2 h_2^3} M_0^2 + \frac{h_2}{2E_2} p_0^2 + \frac{\alpha_2 h_2}{2} \Delta T p_0$$

(5.21)

Here, λ_k ($k = 1, 2, 3, 4$) are four eigenvalues with positive real parts, and d_k are the constants determined by solving the reduced system of traction BCs; for the case of the single crack, terms with non-decaying exponentials (corresponding to the stresses induced by the right free edge of the joint, non-existent in this case) are discarded. These reduced traction BCs are given by

$$\sum_{k=1}^{4} d_k \Psi_0^{k,1} = -\Phi_0^{(1)} \tag{5.22}$$

$$\sum_{k=1}^{4} d_k \lambda_k \Psi_0^{k,1} = 0 \tag{5.23}$$

$$\sum_{k=1}^{4} d_k \Psi_0^{k,2} = -\Phi_0^{(2)} \tag{5.24}$$

$$\sum_{k=1}^{4} d_k \lambda_k \Psi_0^{k,2} = 0 \tag{5.25}$$

5.2.4 Critical Loading and Temperature Change for Initial Cracking

The cracking criterion is established within the framework of LEFM such that: given certain loading conditions, i.e., external loads M_0 or p_0 or temperature change ΔT, the increase in strain energy (ΔU) due to cracking must equal the strain energy release $\Delta \Gamma$:

$$\Delta U = \Delta \Gamma = G_C b h_1 \tag{5.26}$$

where G_C is the critical strain energy release rate for the crack in the coating layer; it is assumed that mode-I cracking occurs. The criterion for the initial cracking in the coating layer is

$$G_{IC} h_1 = 2 \int_0^{+\infty} (e_\infty(\xi) - e_0) \, d\xi \tag{5.27}$$

Substitution of expressions (5.20) and (5.21) into (5.27) yields

95

$$G_{IC} h_1 = \sum_{k=1}^{4} d_k \lambda_k^{-1} \{\Psi_0^k\}^T \{D\} \frac{p_0^2 h_2}{E_1} \tag{5.28}$$

It can be shown that the right side of (5.28) has a quadratic dependence on the loading variables such that

$$\sum_{k=1}^{4} d_k \lambda_k^{-1} \{\Psi_0^k\}^T \{D\} \frac{p_0^2 h_2}{E_1} = A_{pp} p_0^2 + A_{MM} M^2 + A_{TT} (\Delta T)^2 + A_{pM} p_0 M + A_{pT} p_0 \Delta T + A_{MT} M \Delta T$$

$$\tag{5.29}$$

where A_{pp}, A_{MM}, A_{TT}, A_{pM}, and A_{MT} are coefficients which can be determined by the relevant material properties and geometric parameters of the coating/substrate system.

5.2.5 Progressive Cracking and Crack Density in the Coating Layer

To study the phenomenon of progressive cracking in the coating layer, first consider a coating/substrate system in which periodic cracks already exist with spacing L (Figure 5.1a). As the external load (e.g. tensile stress, bending moment, or temperature change) increases in magnitude, a critical load is reached at which a new through-thickness surface crack appears at a location C somewhere between A and B. Given (5.26), the cracking criterion is

$$G_c h_1 = \int_0^{s_1} e(\xi) \, d\xi + \int_0^{s_2} e(\xi) \, d\xi - \int_0^{s} e(\xi) \, d\xi \tag{5.30}$$

where $s_1 = L_1/h_2$, $s_2 = L_2/h_2$, $s = L/h_2$, and $e(\xi)$ is given by (5.19). The integrals in (5.30) can be evaluated and expressed explicitly, leading to the cracking criterion

$$G_c h_1 = \Pi_1 + \Pi_2 - \Pi_3 \tag{5.31}$$

where

96

$$\Pi_1 = \left\{ \sum_{k=1}^{4} \sinh \frac{\lambda_k s_1}{2} \left[c_k \lambda_k^{-1} \exp\left(\frac{\lambda_k s_1}{2} \right) \{\Psi_0^k\}^T + d_k \lambda_k^{-1} \exp\left(\frac{-\lambda_k s_1}{2} \right) \{\Psi_0^k\}^T \right] \right\} \{D\} \frac{p_0^2 h_2^2}{E_1} \quad (5.32)$$

$$\Pi_2 = \left\{ \sum_{k=1}^{4} \sinh \frac{\lambda_k s_2}{2} \left[c_k \lambda_k^{-1} \exp\left(\frac{\lambda_k s_2}{2} \right) \{\Psi_0^k\}^T + d_k \lambda_k^{-1} \exp\left(\frac{-\lambda_k s_2}{2} \right) \{\Psi_0^k\}^T \right] \right\} \{D\} \frac{p_0^2 h_2^2}{E_1} \quad (5.33)$$

$$\Pi_3 = \left\{ \sum_{k=1}^{4} \sinh \frac{\lambda_k s}{2} \left[c_k \lambda_k^{-1} \exp\left(\frac{\lambda_k s}{2} \right) \{\Psi_0^k\}^T + d_k \lambda_k^{-1} \exp\left(\frac{-\lambda_k s}{2} \right) \{\Psi_0^k\}^T \right] \right\} \{D\} \frac{p_0^2 h_2^2}{E_1} \quad (5.34)$$

where the coefficients c_k and d_k are determined according to the eight linearly independent traction BCs from Section 5.2.2 with $L/h_2 = s_1$, s_2, and s. Now Eq. (5.31) [with (5.32)—(5.34)] determines the critical load for progressive cracking of a system with specific single load or combination of loads with constant ratio.

Generally speaking, the location C of the subsequent coating layer crack can be assumed to be a random variable (see Figure 5.1). Therefore, a probability density function p is required to describe the location of the next cracking. Letting T_c denote the critical external load (e.g. tensile stress, bending moment, or uniform temperature change) required to cause the next cracking in a coating/substrate system of pre-existing crack density $d = 1/L$, the expected value of T_c is

$$E[T_c(s)] = h_2 \int_0^s p(\xi) T_c(\xi) \, d\xi \quad (5.35)$$

where T_c is given by (5.31). While the choice of probability density function will affect the results of the progressive cracking analysis, for the simplicity of the following analysis it is assumed that the next cracking will occur equidistant from the adjacent pre-existing cracks. This case can be represented by defining the probability density function with the Dirac delta function:

$$p(\xi) = \delta(\xi - s/2) \quad (5.36)$$

5.3 Numerical Examples

5.3.1 Interfacial Stresses in Cracked Surface Coatings

Closed form solutions for the interfacial shear and normal stresses in a coating/substrate system are given by (5.15) and (5.16) with the application of appropriate boundary conditions. First consider the case of the interfacial stresses in a compliant substrate and hard coating layer with a single through-thickness crack in the coating. As mentioned in Section 5.2.3, the interfacial stresses are high near the free edges of the crack, and decay abruptly with increasing distance from the crack ends. Therefore, it is assumed that $c_k = 0$ for ($k = 1, 2, 3, 4$), and d_k is found by solving the set of linear algebraic equations in (5.22)—(5.25).

It is useful to examine the effects of material properties and geometric parameters on the stress distributions in these systems; to illustrate these effects, Figures 5.3 and 5.4 show plots of the dimensionless interfacial shear and normal stresses with varying thickness ratio at two different modulus ratios. There are several features to note from this comparison. Firstly, increasing the Young's modulus of the coating layer relative to the substrate increases the magnitude of both the peak values of interfacial shear and normal stresses; the increase in modulus ratio also appreciably affects the distribution of these stresses: when $E_1/E_2 = 1$, the stresses are localized around a distance of approximately $1.5h_2$, but when the ratio is increased to 5 the stress field spreads to a distance of roughly $2.5h_2$.

Next consider the coating/substrate system in which periodic cracks exist in the coating layer. The interfacial shear and normal stresses between two adjacent cracks with spacing L are plotted in Figures 5.5 and 5.6 with various thickness and modulus ratios.
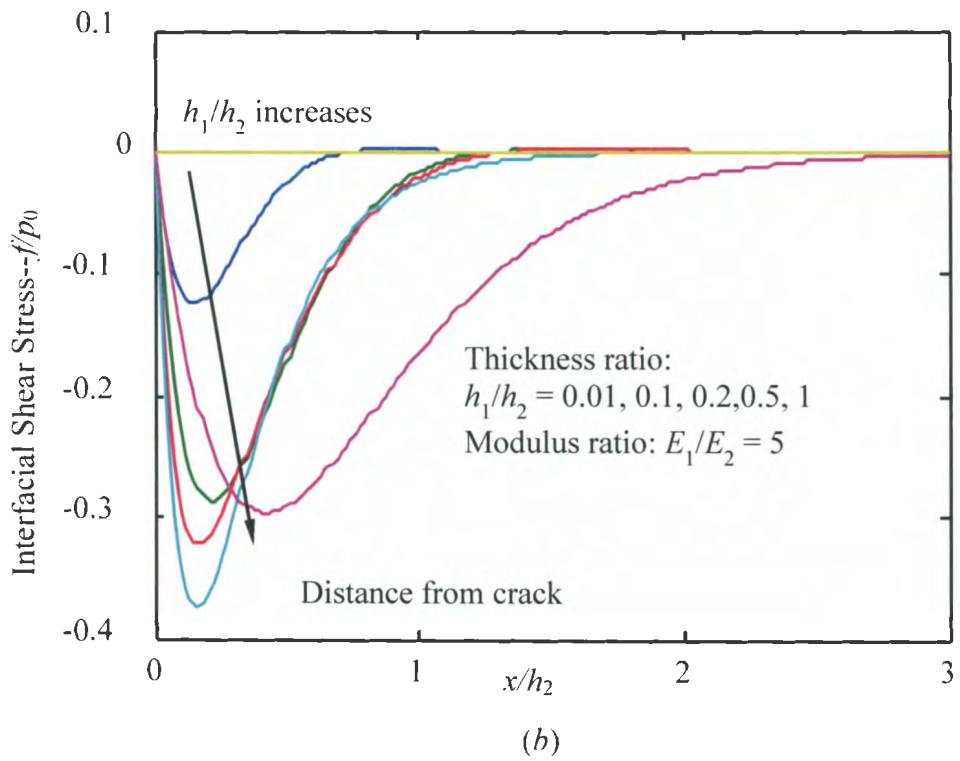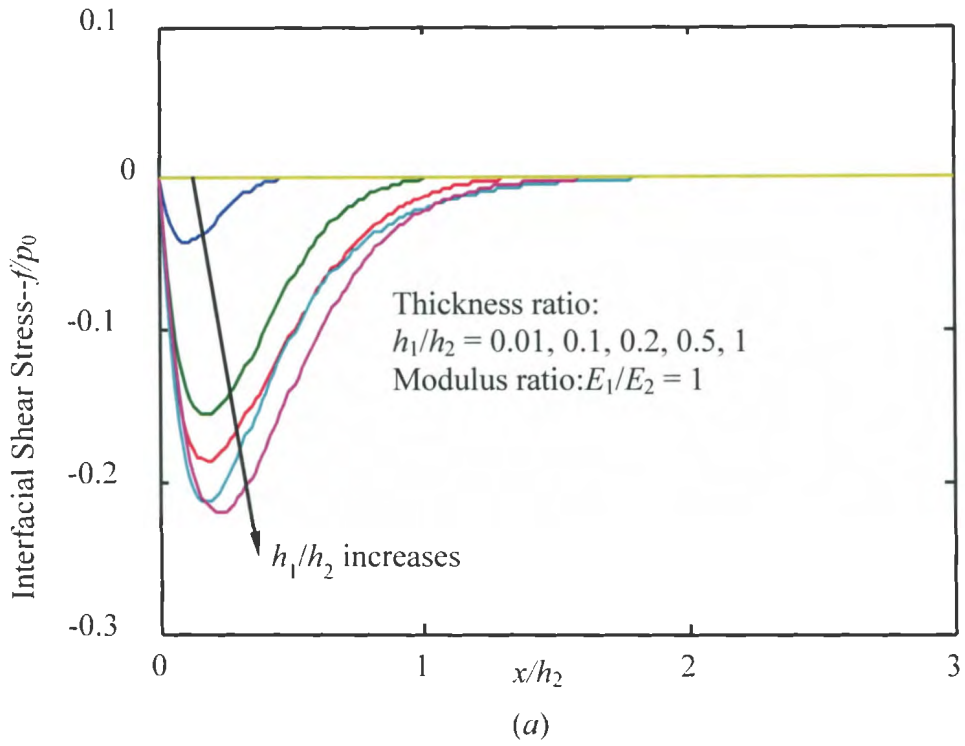
Figure 5.3. Variations of the dimensionless interfacial shear stresses over distance from the crack in a single-cracked hard coating/substrate system, including varying thickness and modulus ratios.
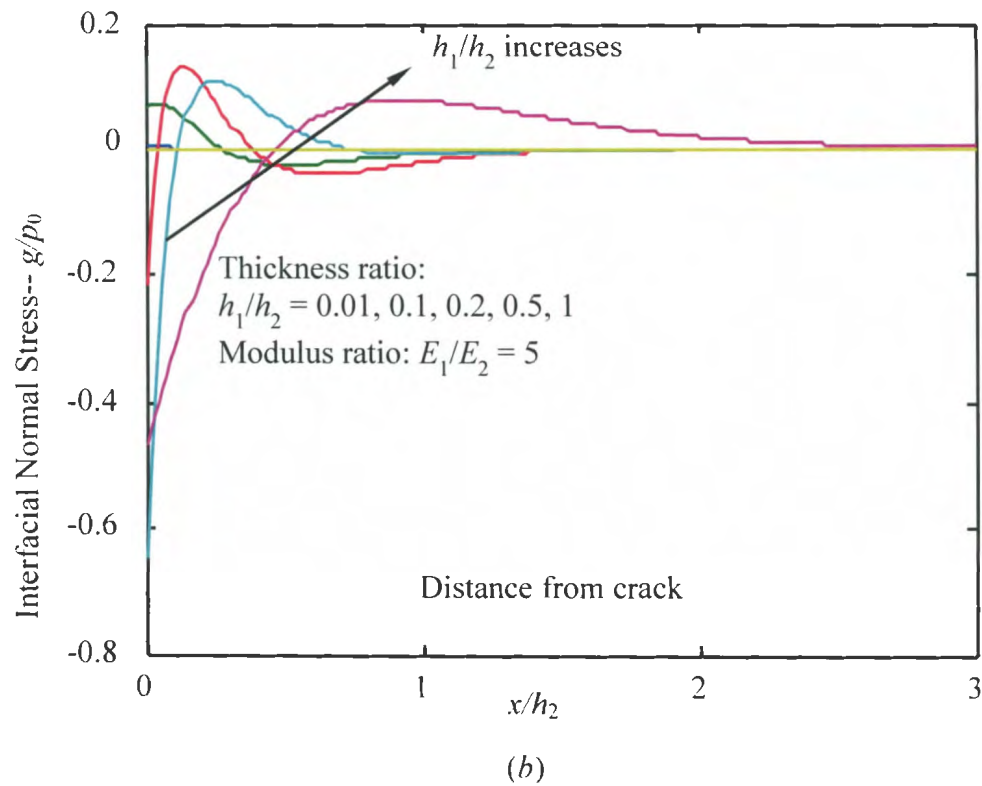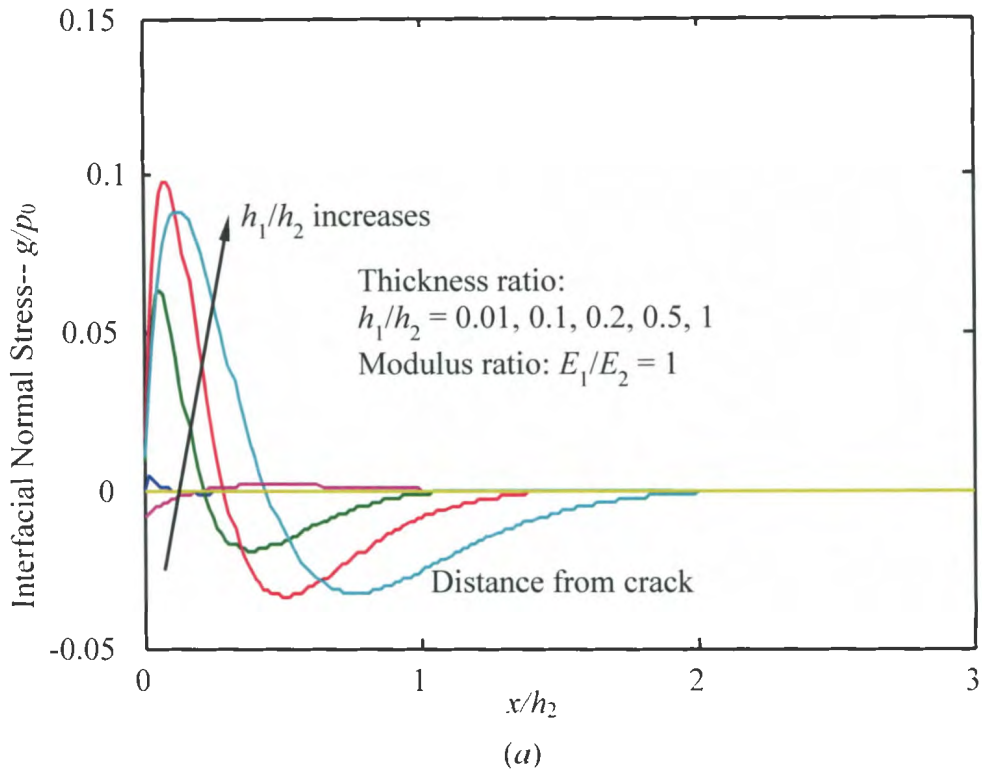
Figure 5.4. Variations of the dimensionless interfacial normal stresses with varying thickness and modulus ratios in a single-cracked hard coating/substrate system.

Figure 5.5. Variations of the dimensionless interfacial shear stresses with respect to dimensionless distance from the left crack in the coating/substrate system with periodic surface cracks.
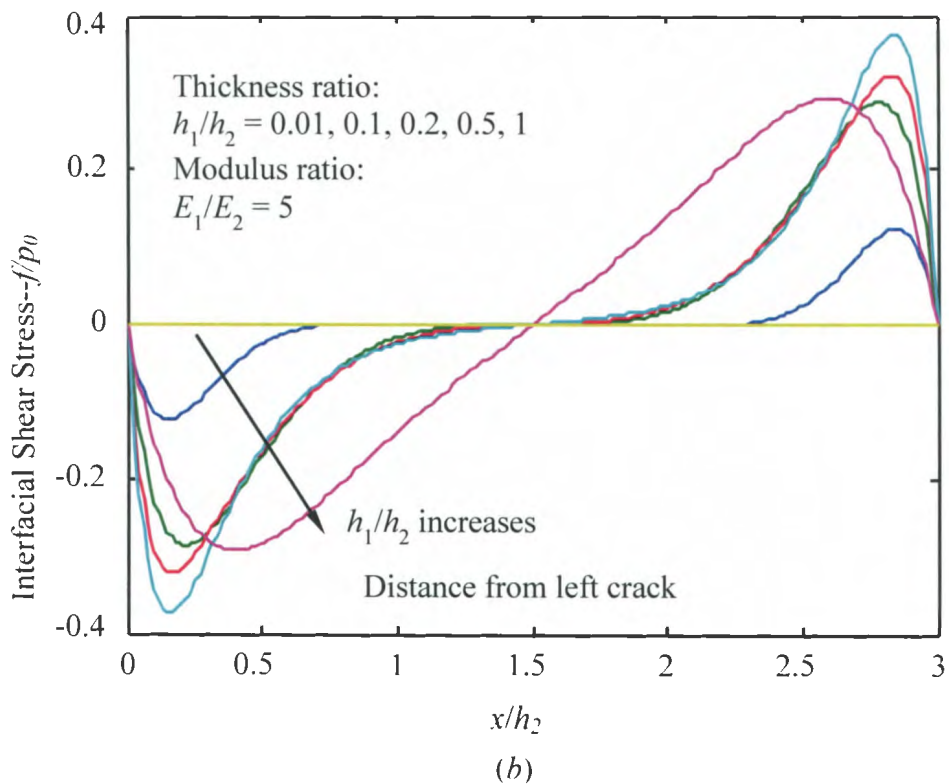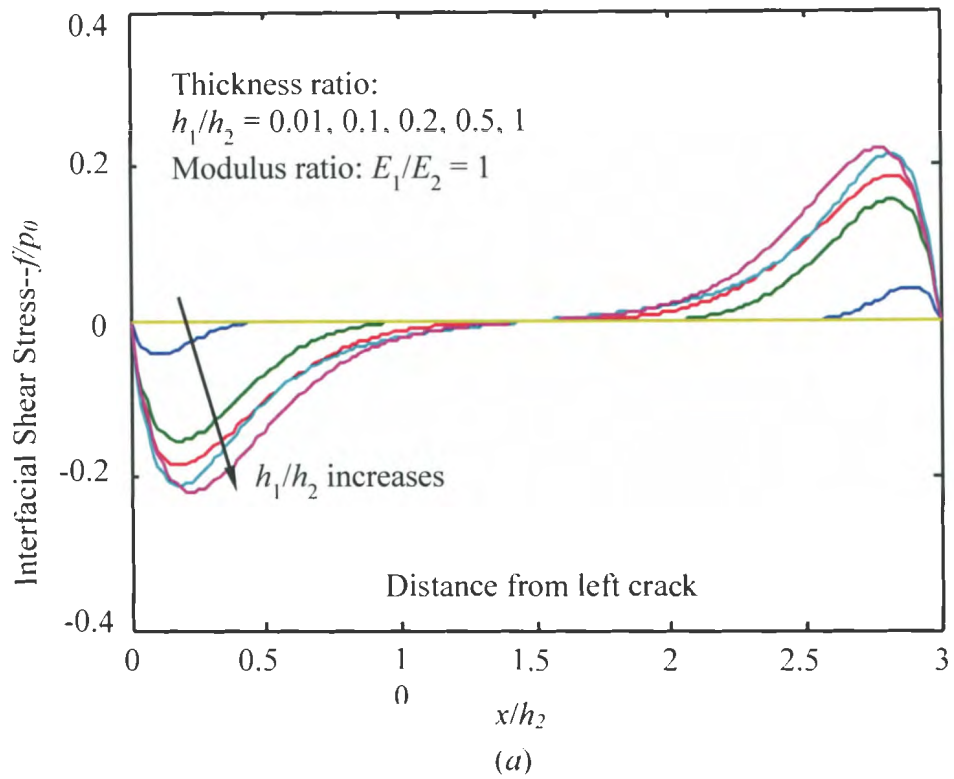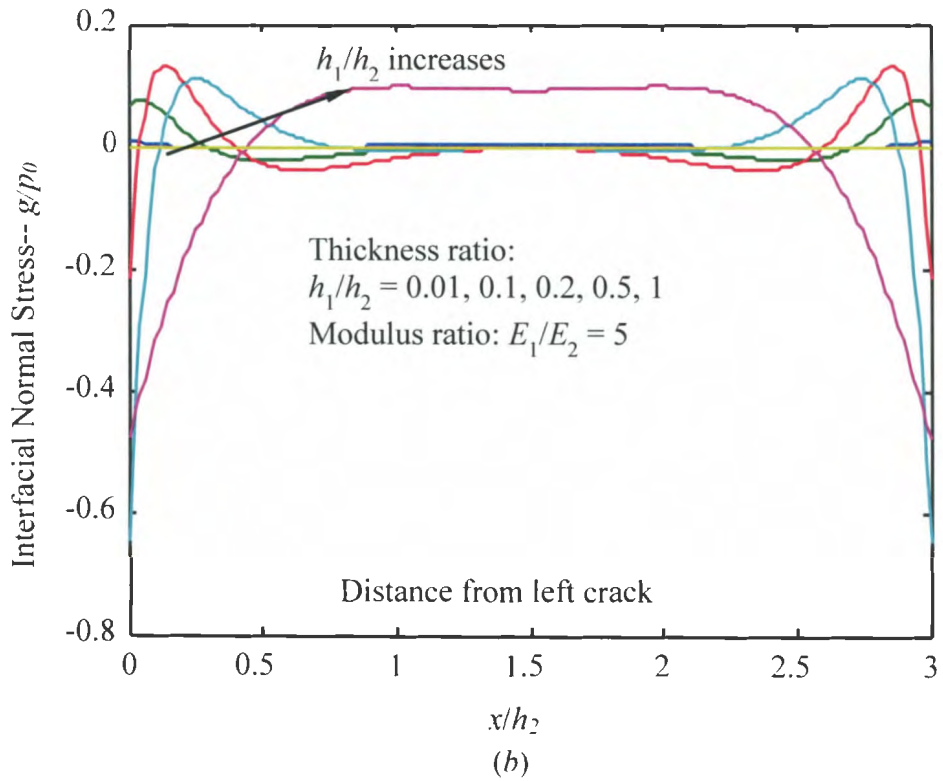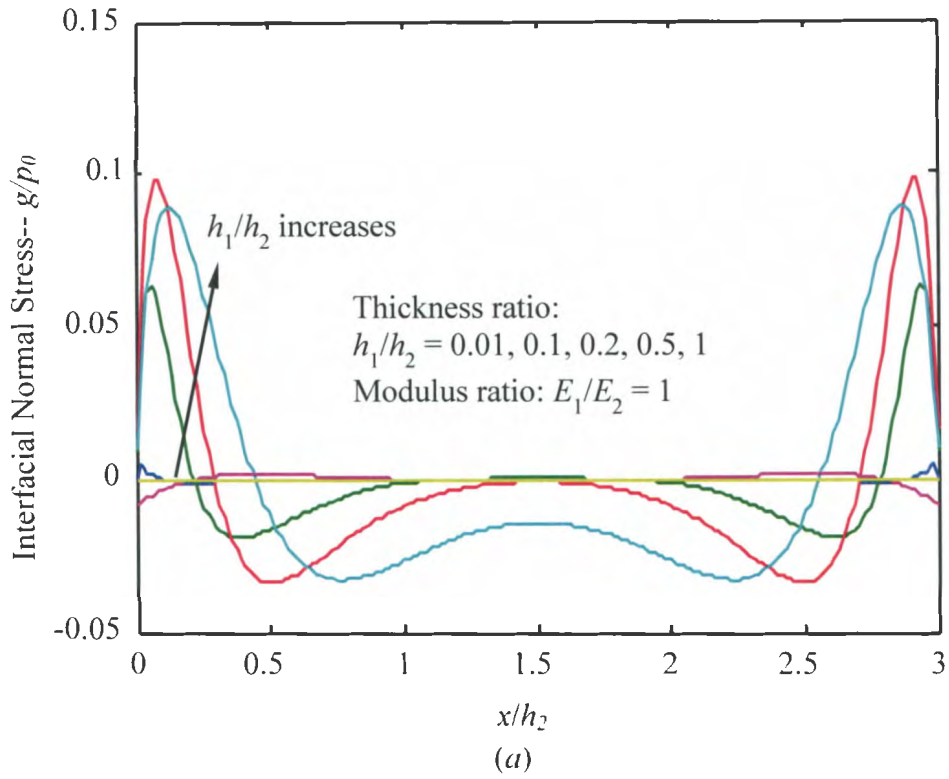
101

Figure 5.6. Variations of the dimensionless interfacial normal stresses in a hard coating system with periodic coating-layer cracks.

These plots indicate that, as with the single crack model shown in the previous figure, thicker coating layers lead to higher values of interfacial shear and normal stress. What these figures show is that increasing the effective stiffness of the coating (i.e., Young's modulus or the layer thickness) with respect to the substrate has the effect of increasing the magnitude of the interfacial shear and normal stresses.

5.3.2 Crack Density in Hard Coating Layers

Finally, consider the progressive cracking phenomenon in hard coatings. The initial through-thickness surface crack will appear in the hard coating on a compliant substrate once the condition of Eq. 5.31 is met. Following the initial crack, progressive surface cracking commences with increasing load; consider the dimensionless crack spacing as it varies with dimensionless critical load $p_0 h_2^2 / G_C h_1$ (for the case of uniform axial tension). This represents the dimensionless applied tension with respect to the cracking energy $G_C h_1$. As mentioned at the end of Section 5.2.5, the critical load is taken to be the expected value corresponding to the assumption that the progressive crack will occur equidistant from the existing cracks at spacing L/h_2 [Eq. (5.36)]. Figure 5.7 depicts the crack spacing over the dimensionless critical load for varying thickness and modulus ratios. Again, the data indicate that for a given crack spacing, the thicker coating layers lead to lower critical load. Furthermore, stiffer coating layers (those with higher Young's modulus) show lower critical loads by comparison with those with a lower stiffness. These results are similar to those of the previous section: thicker, stiffer coating layers not only lead to higher values of interfacial shear and normal stresses (typically responsible for debonding failure of bonded joints) but also lower the resistance to mode-I cracking.

103

Predicted Crack-Spacing vs. Load Diagram

Thickness ratio: h_1/h_2 = 0.01, 0.02, 0.05, 0.1, 0.2
Modulus ratio E_1/E_2 = 2

h_1/h_2 increases

Crack spacing--H/h_2

Dimensionless Load $p_0 h_2^2/(G_C h_1)$

Predicted Crack-Spacing vs. Load Diagram

Thickness ratio: h_1/h_2 = 0.01, 0.02, 0.05, 0.1, 0.2
Modulus ratio E_1/E_2 = 7

h_1/h_2 increases

Crack spacing--H/h_2
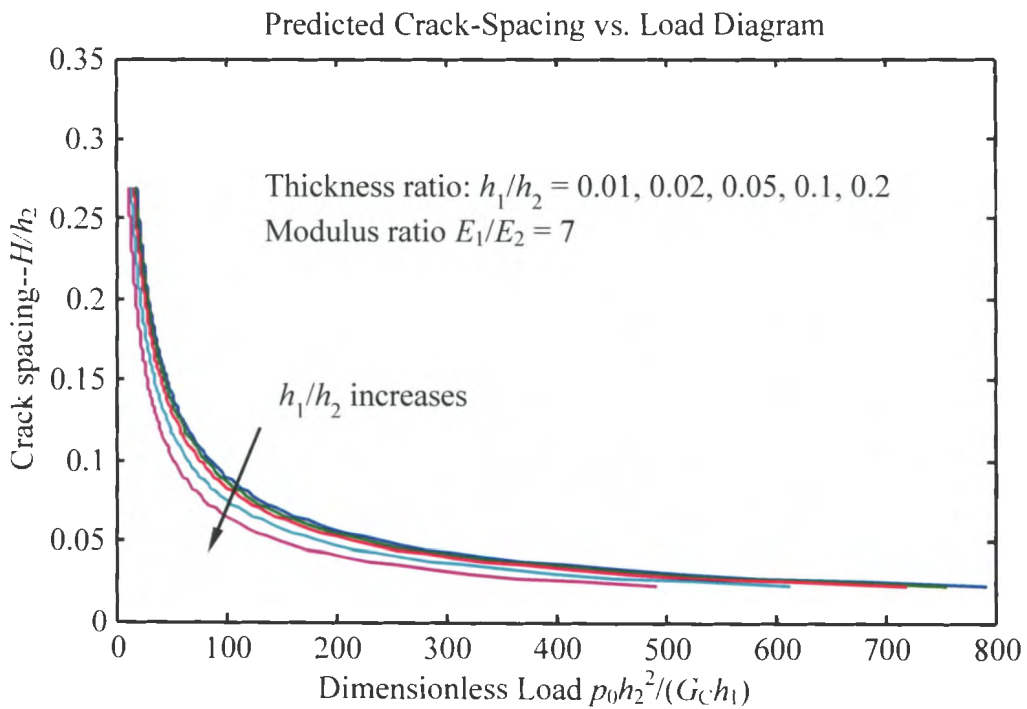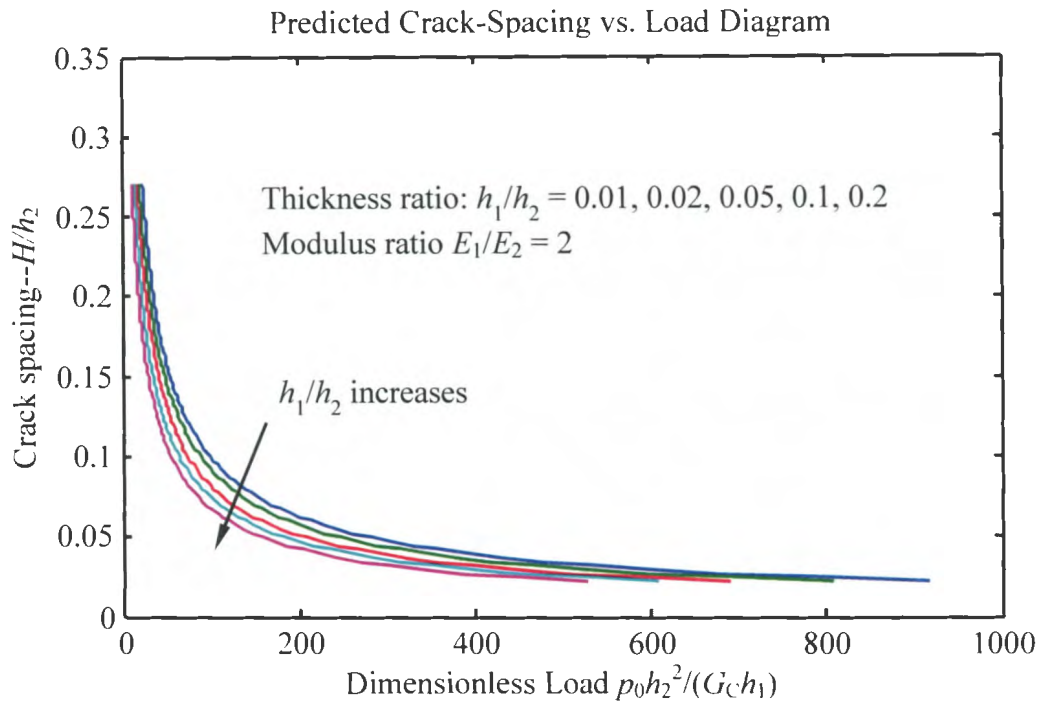
Dimensionless Load $p_0 h_2^2/(G_C h_1)$

Figure 5.7. Variations of the dimensionless surface crack spacing vs. the dimensionless critical load at varying layer thickness ratios at two different modulus ratios.

104

5.4 Conclusions

In this chapter, the stress-function variational method for determination of interfacial stresses in bonded joints has been extended for surface cracking analysis of hard coatings. The strain energy expressions determined by the interfacial stress solutions have been used in conjunction with LEFM to construct energy-based criteria for initial and progressive cracking in the hard coating layers. Explicit criteria have been formulated and demonstrated for the determination of the critical load (e.g. the tensile stress, bending moment, or temperature change) required for initial cracking in the hard coating layer, as well as progressive cracking. Effects on the critical load and crack spacing by thickness and modulus ratio have been examined. It has been indicated by the results of the dimensionless scaling analysis that thicker coating layers resulted in both higher interfacial stresses and lower critical load for given crack spacing. Furthermore, stiffer coating layers (higher Young's modulus) exhibit a similar trend. This analysis can be efficiently used in design and optimization of hard coating/compliant substrate systems and cracking prediction.

6. CONCLUSIONS

In summary, bonded joints are commonly used structural components that have been extensively integrated into various engineering applications as load transfer elements, separated part connections, vehicular components, and microelectronics packaging. Besides, thin films of hard coatings on compliant substrates, such as those used for solid lubricants, thermal shielding, and wear and corrosion resistance, can also be analyzed using an idealized bonded joint model.

In this study, we have successfully formulated a theoretical methodology for the stress analysis of bonded joints consisting of two arbitrary adherends. The main theoretical accomplishments achieved by the present thesis include:

1. Formulation of a novel stress-function variational method for the stress analysis of bonded joints made of two arbitrary adherends, in which two interfacial stress functions are directly introduced. These stress functions can completely satisfy all relevant stress equilibrium equations for representative segmental elements of joint adherends.

2. Satisfaction of all physical boundary conditions at the ends of the adherends. Deformation compatibility is enforced through minimization of the complementary strain energy of the joint. The resulting governing 4th-order ODEs are solved efficiently with eigenfunctions.

The results of this analysis have been validated successfully through several means. In Chapter 3, a single-sided bonded joint has been analyzed, and the results of the present method have been compared with those obtained by elementary mechanics of materials.

106

The predicted stresses have been found to be in a close agreement for the case of long slender adherends, with larger deviation for shorter cover layers; this is likely due to the breakdown of classic beam theory for shorter and thicker beams. Comparisons with results of a detailed FEA of the joint have also supported the accuracy of the present model.

Chapter 4 has examined two different joint configurations: the single-sided strap joint and the single-lap joint. These models have also been compared against FEA data; the models accurately predict the high interfacial stress concentrations near the free edges of the adherends with values close to those given by the FEA. Furthermore, analysis of the joints subjected purely to temperature change has yielded results in a close agreement with those found in the literature for bi-metal thermostats.

Scaling analyses have also been performed on the bonded joint models to investigate the dependence of interfacial stress distribution on material properties and geometric parameters. Interfacial stress distributions have been modeled for varying thickness ratios, length ratios, and modulus ratios. It has been found that increasing the effective stiffness of the cover layer (or reinforcing patch) relative to the substrate (via increased thickness or increased Young's modulus) had the effect of lowering the values of interfacial stress in typical bonded joints. The ability of the current model to easily perform such detailed scaling analyses makes it well-suited for joint design and optimization.

Chapter 5 studied the cracking behavior of hard coatings on compliant substrates. Cracking criteria have been developed using linear-elastic fracture mechanics (LEFM) considerations in conjunction with the stress analysis of the previous chapters. By idealizing the coating/substrate system as a two-adherend bonded joint model, criteria have

been developed to determine the critical load (e.g. uniform axial tension, bending moments, or uniform temperature change) to cause the initial crack and progressive cracking in the coating layer; this has allowed for an analysis of the behavior of the dimensionless crack spacing and its dependence on applied loads.

The analysis developed in this work has the potential for broad application in engineering practices for efficient, robust scaling analysis and design optimization for bonded joint systems. For example, the analysis could be used to predict how variations in the thickness or rigidity of polymeric substrates affect the critical stresses present in flexible electronics applications. In the field of civil engineering, structures are often strengthened via the application of surface reinforcing patches on support components; the methods presented in this thesis could be utilized in the design of these reinforcing patches to optimize their strengthening characteristics while minimizing the addition of building material. Furthermore, the cracking analysis developed in Chapter 5 provides a basis for understanding how the health of hard, thin coatings depends on relative material/geometric properties between the coating and substrate (particularly in the specific failure scenario of through-thickness surface cracks).

Despite the advances of the work presented in this thesis, further refinements to the process may be made:

1. Generalizing the model for the analysis of bonded joints of arbitrary numbers of layers. The current method is only applicable to two-layer joint models; more complicated joint geometries, and joints in which the adhesive layer properties and influence need to be considered are outside the scope of the present formulation.

2. Adapting the model for anisotropic composite adherends. The present model assumes isotropic adherends, which limits the applicability of the analysis to other types of component materials. Adapting the formulation to anisotropic adherends would allow for the stress analysis of fiber-reinforced polymers and layered composites.

Making the recommended modifications to the stress-function variational method would greatly enhance the strength of the formulation and create a robust model capable of handling a wide variety of physically meaningful bonded joint applications.

REFERENCES CITED

Beer, F., Johnston, E.R., Dewolf, J.T., Mazurek D.F., 2009. Mechanics of Materials (5th Edition). McGraw Hill, New York, USA.

Brockmann, W., Geiss, P.L., Klingen, J., Schroder, K.B., 2009. Adhesive Bonding: Materials, Applications and Technology. Wiley-VCH, Weinheim.

Carpinteri, A., Cornetti, P., Pugno, N., 2009. Edge debonding in FRP strengthened beams: stress versus energy failure criteria. Eng. Struct. 31, 2436-2447.

Chakravarthy, S.S., Jordan, E.H., Chiu, W.K.S., 2005. Thin film and substrate cracking under the influence of externally applied loads. Eng. Fract. Mech. 72, 1286-1298.

Chang, F.V., 1990. Interlaminar stresses of laminated composite joints with double cover plates. Int. J. Solid Struct. 26, 165-174.

Chang, F.V., 1993. Interlaminar Stresses on Composite Materials (in Chinese). High Education Press. Beijing, China.

Chen, D., Cheng, S., 1983. An analysis of adhesive-bonded single-lap joints. J. Appl. Mech. Trans. ASME 50, 109-115.

Chen, W.T., Nelson, C.W., 1979. Thermal stress in bonded joints. IBM J. Res. Develop. 23, 179-188.

da Silva, L.F.M., das Neves, P.J.C., Adams, R.D., Spelt, J.K., 2009. Analytic models of adhesively bonded joints-part I: literature survey. Int. J. Adhesion Adhesives 29, 319-330.

Delale, F., Erdogan, F., Aydinoglu, M.N., 1981. Stress in adhesively bonded joints: A closed-form solution. J. Compos. Mater. 15, 249-271.

Diaz, A.D., Hadj-Ahmed, R., Foret, G., Ehrlacher, A., 2009. Stress analysis in a classical double lap, adhesively bonded joint with a layerwise model. Int. J. Adhesion Adhesives 29, 67-76.

Eischen, J.W., Chung, C. Kim, J. H., 1990. Realistic modeling of edge effect stresses in bimaterial elements. ASME Electro. Packag. 112, 16-23.

Erdogan, F., Ratwani, M., 1971. Stress distribution in bonded joints. J. Compos. Mater. 5, 378-393.

Faulhaber, S., Mercer, C., Moon, M.W., Hutchinson, J.W., Evans, A.G., 2006. Buckling delamination in compressed multilayers on curved substrates with accompanying ridge cracks. J. Mech. Phys. Solids 54, 1004-1028.

Goland, M., Reissner, E., 1944. The stresses in cemented joints. J. Appl. Mech. Trans. ASME 11, 17-24.

Goncalves, J.P.M., de Moura, M.F.S.F., de Castro, P.M.S.T., 2002. A three-dimensional finite element model for stress analysis of adhesive joints. Int. J. Adhesion Adhesives 22, 357-65.

Hart-Smith, L.J., 1973. Adhesive-bonded single-lap joints. NAS CR-112236.

Her, S.C., 1999. Stress analysis of adhesively-bonded lap joints. Compos. Struct. 47, 673-678.

Higgins, A., 2000. Adhesive bonding of aircraft structures. Int. J. Adhesion Adhesives 20, 367-76.

Hutchinson, J.W., 2001. Delamination of compressed films on curved substrates. J. Mech. Phys. Solids 49, 1847-1864.

Hutchinson, J.W., Suo, Z., 1992. Mixed mode cracking in layered materials. Adv. App. Mech. 29, 63-194.

Jiang, H.Q., Khang, D.Y., Fei, H.Y., Kim, H., Huang, Y.G., Xiao, J.L., Rogers, J.A. 2008. Finite width effect of thin-films buckling on compliant substrate: experimental and theoretical studies. J. Mech. Phys. Solids. 56, 2585-2598.

Jiang, H.Q., Khang, D.Y., Song, J.Z., Sun, Y.G., Huang, Y.G., Rogers, J.A., 2007. Finite deformation mechanics in buckled thin films on compliant supports. Proc. Natl. Acad. Sci. 104, 15607-15612.

Khang, D.Y., Jiang, H.Q., Huang,Y., Rogers, J.A., 2006. A stretchable form of single-crystal silicon for high-performance electronics on rubber substrates. Science 311, 208-212.

Khang, D.Y., Rogers, J.A., Lee, H.H., 2009. Mechanical buckling: mechanics, metrology, and stretchable electronics. Adv. Funct. Mater. 18, 1-11.

Kim, D.H., Rogers,J.A. 2008. Stretchable electronics: materials strategies and devices. Adv. Mater. 20, 1-6.

Lee, J., Kim, H., 2005. Stress analysis of generally asymmetric single lap adhesively bonded joints. J. Adhesion 81, 443-472.

Tsai, M.Y., Hsu, C.H., Han, C.N., 2004. A note on Suhir's solution of thermal stresses for a die-substrate assembly, J. Electron. Packag. 126, 115-119.

Tsai, M.Y., Oplinger, D.W., Morton, J., 1998. Improved Theoretical Solutions for Adhesive Lap Joints. Int. J. Solids Structures 35, 1163-85.

Volkersen, O., 1938. Die Nietkraftverleitung in zugbeanspruchten Nietverbindungenmitkonstanten Laschenquerschnitten. Luftfahrtforschung 15, 41-7.

Wu, X.F., Dzenis, Y.A., 2002a. Closed-form solution for the size of plastic zone in an edge-cracked strip. Int. J. Eng. Sci. 40, 1751-1759.

Wu, X.F., Dzenis, Y.A., 2002b. Closed-form solution for a mode-III interfacial edge crack between two bonded dissimilar elastic strips. Mech. Res. Commun. 29, 407-412.

Wu, X.F., Dzenis, Y.A., 2005. Experimental determination of probabilistic edge-delamination strength of a graphite-fiber/epoxy composite. Composite Struct. 70, 100-108.

Wu, X.F., Dzenis, Y.A., Fan, T.Y., 2003a. Two semi-infinite interfacial cracks between two bonded dissimilar elastic strips. Int. J. Eng. Sci. 41, 1699-710.

Wu, X.F., Dzenis, Y.A., Gokdag, E., 2004. Edge-cracked orthotropic bimaterial butt joint under anti-plane singularity. Int. J. Nonlinear Sci. Numer. Simulation 5, 347-354.

Wu, X.F., Dzenis, Y.A., Strabala, K.W., 2007. Free-edge stresses and progressive cracking in surface coatings of circular torsion bars. Int. J. Solids Structures 45, 2251-2264.

Wu, X.F., Dzenis, Y.A., Zou, W.S., 2003b. Interfacial edge crack between two bonded dissimilar orthotropic strips under antiplane point loading. Z. Angew. Math. Mech. (ZAMM) 83, 419-22.

Yin, W. L., 1994a. Free edge effects in anisotropic laminates under extension, bending and twisting. Part I: A stress-function-based variational approach. ASME J. Appl. Mech.; 61: 410-415.

Yin, W. L., 1994b. Free edge effects in anisotropic laminates under extension, bending and twisting. Part II: Eigenfunction analysis and the results for symmetric laminates. ASME J. Appl. Mech. 61, 416-421.

Yu, H.H., Hutchinson, J.W., 2001. Edge effects in thin film delamination. Acta Mater. 49, 93-107.

Yu, H.H., Hutchinson, J.W., 2003. Delamination of thin film strips. Thin Solid Films 423, 54-63.

114

Yuan, H., Teng, J.G., Seracino, R., Wu, Z.S., Yao, J., 2004. Full-range behavior of FRP-to-concrete bonded joints. Eng. Struct. 26, 553-565.